R-04-63

Preliminary site description: Groundwater flow simulations

Simpevarp area (version 1.1) modelled with CONNECTFLOW

Lee Hartley, David Worth, Serco Assurance
Björn Gylling, Niko Marsic, Kemakta Konsult AB
Johan Holmén, Golder Associates

August 2004

Svensk Kärnbränslehantering AB
Swedish Nuclear Fuel
and Waste Management Co
Box 5864
SE-102 40 Stockholm Sweden
Tel 08-459 84 00
+46 8 459 84 00
Fax 08-661 57 19
+46 8 661 57 19

ISSN 1402-3091
SKB Rapport R-04-63

Preliminary site description: Groundwater flow simulations

Simpevarp area (version 1.1) modelled with CONNECTFLOW

Lee Hartley, David Worth, Serco Assurance
Björn Gylling, Niko Marsic, Kemakta Konsult AB
Johan Holmén, Golder Associates

August 2004

Contents

1 Introduction

The main objective of this study is to assess the role of known and unknown hydrogeological conditions for the present-day distribution of saline groundwater at the Simpevarp and Laxemar sites. An improved understanding of the paleo-hydrogeology is necessary in order to gain credibility for the Site Descriptive Model in general and the Site Hydrogeological Description in particular. This is to serve as a basis for describing the present hydrogeological conditions as well as predictions of future hydrogeological conditions.

This objective implies a testing of:

- geometrical alternatives in the structural geology and bedrock fracturing,
- variants in the initial and boundary conditions, and
- parameter uncertainties (i.e. uncertainties in the hydraulic property assignment).

This testing is necessary in order to evaluate the impact on the groundwater flow field of the specified components and to promote proposals of further investigations of the hydrogeological conditions at the site.

1.1 Background

This study is being performed by two separate modelling teams, one of which is The CONNECTFLOW Team involving consultants from Serco Assurance, Kemakta Konsult and Golder Associates using the CONNECTFLOW groundwater flow and transport software. This software contains several modules including the NAMMU continuum porous medium (CPM) code, the NAPSAC discrete fracture network (DFN) code, and the GeoVisage 3D visualisation code.

The current modelling studies of the Simpevarp area have utilized data described in the 1.1 Data freeze (from 1 July 2003) for the modelling performed in January–February 2004. The structural model however, is the same as that used for Oskarshamn Version 0.

1.2 Expected paleo-hydrogeological results

A number of deliverables are specified in the Task Description 1.5, February 25, 2004. In terms of developing the understanding of the paleo-hydrogeological situation at the site, the following results were requested:

- Video showing the transient salinity evolution (driven by advection) in 3 E-W profiles (parallel to the regional model boundaries) and one N-S profile through KLX01visualised in Tecplot and figures showing the salinity for the same section at 5000 BC, 0 BC, 2000 AD (times may be adjusted).

- Video showing the present-day distribution of the salinity distribution between z=–2100 and ground surface visualised in Tecplot with a vertical E-W -plane sweeping from North to South. Figures showing the present day salinity at –10, –100, –500 and –1000 masl.
- Figures showing the present day q(Darcy) in the z-direction at –10, –100, –500 and –1000 masl and average downwards vertical component of q(Darcy) within the local model as function of depth.

In addition, profiles of salinity as a function of depth within KLX01 and KLX02 at various times are used to compare variants.

1.3 Transport performance measures

Additional results were required to assess the implications for performance measures relating to safety assessment:

- Using the velocity field at 2000 AD particles are released at –500 m distributed over two defined parts of the local model domain.
  - Simpevarp peninsula: (X,Y) (1550500, 6365200) (1552500, 6365200) (1552500, 6366200) (1550500, 6366200).
  - Laxemar area: (X,Y) (1548700, 6366500) (1550300, 6366500) (1550300, 6367800) (1548700, 6367800).
- Statistics, graphs or pictures for all cases with regards to
  - t(adv.) of all flowpaths.
  - q(Darcy)- length of the flow vector, at depth at the starting positions.
  - Discharge positions of particles.
  - Salinity profiles along the trend and plunge of KLX01 and KLX02.
  - F-factor for all pathways.
  - K-distribution (histogram, logN-probability plot) for the local domain.

1.4 Sensitivity analysis

A number of simulations were performed to investigate the influence the conceptual and parameter uncertainties including those relating to initial conditions, DFN data interpretation, and transport porosity values.

Invariants for the models considered in Version 1.1 are:

- Flow boundary condition on the top surface: Dirichlet topographic pressure.
- No-flow on vertical boundaries located at regional flow divides.
- Salinity boundary condition on top: Dirichlet value for salinity (as a function of time and shoreline) at inflows, outflow condition on outflow.
- No flow boundary condition at base.
- Specified salinity on base at –2300 masl 10%.
- Structural model and hydraulic conductivities of fracture zones.

Variations performed:

- Initial salinity condition 1 (used for most cases): Zero salinity to –500 masl, linearly increasing to 10% at –2100 masl.
- Initial salinity condition 2 (used in one variant): Zero salinity to –1000 masl, linearly increasing to 10% at –2100 masl.
- Sensitivity study of the kinematic porosity accessible to salinity in fracture zones and rock mass.
- Include smaller scale fractures.
- Higher fracture density (P32) by a factor of 5.
- Convergence check on temporal discretisation.

It should be noted that some of the input data was updated since calculations were begun. These changes included:

- New RVS structural model in the latest RVS version format.
- Corrections to the topographic data to fix some anomaly offshore and the position of the current shoreline.
- Change minimum background rock hydraulic conductivity from 10^{-11} to 10^{-9} m/s.
- New facility in CONNECTFLOW for combining fracture and rock mass properties according to a weighting by relative transmissibility rather than volume.

Due to time constraints it was not possible to re-run and post-process these calculations with the new data. However, it was thought that the impact of these changes would not be significant to the results and conclusions presented here.

2 Methodology and features used in CONNECTFLOW

The Oskarshamn 1.1 study made use of both the DFN and CPM capabilities within CONNECTFLOW. Detailed descriptions of the functionality of CONNECTFLOW are available elsewhere /1, 2, 3, 4, 5/. However, it useful to summarise how CONNECTFLOW was used within this project and detail a few specifics of how certain functionality is implemented in the software.

2.1 Workflow

Figure 2-1 shows a schematic overview of the modelling workflow used in the project. The starting to point is the DFN conceptual model and the associated fracture properties such as fracture density (P32), fracture length distributions, transmissivity distributions etc. DFN models can be constructed in simple block domains initially to analyse the implications of the fracture conceptual model to calculate quantities such as equivalent CPM hydraulic conductivity as a function of block size, and to assess sensitivities to modelling parameters such as truncation of parameter distributions such fracture length or transmissivity. Once, the DFN model is understood, a regional-scale DFN can be constructed within the regional mesh and then "upscaled" to produce an equivalent CPM model that has hydraulic properties consistent with a realisation of the underlying DFN data. This CPM regional-model is then used to simulate transient groundwater flow and salt transport and to provide the required performance measures.

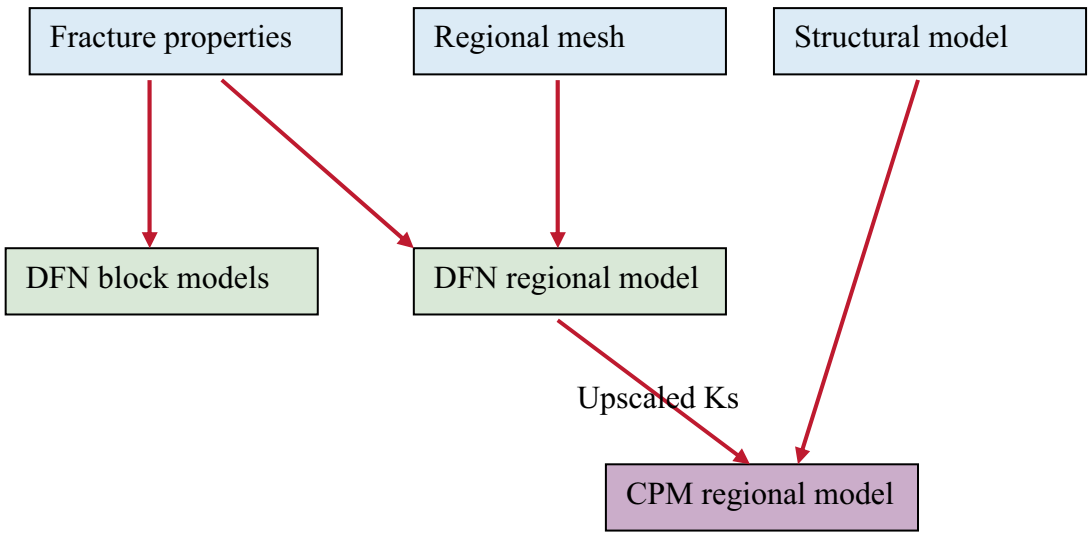

Figure 2-1. *A schematic workflow for the CONNECTFLOW modeling.*

2.2 DFN models

DFN models in CONNECTFLOW are created using the NAPSAC module /3/. To generate a DFN model in NAPSAC the following data is required:

- Fracture length distribution (e.g. Power-law).
- Fracture intensity model (e.g. Poisson point process).
- Fracture orientation distribution (e.g. Univariate Fisher).
- Division of fractures into sets.
- Fracture transmissivity or hydraulic aperture (used to parameterise flow).
- Fracture transport aperture (used to parameterise transport).

These basic parameters are used to define stochastic fractures. Additional deterministic fractures can be added as planes or triangulated surfaces. Extra complexity can be introduced into models such as:

- Direct or partial correlations between fracture length and transmissivity.
- Variable aperture on fractures.
- Different P32 within different regions or rock types.
- Fracture damage zones around structures (e.g. swarms of fractures associated with a lineament).
- Fracture truncation against rock/lithology boundaries.
- Hydromechanical coupling. That is, relationships between transmissivity and the directional stress tensors (e.g. an increase in fracture transmissivity for fractures parallel to the maximum horizontal stress, or a decrease in transmissivity with increased overburden at depth).

2.3 Fracture upscaling to equivalent CPM properties

DFN models can be constructed within simple block domains or complex site meshes (either structured or unstructured) containing many elements. In order to assess the implications of the DFN model on flow and transport, one approach is to convert the DFN model to an equivalent CPM model. The result is a directional permeability tensor, fracture porosity (and other properties such as the matrix block sizes and shapes between the inter-connected fracture network). For a simple block model these equivalent CPM parameters can be calculated for an array of sub-blocks of arbitrary size, whereas for a site mesh the DFN can be converted to an equivalent CPM element-by element. The upscaling method use to calculate the equivalent CPM permeability tensor is described in detail in /6/. Briefly, the method can be summarised by the following steps:

- Define a sub-block or element within DFN model.
- Identify the fractures that cut the element.
- Calculate the connections between these fractures and their connection to the faces of the element.

- Specify a linear pressure gradient parallel to each coordinate axis on all the faces of the element.
- Calculate the flow through the network and the flux through each face of the element and for each axial pressure gradient.
- Fit a symmetric anisotropic tensor that best fits (least-squares) the flow response of the network.
- Fracture porosity is calculated as the sum of fracture area within the element multiplied by the transport aperture of the fracture.

Hence, to calculate the equivalent CPM properties for a mesh with 1 million elements, say, involves 3 times 1 million DFN flow calculations. One important aspect of this approach is the properties are calculated on a particular scale, that of the element-size, and that a connectivity analysis of the network is performed only on the scale of the element. Bulk flows across many elements will depend on the correlation and variability of properties between elements. Inherent within the DFN approach is the assumption that there is no flow in the matrix between the fractures, i.e. flow takes place only in the fracture planes and flow passes from one fracture to the next at their intersections.

2.4 Treatment of fracture zones

For Simpevarp 1.1, the DFN model was constructed using the large stochastic fractures from scales between 100–1000 m. Using the upscaling methods described above, an equivalent CPM model of these fractures was created. At that point the structural model in terms of the geometry and properties of a set of large-scale fracture zones was combined with the equivalent CPM model using the Implicit Fracture Zone (IFZ) method in CONNECTFLOW as described in /7/. This method identifies which elements are crossed by a fracture zone and combines a permeability tensor associated with the fracture zone with a permeability tensor for the background fractured rock. For each element crossed by the fracture zone the following steps are performed:

1. The volume of intersection between the fracture zone and the element is determined.
2. The effective permeability tensor that represents the combined effect of the background rock and fracture zone is determined in the coordinate system aligned with the feature.
3. The effective permeability tensor that includes the effect of the fracture zone is determined in the coordinate system aligned with the fracture zone.
4. The effective permeability tensor that includes the effect of the fracture zone is determined in the original coordinate system.

Similarly, a combined scalar porosity is calculated for the element based on combining the fracture zone porosity and the background fracture rock porosity using a weighting either based simply on either the relative volume or on relative transmissibility (transmissivity times thickness (m^3/s)). The latter weighting can be suitable for transport since it weights the combined porosity toward the fracture zone porosity if this is of a relatively high permeability. The result of this step is to produce a spatial distribution of CPM element properties (permeability tensor and porosity) that represent the combined influence of both the deterministic fractures zones and background stochastic fractures.

2.5 Transient groundwater flow and salt transport

The simulations of how flow and salinity have evolved in the post-glacial period up to the present day is modelled in CONNECTFLOW using a CPM model with fixed hydraulic properties, but with boundary conditions that change with time. In this study, the head on the top surface was set to the topographic height that evolves in time due to post-glacial rebound. Offshore, the head was equal to the depth of the sea multiplied by the relative salinity of the Baltic Sea, and here both the salinity of the Baltic and sea depth altered in time. Simulations were started at 10,000 BC with a hypothetical initial salinity distribution and run until the present day. CONNECTFLOW uses a fully-implicit time-stepping method for stability with a piecewise constant time-step size.

Typical time-step sizes were 10 to 20 years with smaller time-steps used at earlier times to minimise oscillations than can arise from a simplified and potentially unphysical initial condition. To avoid non-linear oscillations the groundwater flow calculations at each time-step are solved in two-steps: solve for flow (pressure) for a variable groundwater density, and then solve an advection dispersion equation for salinity in the new flow field, and so update the spatial distribution of groundwater density distribution. In this way, the flow and transport equations are decoupled within a time-step. This is a valid simplification and gives a stable scheme providing the time-step is chosen to be suitably small. Some examination of convergence with respect to the temporal discretisation was made in this study.

Currently, CONNECTFLOW uses a single porosity model for modelling salt transport. From a numerical standpoint, this porosity is a kinematic porosity for the rate of movement of salinity and is given as the Darcy velocity divide by the kinematic porosity. In terms how to define a physical concept and model for this parameter it depends on the speed of the transient process and how much of the fracture and accessible pore space salinity is able to enter as a saline front moves through a model. In the context of this study, the natural transients considered evolve slowly over thousands of years, so there is likely be time for salinity to access a significant portion of the available pore space by a combination of advection through the small scale fractures and diffusion into the rock mass. Hence, it will be assumed that salinity accesses the matrix and so the value of kinematic porosity used here will be chosen to be of a magnitude close to the total porosity of fractures and rock mass. This is a much larger value, maybe a factor 100, than the porosity associated with advection in the fracture system alone. However, when calculating advective particle tracks for safety assessment it is usual to make conservative assumptions about the kinematic porosity and use a value that is chosen based only on the porosity of the major conductive features. Hence, in CONNECTFLOW we use two different values for the kinematic porosity: one for the transient salt transport calculation (based physically on a total porosity), and one for the particle tracking (based physically on the conductive fracture porosity).

A new formulation of the salt transport equations to include rock matrix diffusion will be available in CONNECTFLOW April 2004.

3 Groundwater flow model construction

3.1 Properties

The properties for fracture zones, rock mass and overburden are given accordingly to the Paleo-hydrogeology Task Description (TD).

As of January 2004, the only structural model available for Simpevarp was the Version 0.2 XML file which defines the Version 0 structural model on a regional-scale. Hence, the fracture zone geometries were created from this file using RVSInfo, but the fracture zone properties were taken from the Version Simpevarp 1.1 TD. Most zones are 20 m thick according to the Simpevarp Version 0.2 XML file. The properties used in the model are listed in Table 3-1.

Table 3-1. Summary of the properties of the Simpevarp 1.1 model based on TD Paleo-hydrogeology.

Property	Overburden	Rock Mass	Zones
Transmissivity, T (m^2/s)	–	DFN model: aL^b	$1.3 \cdot 10^{-5}$
Thickness, b (m)	3	–	From RVS (~20 m)
Conductivity, K (m/s)	$1.5 \cdot 10^{-5}$	From DFN, Min=$1.0 \cdot 10^{-9}$	–
Kinematic porosity (–)	0.05	$1 \cdot 10^{-5}$	–
Storativity (–)		function of L ($1 \cdot 10^{-6}$ to $2 \cdot 10^{-5}$)	$2.0 \cdot 10^{-5}$
Transport aperture (m)	–	function of L ($1 \cdot 10^{-6}$ to $2 \cdot 10^{-5}$)	$1.0 \cdot 10^{-3}$

The hydraulic conductivity of the rock mass is calculated based on the DFN which defined in terms of fracture properties as described in Section 3.4.

3.2 Topographic data

Topographic data was supplied on two scales, 50 m and 10 m. Since the refined 10 m data covered the entire regional-scale model area defined in the TD, this fine-scale data was used both to define the model area and to set boundary conditions on the top surface. In addition, a number of regional and local water divides had been identified. In CONNECTFLOW it is possible to construct unstructured meshes with irregular boundaries, and hence it is possible to choose boundaries that follow water divides. Figure 3-1 shows the extent of the topographic data and water divides along with the regional model domain as proposed in the TD. Boundaries were chosen as close as possible to the proposed domain, but following water-divide wherever possible. The motivation for using water-divides was that these have some physical basis for use as no-flow boundaries, and hence form a more natural choice than an arbitrary box. Further, in choosing such boundaries problems are avoided in having no-flow boundaries in places where flow would naturally cross the boundary under realistic conditions. The most sensible way to address uncertainties associated with the choice of lateral boundaries would be to keep the boundaries in a natural position, but vary the type of boundary condition e.g. a hydrostatic (no vertical flow) condition.

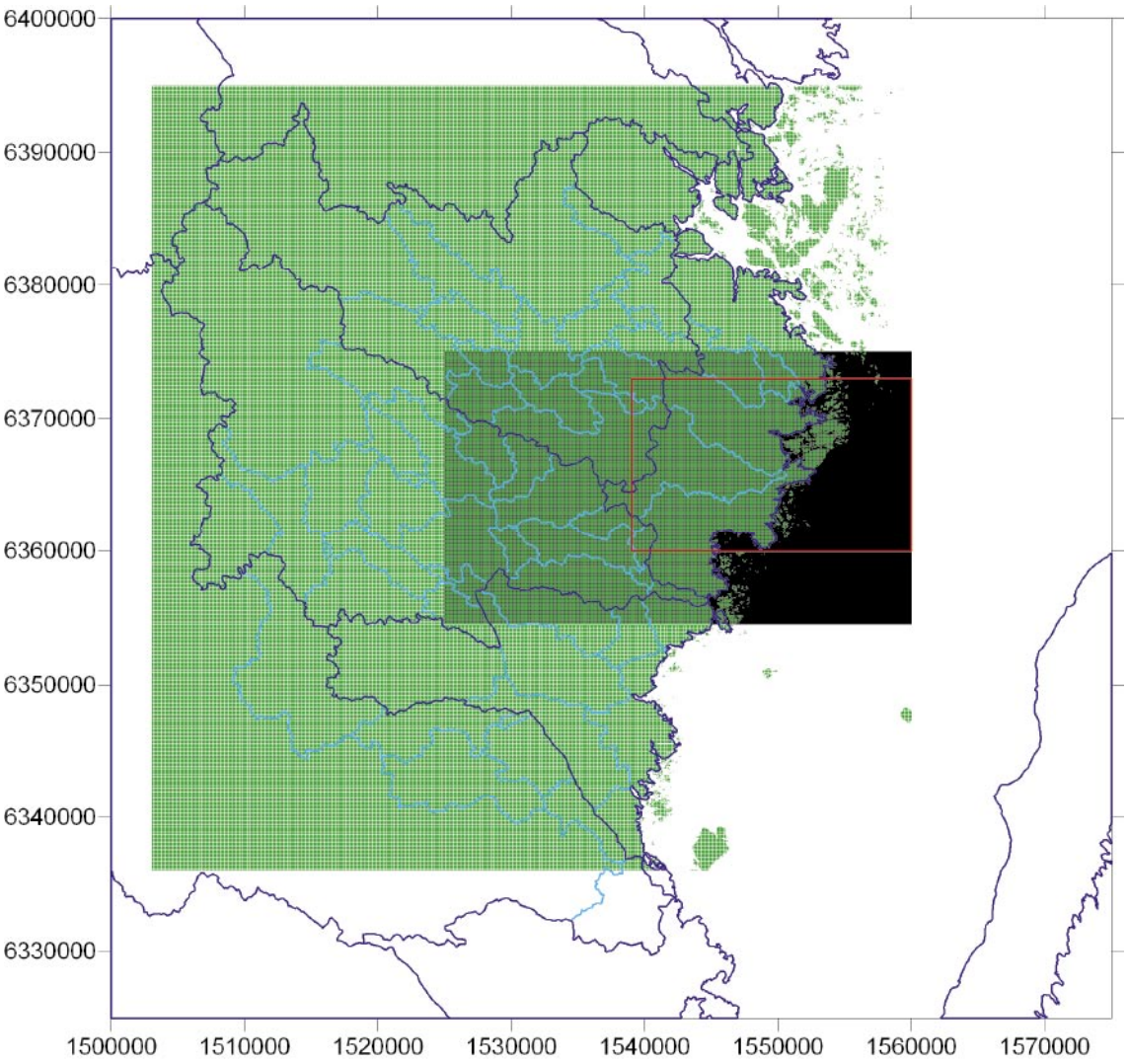

Figure 3-1. *Overview of available data 10 m topographic data (dark green), 50 m topographic data (light green), regional water divides (dark blue), local water divides (light blue), and the suggested regional scale area (red).*

The position of the present catchment boundaries is shown in Figure 3-2 along with positions of boreholes KLX01 and KLX02 that have salinity data available for model calibration. In the model, the catchment boundaries are assumed to be lateral no-flow boundaries.

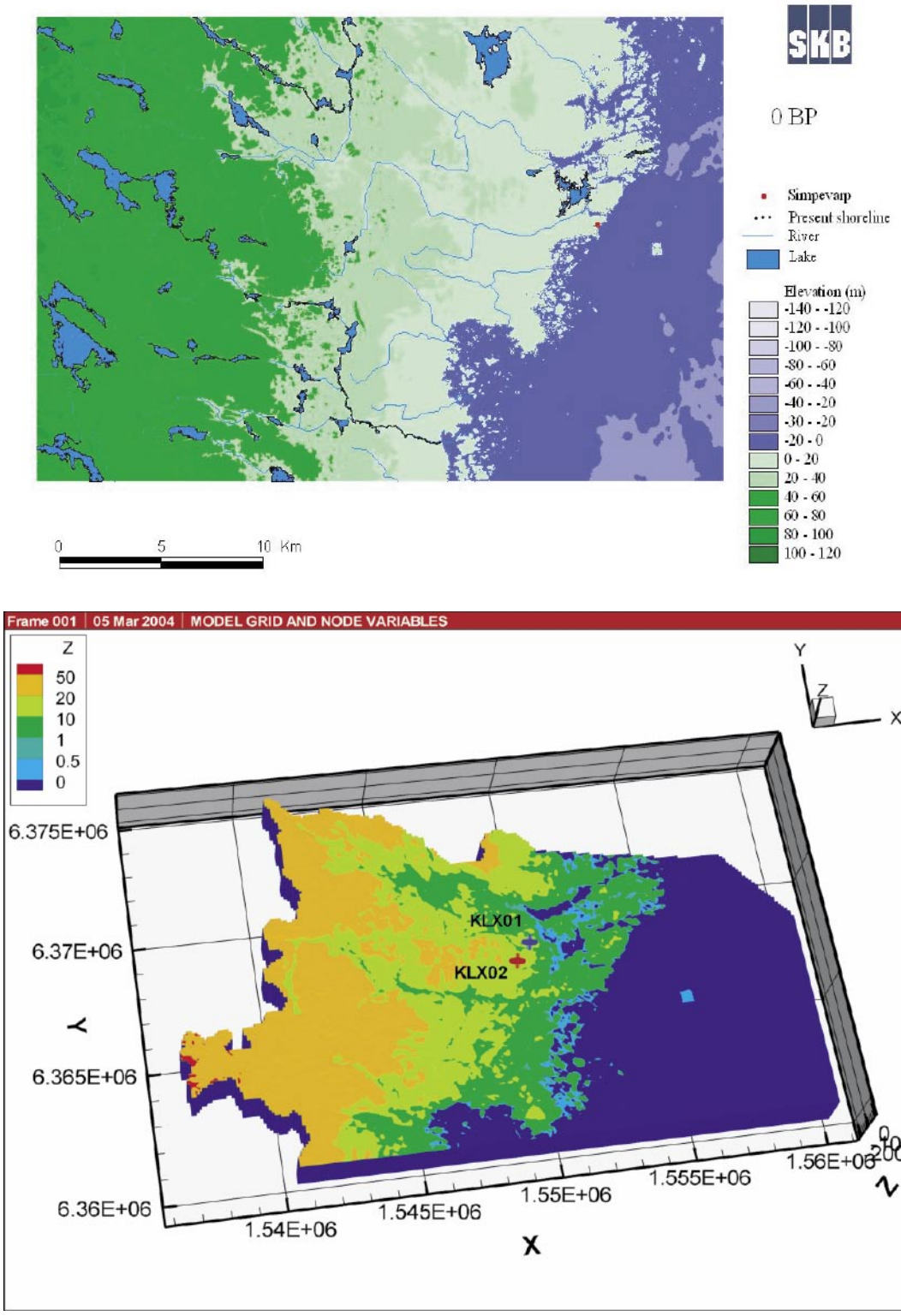

Figure 3-2. *Choice of model boundary used. Top figure shows the shoreline, rivers and elevation for present time (Follin and Stigsson, 2004) used to select the position of the boundary. The bottom figure shows the present day elevation data in the model, the positions of the vertical boundaries, and the location of the boreholes KLX01 (blue marker) and KLX02 (red marker).*

3.3 Model grid

The model grid was constructed in CONNECTFLOW as a uniform mesh of 100 m cuboid finite-elements. To represent the irregular boundary shape associated with the water-divides elements were deleted outside of a set of boundary segments. The top surface of the grid was mapped to the topographic surface and a thin parallel layer was inserted 3m below the surface to represent the Quaternary deposits. The base of the model was extended to –2300 masl and subdivided into a relatively fine vertical discretisation to represent salinity gradients around the base of the model. This was found to be a useful approach to stabilising numerical effects that arise near the Dirichlet salinity boundary condition on the base during the Version 1.1 modelling of the Forsmark site. Figure 3-3 shows the finite-element mesh used for both the DFN upscaling and the CPM groundwater flow and transport modelling. The grid contains 709032 elements in total. Linear finite-element interpolation was used in the CPM model with nodes at element corners.

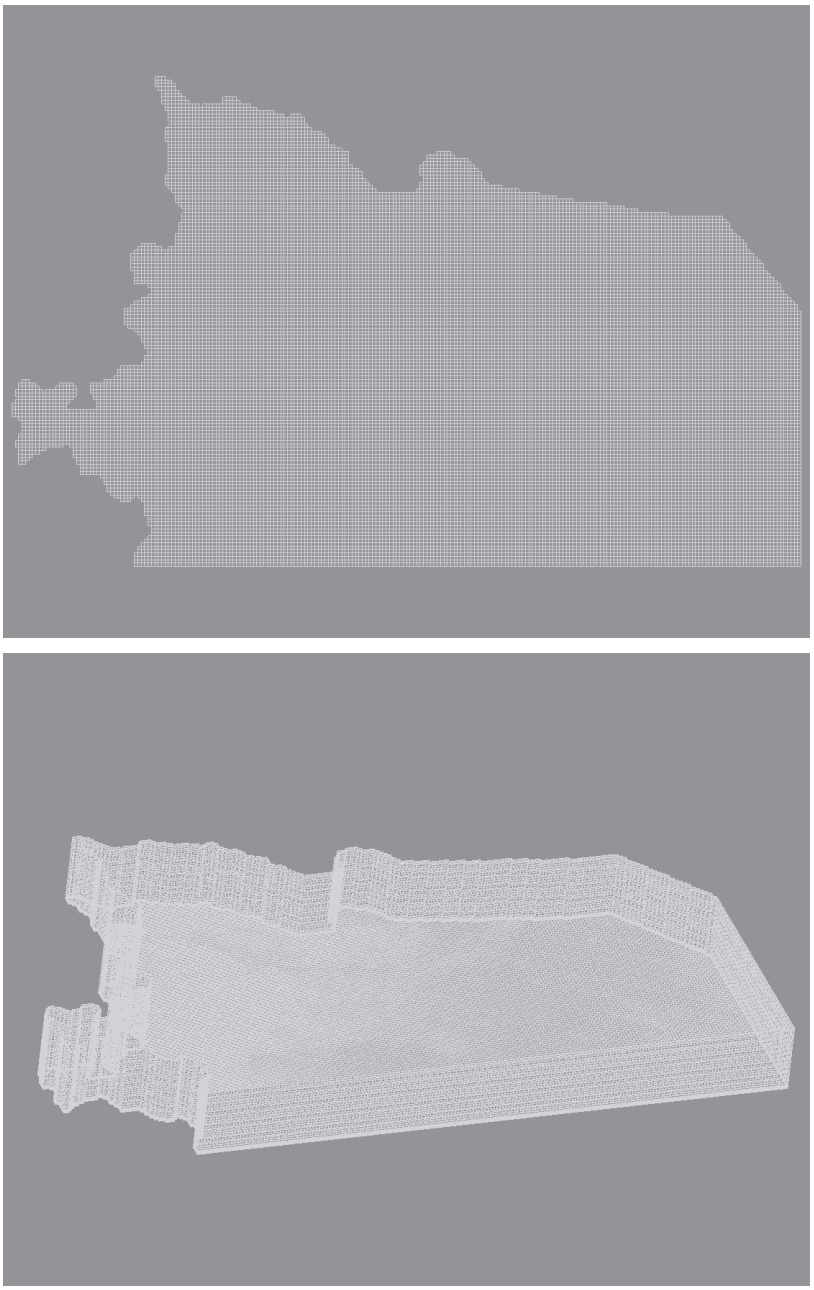

Figure 3-3. *The finite-element mesh; map view from above (top), oblique view (bottom).*

3.4 Fracture conceptual model – DFN models

The definition of the DFN model for Simpevarp was based on geometric data from Äspö (TR-02-19) and on the length and transmissivity data from Forsmark 1.1. A number of variants were suggested in the TD to quantify sensitivity to the DFN data. These were based on a higher fracture intensity (P32) or a higher fracture transmissivity. The stochastic model was split into 4 orientation sets as detailed in Table 3-2. The fracture intensity was based on the ratio size of P10c (all conductive fractures) for KLX02 to P10c for KFM01A at Forsmark multiplied by the P32c used at Forsmark for the upper 400 m of rock (see TD-POM_V1.1). The fracture intensity for conductive fractures can be interpreted using either a static criterion (using the core characterisation data) or on a dynamic criterion using the Posiva flow-log. The uncertainty between these two possible criteria for conductive fracture P32 motivated the two cases proposed in the TD, Table 3-3.

Table 3-2. Four fracture sets (TR-02-19, Table 3-15).

Fracture set	Mean pole trend	Mean plunge	Dispersion	Model	% of fractures
1	262	3.8	8.52	Fisher	24.9
2	195.9	13.7	9.26	Fisher	32.06
3	135.9	7.9	9.36	Fisher	25.92
4	35.4	71.4	7.02	Fisher	17.12

Table 3-3. Two cases for fracture intensity are considered.

Case	P32c	Comment
1	0.0371 m^2/m^3	
2 (optional)	0.1855 m^2/m^3	Case 1 increased 5 times

The fracture size model and spatial distribution is described by a CCDF from Task 6 modelling (IPR-03-13, app A, exponent D) with:

- Fracture sizes generated between L = 100–1000 m.
- Powerlaw distribution.
- Parameters (minimum length (Lmin), exponent (D)) = 100, 2.6.
- Poisson spatial model.
- Constant relative intensities throughout the entire model domain.

Fracture transmissivity is directly correlated to length as defined in Table 3-4.

Table 3-4. Transmissivity assignment: $T=aL^b$ m^2/s.

Case	a	b	Comment
1	$2.47 \cdot 10^{-12}$	1.791	Same as Forsmark v 1.1
2 (Optional)	$24.7 \cdot 10^{-12}$	1.791	Optional case

Other parameters were suggested in the TD for fracture aperture and storativity. These were not used in the CONNECTFLOW model. Instead spatial uniform values were used for porosity and storativity since it was considered that it would be easier to interpret results in the first instance using a simplified parameterisation for porosity and storage.

Initially, the DFN data was used to create some simple block models to gain an understanding of equivalent CPM properties, primarily the permeability tensor, on the scale of the finite-elements (100 m). It would be possible to compute the distribution of permeability on other scales such as the 5 m, 20 m and 100 m packer-interval scales to calibrate the fracture conceptual model with flow observation from KLX02, for example. A block size of 1 km was to study the equivalent CPM properties. Examples of the DFN block models are shown in Figure 3-4 and Figure 3-5.

Figure 3-5 demonstrates the direct correlation between fracture transmissivity and length. This network is reasonably well-connected although some of the smaller fractures around 100 m could be isolated. Also the fracture spacing would appear to be of the order of 100 m, so if the clock is divided into 100 m elements, then some elements may not be crossed by a fracture and so have zero permeability.

Two extra versions of the DFN model were considered in the simulations to quantify some uncertainties in the DFN parameterisation.

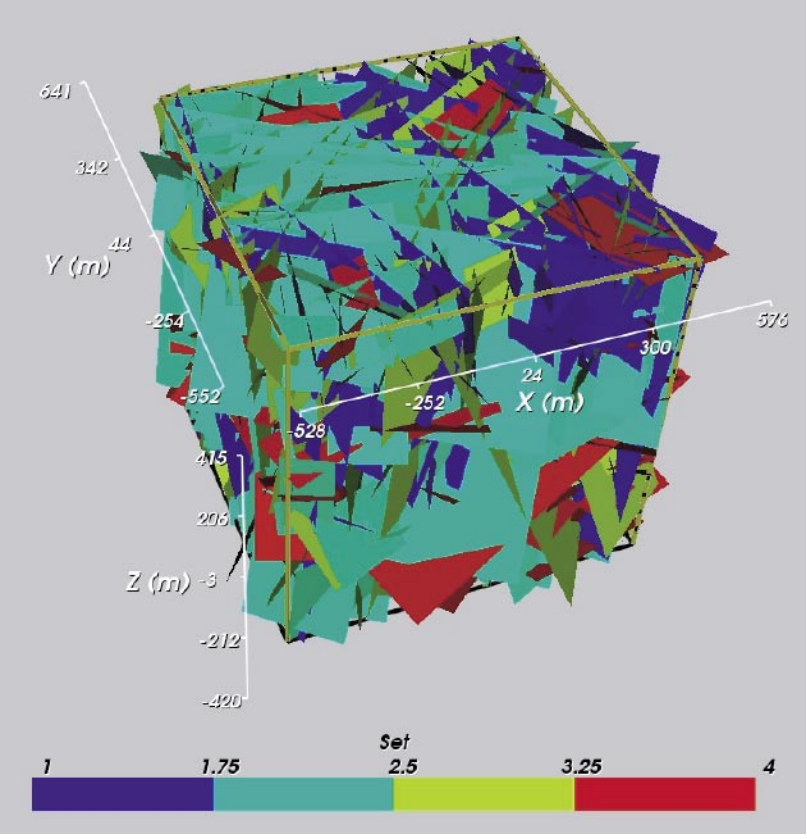

Figure 3-4. *Four sets of fractures in DFN-model Version 1 in a conceptual 1 km block.*

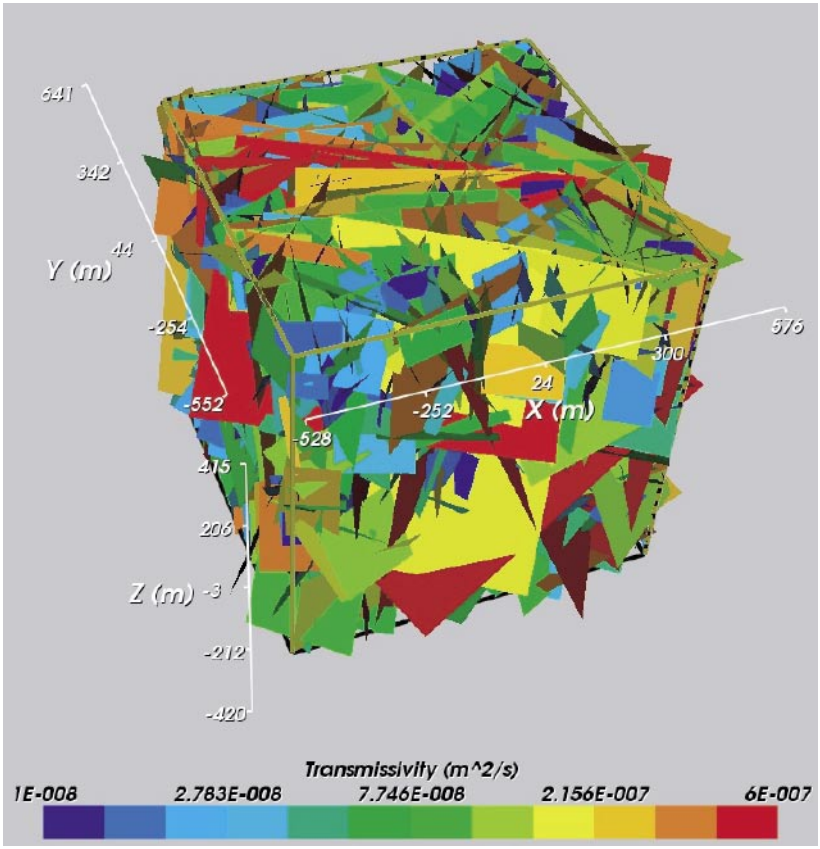

Figure 3-5. *Log T for the sets of fractures in DFN-model Version 1 in a conceptual 1 km block. Fractures are coloured Log (T).*

These versions were:

1. Version 2: a higher conductive fracture-intensity P32 of five times higher than in variant 1.
2. Version 3: a truncation of the fracture length data of 50 m rather than 100 m to see if there is a sensitivity to the choice of removing small-scale fractures from the DFN for modeling flow on the regional-scale.

Otherwise Version 1 was used in the variant simulations. Figure 3-6 shows the DFN block model, again 1 km, for the version with a higher P32. Figure 3-7 shows the DFN model with additional fractures with lengths scales 50–100 m. Clearly both of these DFN versions are well-connected (many fracture intersections per fracture) and upscaling these models for 100 m elements will give any elements with zero permeability. Figure 3-7 shows that although adding in the smaller fractures in Version 3 increases the connectivity, because of the correlation between transmissivity and length, the extra fracture small do not necessarily carry much flow.

To obtain a permeability field for the groundwater model, the generated DFN models are converted into a CPM of equivalent flow properties. Figure 3-8 shows an illustration of this where the three DFN models, Versions 1 to 3, are upscaled for 100 m blocks. The method for doing this is described in Section 2.3. In order to get a measure of the spatial variability of the upscaled permeability, values are calculated for an array of adjacent 100 m sub-blocks. In this case, upscaled permeabilities were calculated for an (9, 9, 9) array of 100 m blocks. For accuracy, (see /6/), the 1 km block is actually split into overlapping blocks of 200 m size and flow calculations are performed on the 200 m blocks, and then

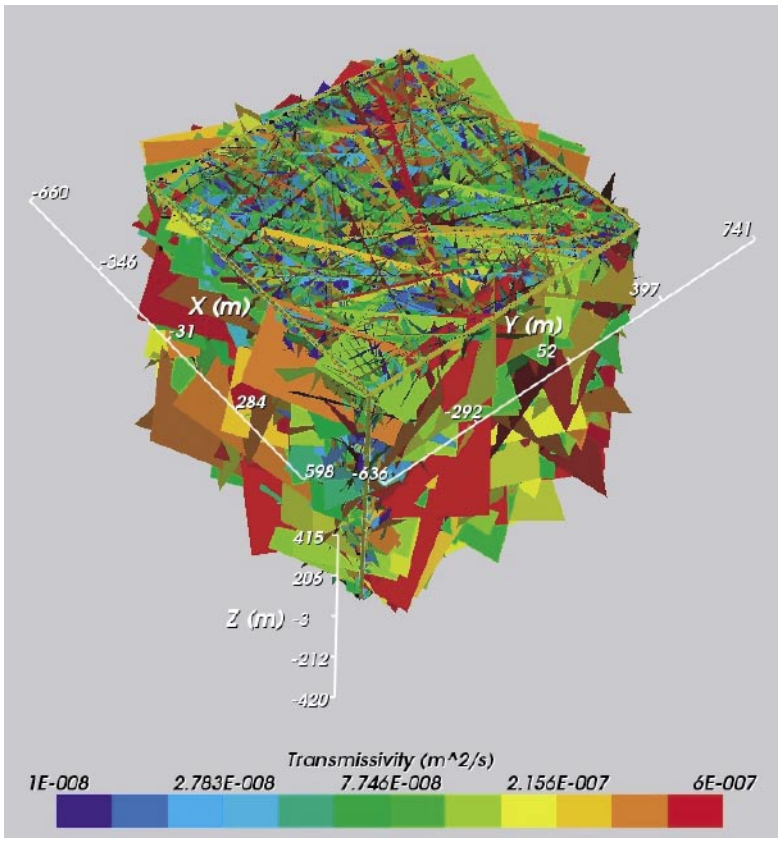

Figure 3-6. *Log (T) for the sets of fractures in DFN-model Version 2 in a conceptual 1 km block. Here P32 is a factor of five higher than in Version 1.*

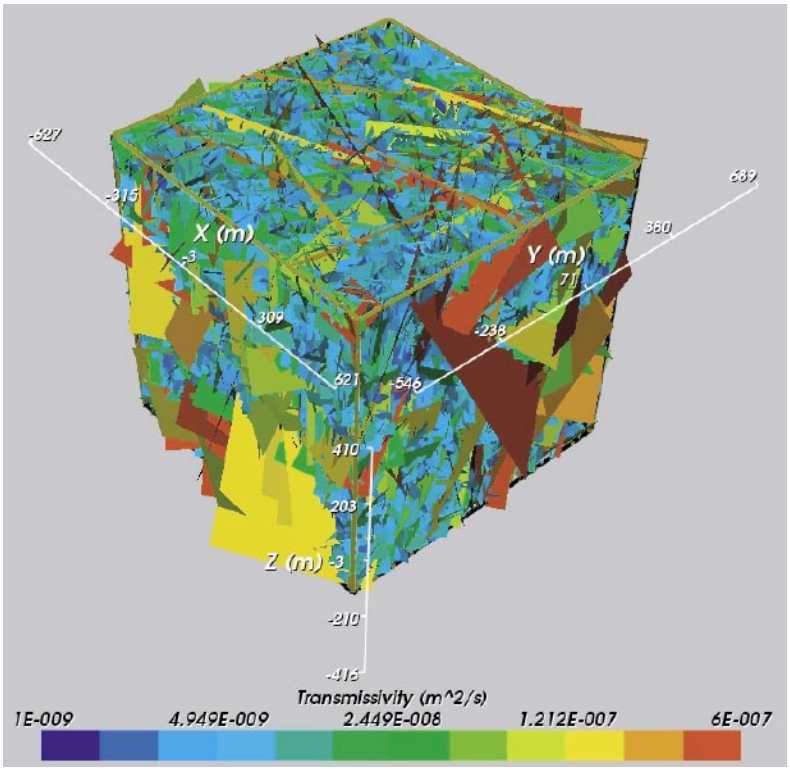

Figure 3-7. *Log T for the sets of fractures in DFN-model Version 3 in a conceptual 1 km block. Here, the size distribution starts at 50 m whereas 100 m is used as the lower limit in Version 1.*

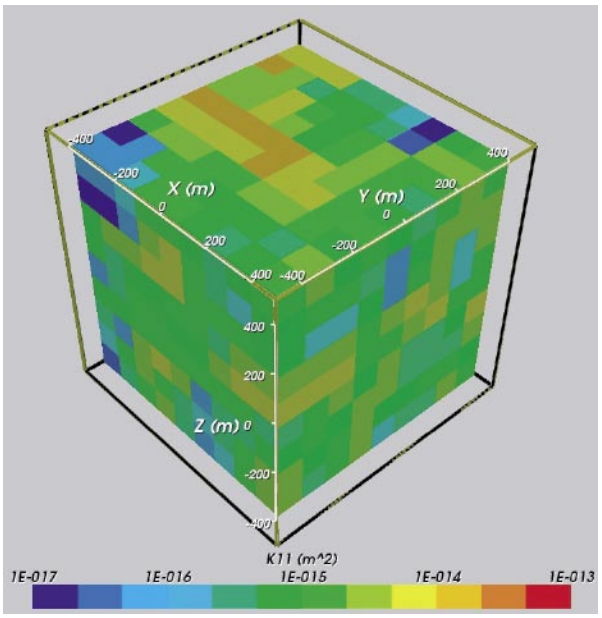

a)

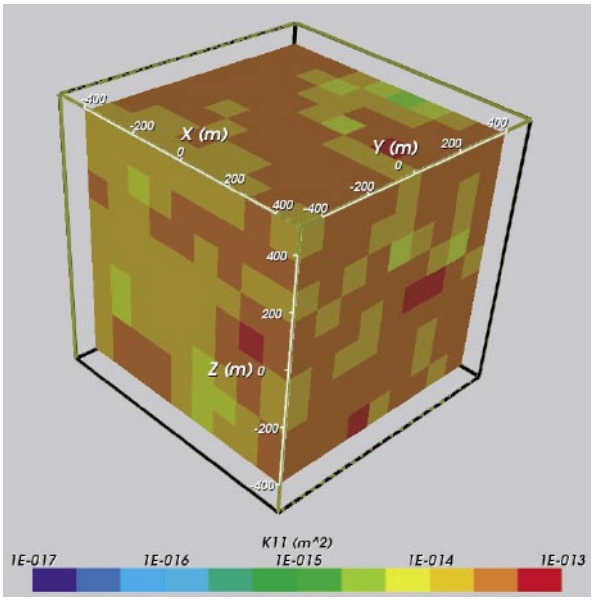

b)

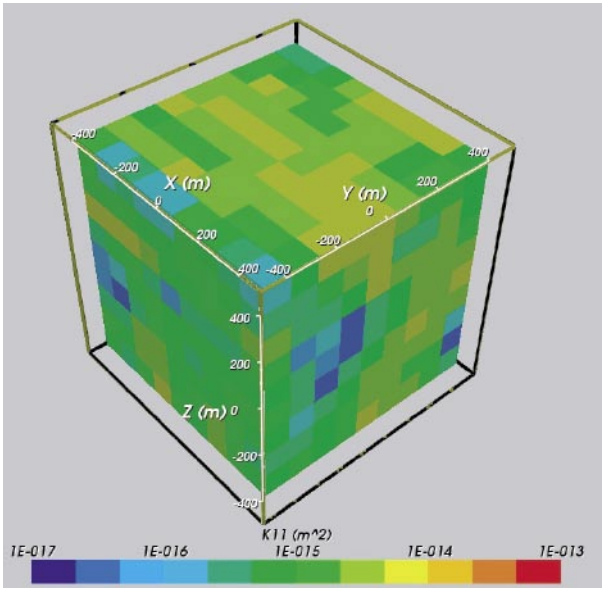

c)

Figure 3-8. *Upscaled equivalent permeability Log (k11) (m^2)on a (9, 9, 9) 100 m grid, a) Version 1, b) Version 2 and in c) Version 3.*

the fluxes are computed across the faces of the central 100 m cube for use in fitting an equivalent CPM permeability tensor on a 100 m scale. The reason for using a 200 m block is to avoid over-predicting the permeability by inclusion of flow through short-cuts of fractures that just cut corners, say, of the flow simulation domain and don't really represent flow through a network of inter-connected fractures. The choice of a 200 m block is in a sense arbitrary, but it should be about one fracture length larger than block scale required.

Note, in Figure 3-8 sub-blocks are coloured by Log (K11), the permeability in the E-W direction. The colour range is 10^{-16} to 10^{-13} m^2. To convert to hydraulic conductivity these numbers need to be multiplied by 9.8e6. Visually, Versions 1 and 3 are of similar magnitude, although Version 3 is more homogeneous due to the enhanced connectivity of small fractures. Clearly Version 2 is a much higher permeability.

These results can be presented as a statistical distribution using sub-block as a data value. For an (9, 9, 9) array of blocks we have 729 data values. Figure 3-9 shows the distribution of the geometric mean permeability (the mean of the principal components of the permeability tensor) for the three DFN versions. The geometric mean is used as a simple scalar for comparison.

For DFN Version 1, the distribution of permeability has a small, but long tail toward low permeabilities suggesting there are some 100 m blocks have get very little flow or uni-directional flow i.e. a single fracture. DFN Version 3 displays a very similar distribution, but there few values below $1.0 \cdot 10^{-16}$ m^2 ($K=1.0 \cdot 10^{-9}$ m/s) due to the extra connectivity provide by the smaller 50–100 m fractures. This would suggest it is valid to truncate the DFN model at a threshold of about 100 m for the purposes of modeling bulk flows on the regional-scale for 100 m elements, although in practice no elements should have a hydraulic conductivity less than about $1.0 \cdot 10^{-9}$ m/s, because the smaller scale fractures that have been omitted

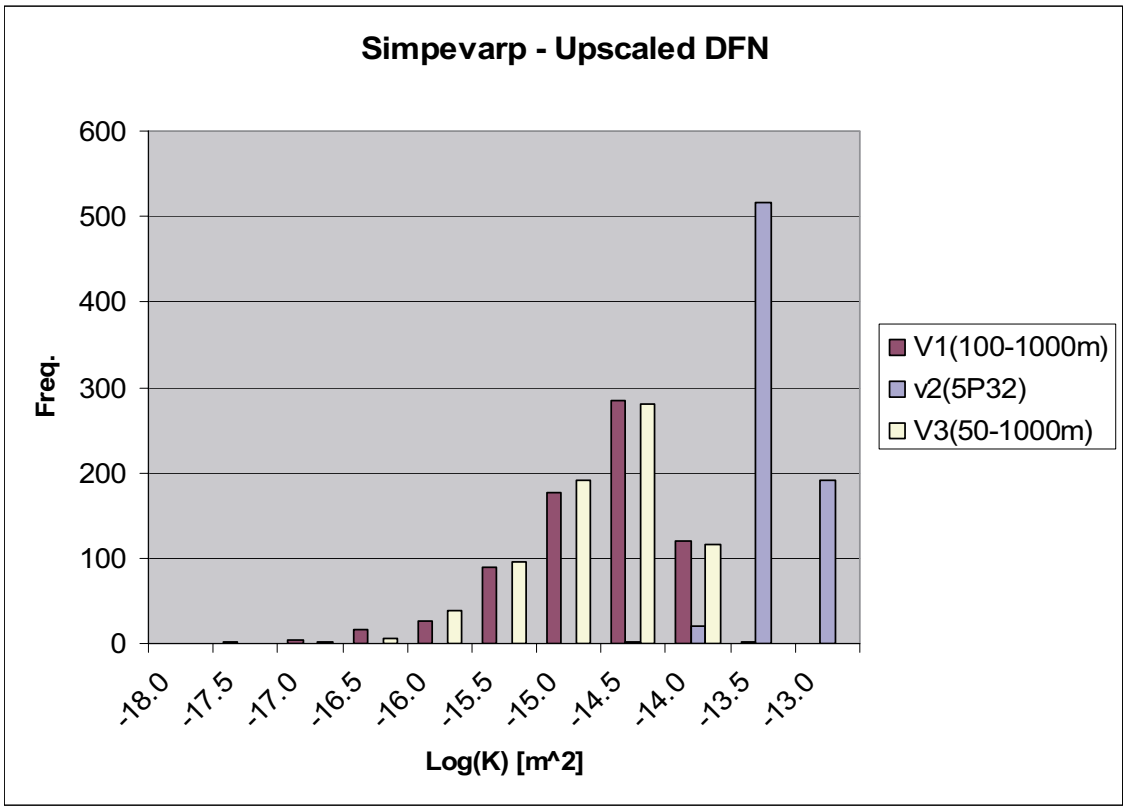

Figure 3-9. *Histogram of k_g in 100 m cells for the upscaled DFN-models. V1 is Version 1, V2 is Version 2 and V3 is Version 3.*

from the regional DFN give a background permeability of this magnitude. The variability in the distribution for DFN Version 1 suggests that a 100 m block is a sub-Representative Elementary Volume (REV) and that the network is not uniformly well-connected. In contrast, DFN Version 2 is a much tighter distribution suggesting a well-connected network and that 100 m is close to an REV. The median hydraulic conductivity is about 10^{-8} m/s. The permeabilities are also much higher ($K \sim 2.5 \cdot 10^{-7}$ m/s). The reason there is such a difference hydraulic conductivity, a factor 25, is because not only are there 5 times as many fracture, but the network has gone from marginally connected to very well-connected. It should be possible to use such results to compare with data from packer-test permeabilities to verify which of these models for conducting fractures is more realistic.

The conclusion that smaller scale fractures below 100 m have little effect on the bulk permeability for 100 m elements is in contrast to the finding for Forsmark. At Forsmark, the tail of the permeability distribution was increased notably by adding in fractures down to 50 m length. The difference is in part due to a slightly higher fracture-intensity here, about 20% higher, but also the different fracture length distribution. For Forsmark, the exponent D was 2.97 which gave rise to more small fractures. Since connectivity is a function of both fracture-intensity and length, then the connectivity at Simpevarp tends to be enhanced by having slightly more larger fractures.

The same upscaling technique is used for the full regional-scale DFN model. One example of the regional-scale DFN model is shown in Figure 3-10.

Figure 3-11 shows the same DFN model in close-up with the 100 m grid. There are about 320,000 fractures in this model. Figure 3-12 shows a horizontal cross-section through a 5 km by 5 km area of the DFN model at –500 masl. This demonstrates the network is reasonably well-connected even in 2D.

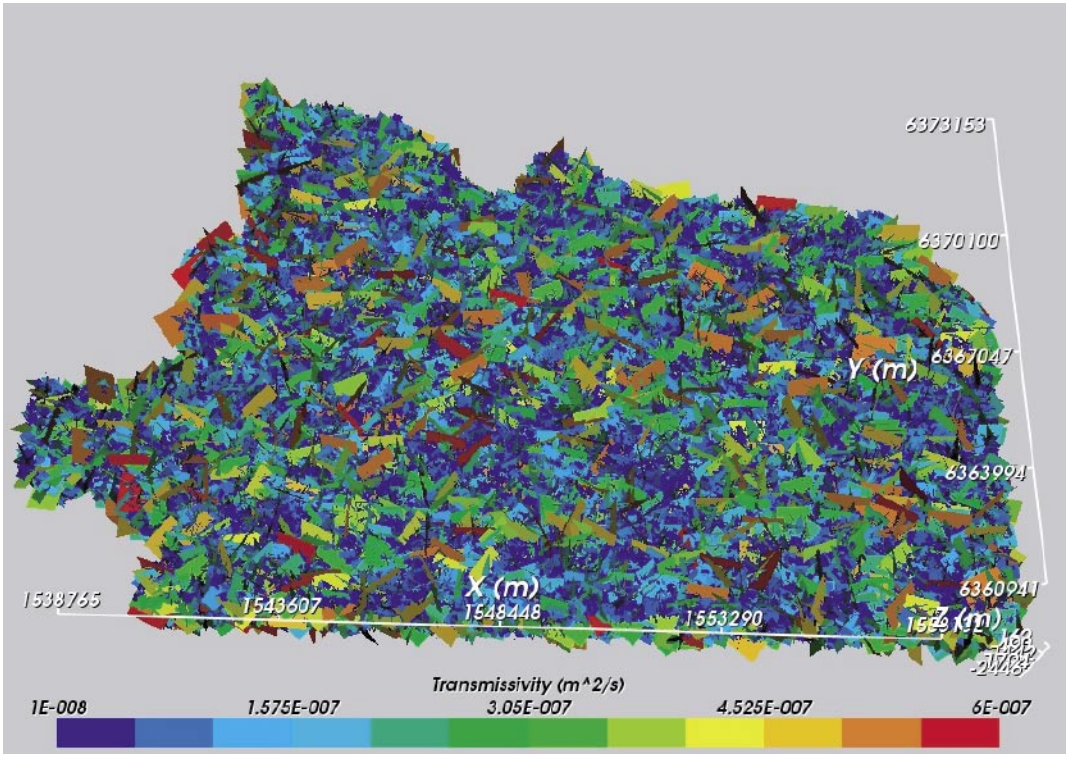

Figure 3-10. *DFN model Version 1 on a regional-scale. Fractures are coloured by Log (T).*

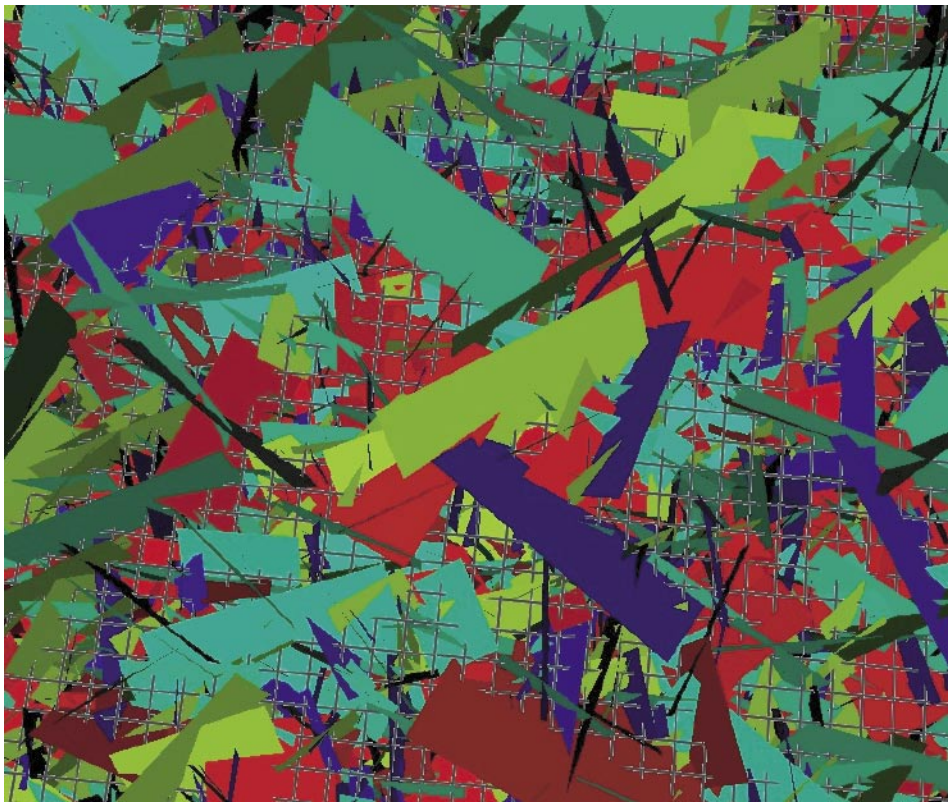

Figure 3-11. *DFN model Version 1 in focus (100 m grid, colours represent fracture sets).*

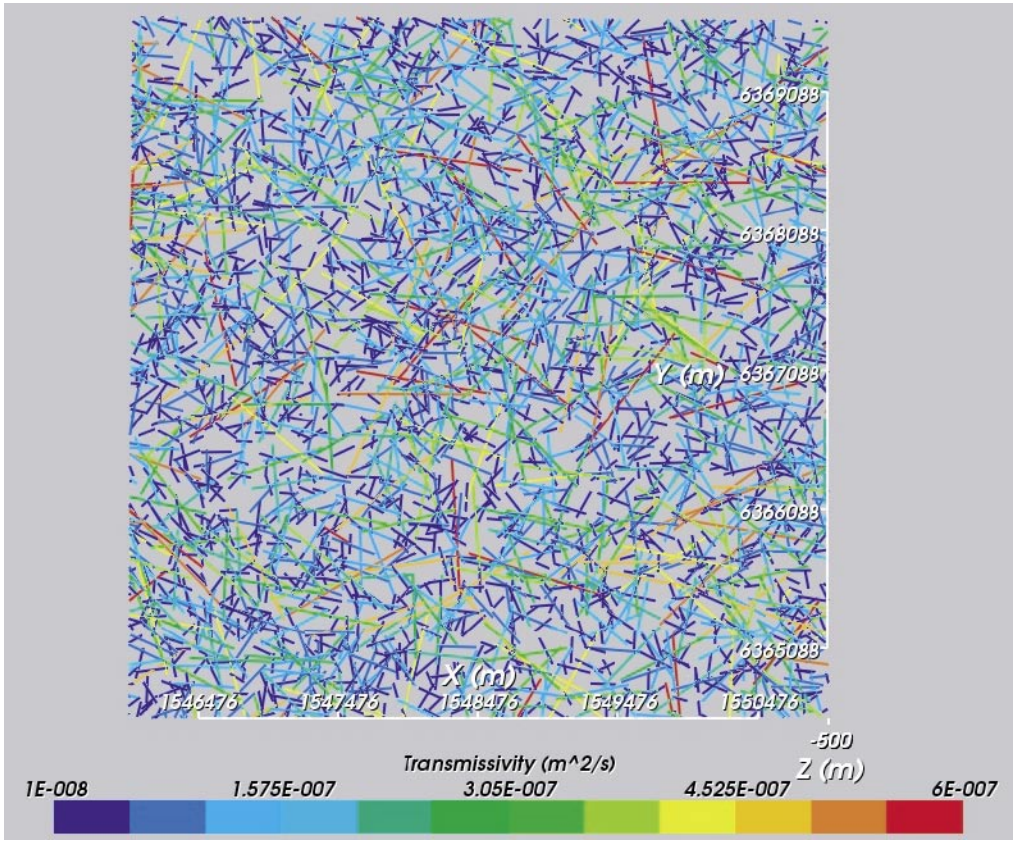

Figure 3-12. *Horizontal slice through the DFN model Version 1 (5 km cross-section at z=–500 m, colours represent Log (T)).*

3.5 CPM model

The CPM model is constructed based on the data in Task Description Version 1.5, the XML-file and the generated DFN models. An example of a model may be seen Figure 3-13. Here, the fracture zones are denoted by the colour cyan. The fracture zones terminate at Z = –2100 m while the model continues to a depth of –2300 masl. In addition the mesh is refined at base of model. These features are adaptions to avoid numerical problems (localised salt convection cells) associated with having a high transmisisvity zones that intersect a fixed high salinity at the base of the model. This approach was developed in the Forsmark 1.1 modelling.

The top layer red layer corresponds to the Quaternary deposits. The effect on permeability of the mainly sub-vertical fracture zones can clearly be seen on the sides of the model, as can some large high transmissivity stochastic fractures. Figure 3-14 shows the distribution of permeability for the CPM model with the Quaternary deposits removed to show the effect of the combined DFN and deterministic fracture zones. Clearly the fracture zones have a very strong impact on the permeability field and hence on the regional-scale flow.

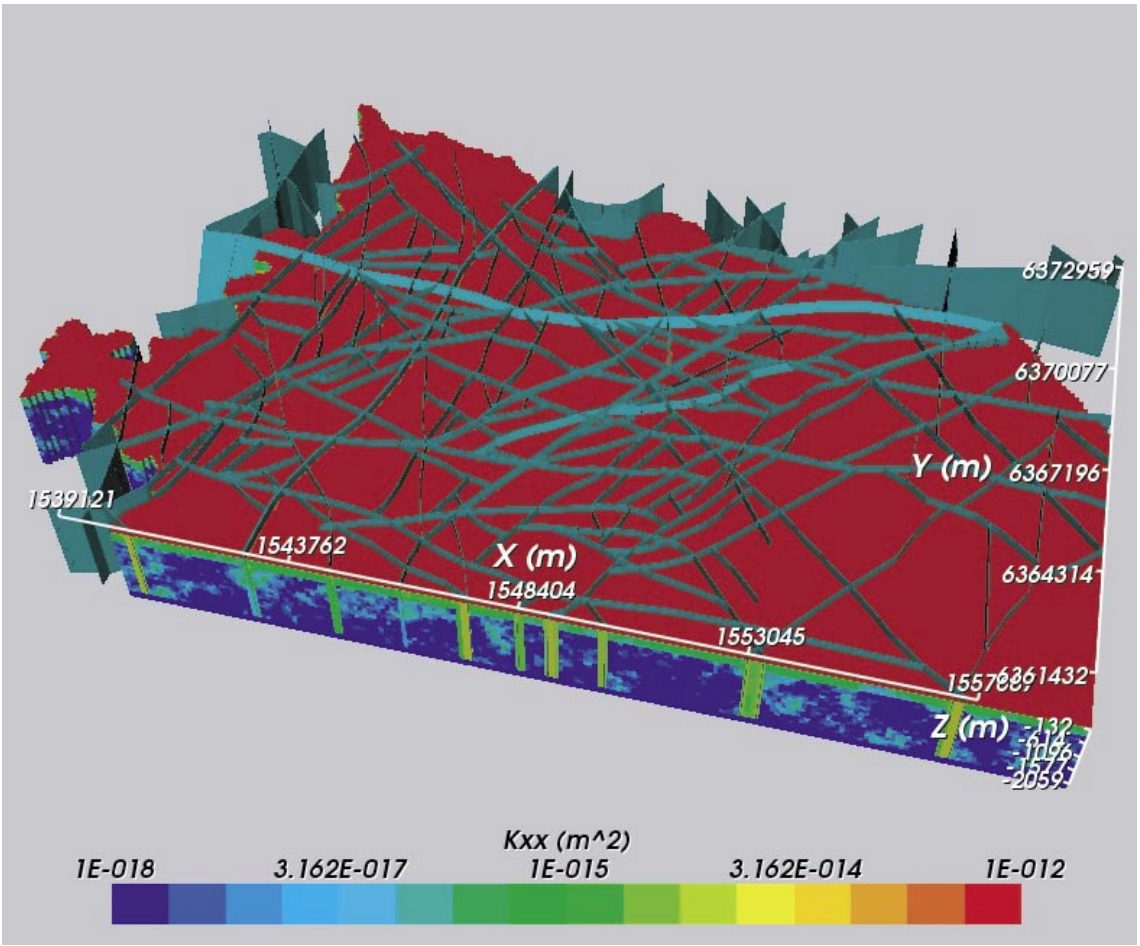

Figure 3-13. *The CPM model based on Version 1 DFN, showing the layering and fracture zones. The finite-elements are coloured by Log(k).*

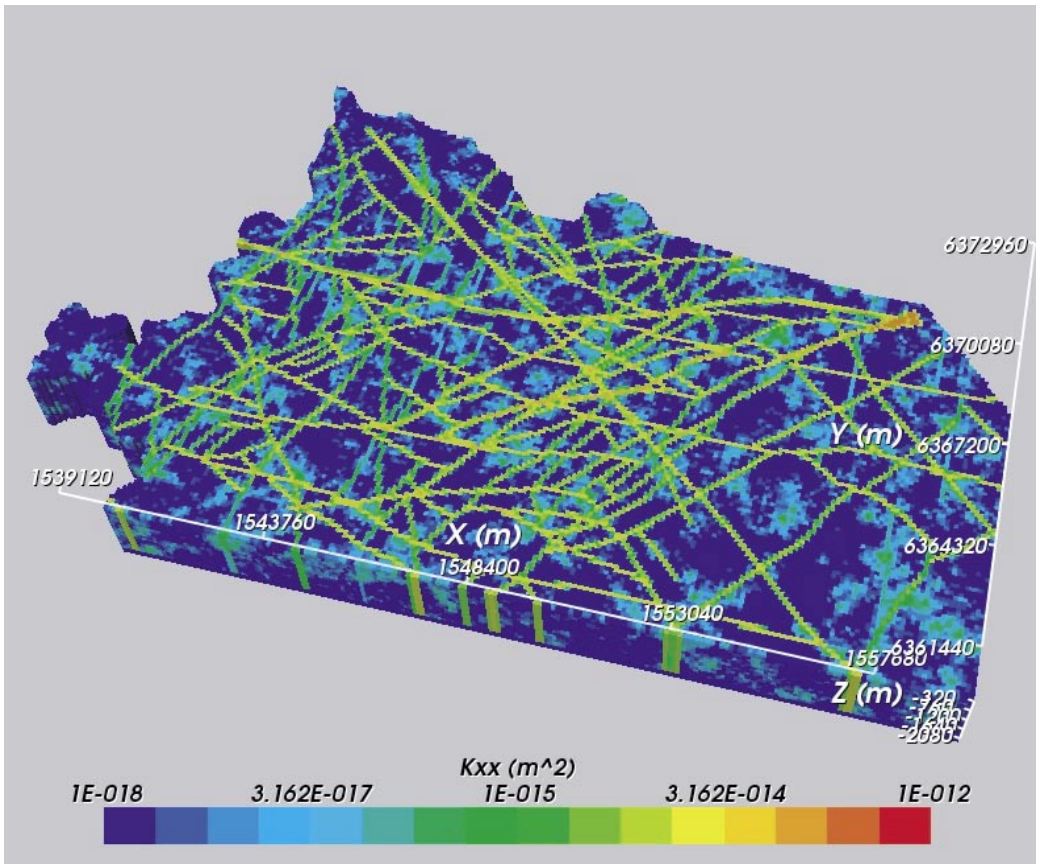

Figure 3-14. *The CPM model coloured by Log (k11) shown below the Quaternary.*

Figure 3-15 shows an example of the distribution of kinematic porosity used for the transient saline calculations. In this case, the porosity of the rock mass was to set to $2.0 \cdot 10^{-3}$ and that of the fracture zones was $3.0 \cdot 10^{-3}$, and hence the result is almost a homogeneous porosity field. A different porosity distribution was used in the particle tracking calculations. It should be noted that a transmissibility (permeability times volume) weighting was used in combining the fracture zone porosity with that of rock mass to give an effective porosity for the combined fracture zone plus rock mass in each element crossed by a fracture zone. The same weighting was used for the flow-wetted surface (FWS) in each element. A flow-wetted surface of 0.1 was used for the rock and 1.0 for the fracture zones.

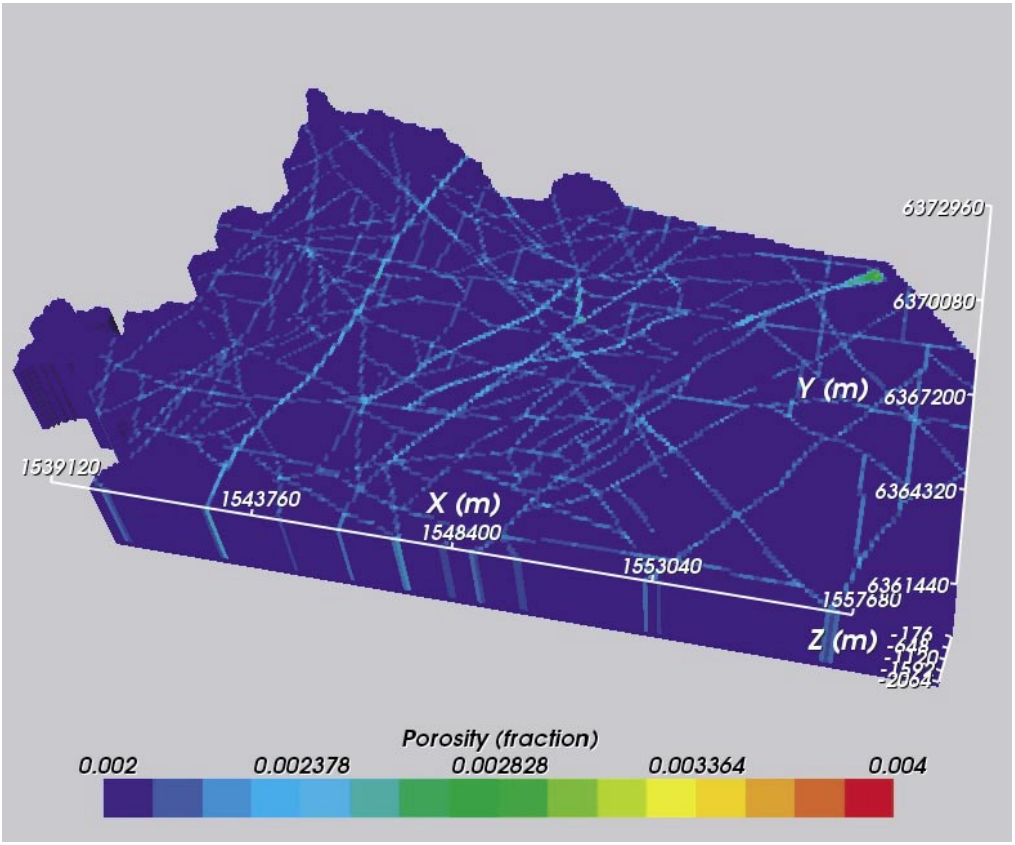

Figure 3-15. *The CPM model coloured by Log (porosity) shown below the Quaternary.*

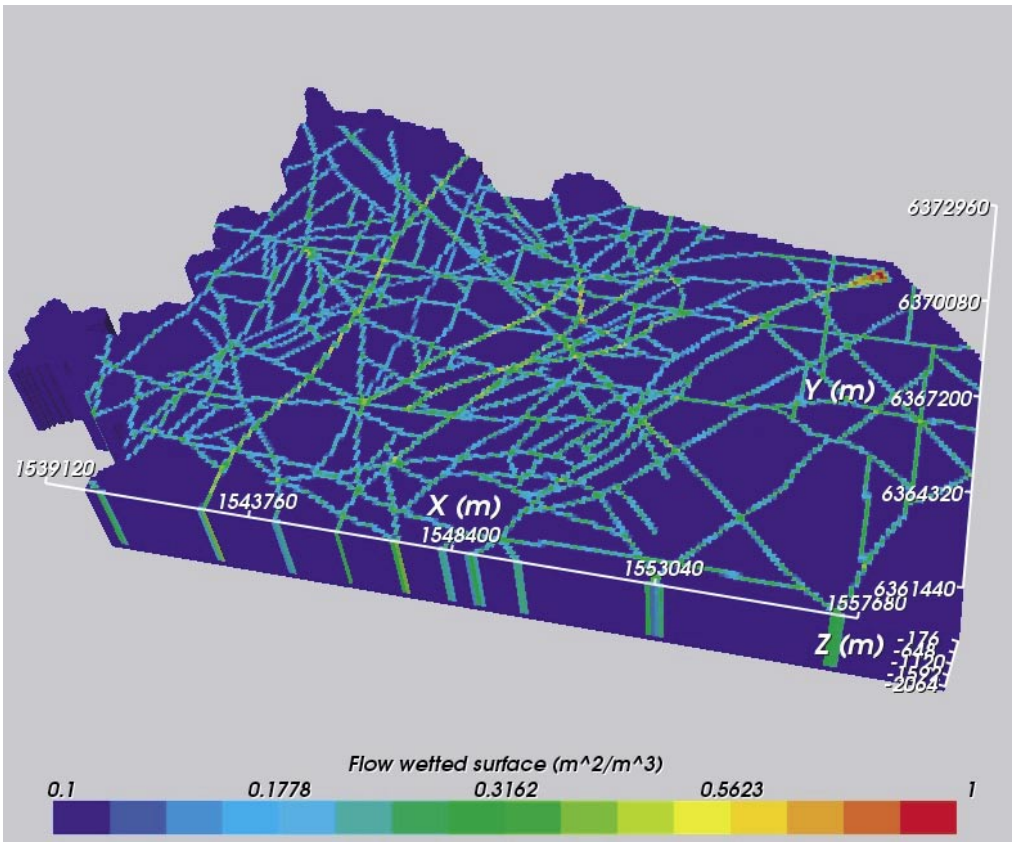

Figure 3-16. *The CPM model coloured by Log (FWS) shown below the Quaternary.*

3.6 Boundary and initial conditions

The boundary conditions used had to represent the transient processes of shore displacement due to post-glacial rebound and the variations in the salinity of the Baltic Sea. The evolutions of these two quantities are shown over the post-glacial period are shown in Figure 3-17 and Figure 3-18. The general modelling approach was to hold the model domain fixed (i.e. same x, y and z coordinates), but modify the head and salinity on the top.

The head on the top surface was set to the topographic height that evolves in time due to post-glacial rebound (see Figure 3-17). Offshore, the head was equal to the depth of the sea multiplied by the relative density of the Baltic Sea to freshwater. The evolution of the shoreline in the past is illustrated in the Appendix. For salinity a time-varying mixed type boundary condition was used such that where the instantaneous flow was inward, then salinity was set to either zero of the Baltic salinity depending on the position of the shoreline, and an outflow condition was used where the flows was out of the domain. The boundary condition on the vertical sides was no-flow. On the base, the boundary conditions were no-flow and a fixed salinity of 10%. The variation of the salinity in time is a determined input function that follows the lower curve in Figure 3-18. The green area is showing the range for the salinity. To mention an example, for the Yoldia Sea (9500–8500 BC) the maximum salinity is estimated to be in the range between 0.5 and 1.5%. Since we are using the lower limit, the highest salinity is 0.5% for this time period. Similarly, for the Litorina Sea (7000 BC–Present) the maximum salinity is estimated to be in the range in the range 1.2–1.5% and hence 1.2% is used in our simulations.

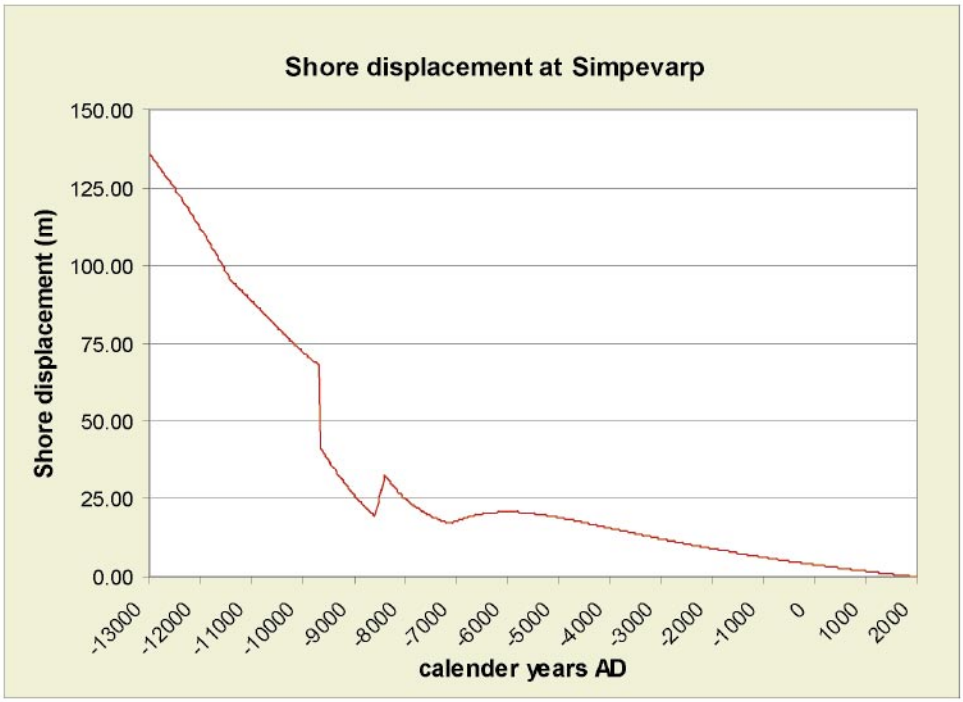

Figure 3-17. *The shore line displacement at Simpevarp.*

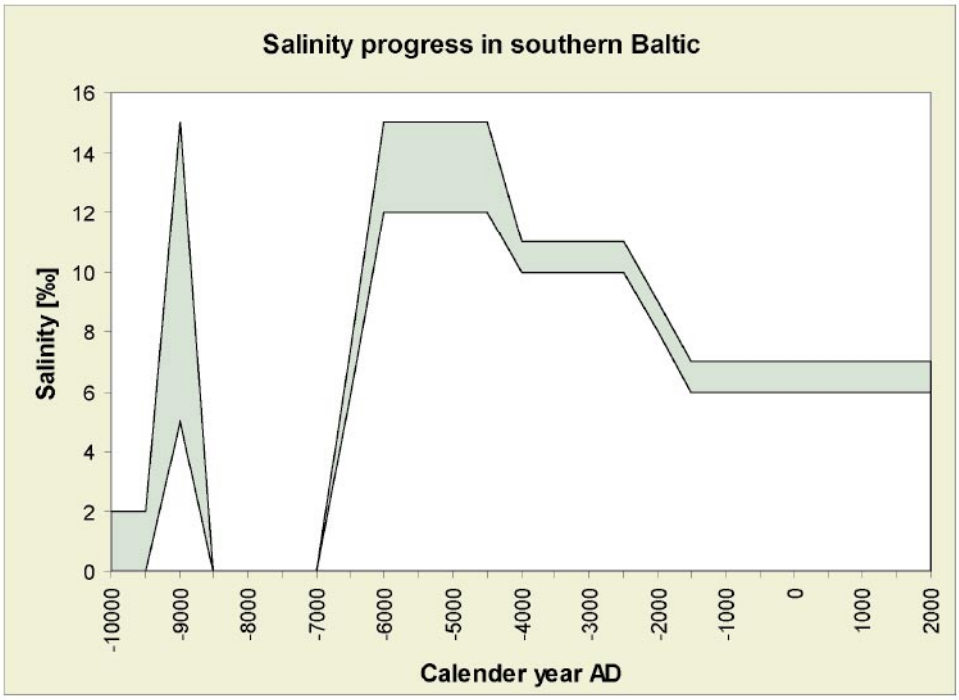

Figure 3-18. *The salinity progress in southern Baltic Sea.*

The initial conditions are uncertain and so the approach taken was to start calculations with a hypothetical initial condition based on the concept of a stratified dense brine around the base of the model below –500 to –1000 masl at 10,000 years BC well before the formation of the Baltic Sea. From Figure 3-18 this start time predates several states marine and freshwater bodies over the area, and so there should be sufficient time to minimise bias introduce by guessing the initial condition. To demonstrate whether this is the case two initial conditions are considered:

- Freshwater to –500 masl, then a linear gradient to 10% salinity at –2100 masl.
- Freshwater to –1000 masl, then a linear gradient to 10% salinity at –2100 masl.

3.7 Selection of calibration targets

To compare variant calculations and compare with observation data, the predicted salinity for the present day will be compared with the measured salinity profiles down KLX01 and KLX02. The positions of the boreholes are given in Table 3-5.

Table 3-5. Coordinates of the used calibration targets, i.e Boreholes KLX01 and KLX02.

Name	X	Y	Ztop	Length	Bearing	Inclination
KLX01	1549923.093	6367485.516	16.77	1077.99	358.119	–85.3
KLX02	1549224.090	6366768.985	18.40	1700.50	9.119	–85.0

4 Transient flow and salinity calculations

A number of simulations have been performed to investigate the influence of initial conditions, DFN-models, and kinematic porosity values. Invariants for the models considered in Version 1.1 are:

- Flow boundary condition on the top surface: Dirichlet topographic pressure.
- No-flow on vertical boundaries located at regional flow divides.
- Salinity boundary condition on top: Dirichlet value for salinity (as a function of time and shoreline) at inflows, outflow condition on outflow.
- No flow boundary condition at base.
- Specified salinity on base at –2300 masl 10%.
- Structural model and hydraulic conductivities of fracture zones.

Variants performed are:

- Initial salinity condition 1 (used for most cases): Zero salinity to –500 masl, linearly increasing to 10% at –2100 masl.
- Initial salinity condition 2 (used for one case): Zero salinity to –1000 masl, linearly increasing to 10% at –2100 masl.
- Sensitivity study of the kinematic porosity accessible to salinity in fracture zones and rock mass.
- Include smaller scale fractures.
- Higher fracture density (P32) by a factor of 5.
- Convergence check on temporal discretisation.

Data have been updated since we started our set of simulations. These changes included:

- New RVS structural model in the latest RVS version format.
- Corrections to the topographic data to fix an anomaly offshore and the position of the current shoreline.
- Change minimum background rock hydraulic conductivity from $1.0 \cdot 10^{-11}$ to $1.0 \cdot 10^{-9}$ m/s.
- New facility in CONNECTFLOW for combining fracture and rock mass properties according to a weighting by relative transmissibility rather than volume.

Due to time constraints it has not been possible to implement these late changes for the simulations reported here. Instead data as of January 2004 has been used. However, it is thought that the above changes would have any significant impact on the results or the conclusions made.

4.1 Overview of simulations

The following set of cases were performed to help develop an understanding of the hydrogeological situation at Simpevarp. Table 4-1 summarise the differences between the variants. An extra column, K/φ, has been added as a useful scalar to compare the cases as it scales with the kinematic velocity.

Table 4-1. Simulated cases.

Case	Initial condition. SALINITY of water in model	Kinematic Porosity for rock mass	K/φ (m/s)	DFN	Comment
1, pom11_1v2	1	Low porosity ($1.0 \cdot 10^{-3}$)	$8 \cdot 10^{-6}$	V1	HCD1-1-DFN1-1-QD1-1-B1-I1 ~320,000 fractures
2, pom11_1v3	1	High porosity ($5.0 \cdot 10^{-3}$)	$1.5 \cdot 10^{-6}$	V1	HCD1-1-DFN1-1-QD1-1-B1-I1
3, pom11_1v4	1	Intermediate porosity ($2.0 \cdot 10^{-3}$)	$4 \cdot 10^{-6}$	V1	HCD1-1-DFN1-1-QD1-1-B1-I1
4, pom11_1v5	1	Intermediate porosity ($2.0 \cdot 10^{-3}$)	$1.2 \cdot 10^{-4}$	V2	HCD1-1-DFN2-1-QD1-1-B1-I1 5 times higher P32 ~1,600,000 fractures dt=20 years.
5, pom11_1v6	1	Intermediate porosity ($2.0 \cdot 10^{-3}$)	$5 \cdot 10^{-6}$	V3	HCD1-1-DFN3-1-QD1-1-B1-I1 Lower truncation of L (50 m) ~4,400,000 fractures
6, pom11_1v7	2	Intermediate porosity ($2.0 \cdot 10^{-3}$)	$4 \cdot 10^{-6}$	V1	HCD1-1-DFN1-1-QD1-1-B1-I2
7, pom11_1v5vt1	1	Intermediate porosity ($2.0 \cdot 10^{-3}$)	$1.2 \cdot 10^{-4}$	V2	Same as pom11_1v5, but dt=10 years
8, pom11_1v5vt2	1	Intermediate porosity ($2.0 \cdot 10^{-3}$)	$1.2 \cdot 10^{-4}$	V2	Same as pom11_1v5, but dt=5 years

As described in Section 2.5, two different porosities were used for transient salt transport modelling and the particle-tracking for safety assessment. The different values are tabulated in Table 4-2 and Table 4-3, respectively. The physical interpretation that should be put on this difference is that first represent a total porosity based on an assumption that transients occur sufficiently slowly for salinity to diffuse into a significant portion of the rock mass. Whereas for radionuclide transport, conservative assumption need to be made that neglect the effect of rock matrix diffusion and so a fracture porosity is used for the main conductive features.

Table 4-2. Kinematic porosity values used in the transient flow and saline transport calculations.

Case	QD1–1	Rock between HCD	Fracture zones
1, pom11_1v2	$5 \cdot 10^{-2}$	$1 \cdot 10^{-3}$	$1 \cdot 10^{-3}$
2, pom11_1v3	$5 \cdot 10^{-2}$	$5 \cdot 10^{-3}$	$1 \cdot 10^{-2}$
3, pom11_1v4	$5 \cdot 10^{-2}$	$2 \cdot 10^{-3}$	$3 \cdot 10^{-3}$
4, pom11_1v5	$5 \cdot 10^{-2}$	$2 \cdot 10^{-3}$	$3 \cdot 10^{-3}$
5, pom11_1v6	$5 \cdot 10^{-2}$	$2 \cdot 10^{-3}$	$3 \cdot 10^{-3}$
6, pom11_1v7	$5 \cdot 10^{-2}$	$2 \cdot 10^{-3}$	$3 \cdot 10^{-3}$

Table 4-3. Kinematic porosity values in the particle tracking calculations.

Case	QD1–1	Rock between HCD	Fracture zones
1, pom11_1v2	$5{\cdot}10^{-2}$	$1{\cdot}10^{-5}$	$5{\cdot}10^{-5}$
2, pom11_1v3	$5{\cdot}10^{-2}$	$1{\cdot}10^{-5}$	$5{\cdot}10^{-5}$
3, pom11_1v4	$5{\cdot}10^{-2}$	$1{\cdot}10^{-5}$	$5{\cdot}10^{-5}$
4, pom11_1v5	$5{\cdot}10^{-2}$	$1{\cdot}10^{-5}$	$5{\cdot}10^{-5}$
5, pom11_1v6	$5{\cdot}10^{-2}$	$1{\cdot}10^{-5}$	$5{\cdot}10^{-5}$
6, pom11_1v7	$5{\cdot}10^{-2}$	$1{\cdot}10^{-5}$	$5{\cdot}10^{-5}$

As described in Section 1.2, part of the deliverables are safety assessment performance measures, such as travel time, canister flux and F-quotient for particle-tracks start at a regular array of points within the two local-scale areas. The areas are shown in Figure 4-1. It should be noted that transport calculations on this coarse regional-scale 100 m mesh-size grid are only tentative results. Further, no consideration was given to avoid starting particles in major fracture zones according to a minimum respect distance.

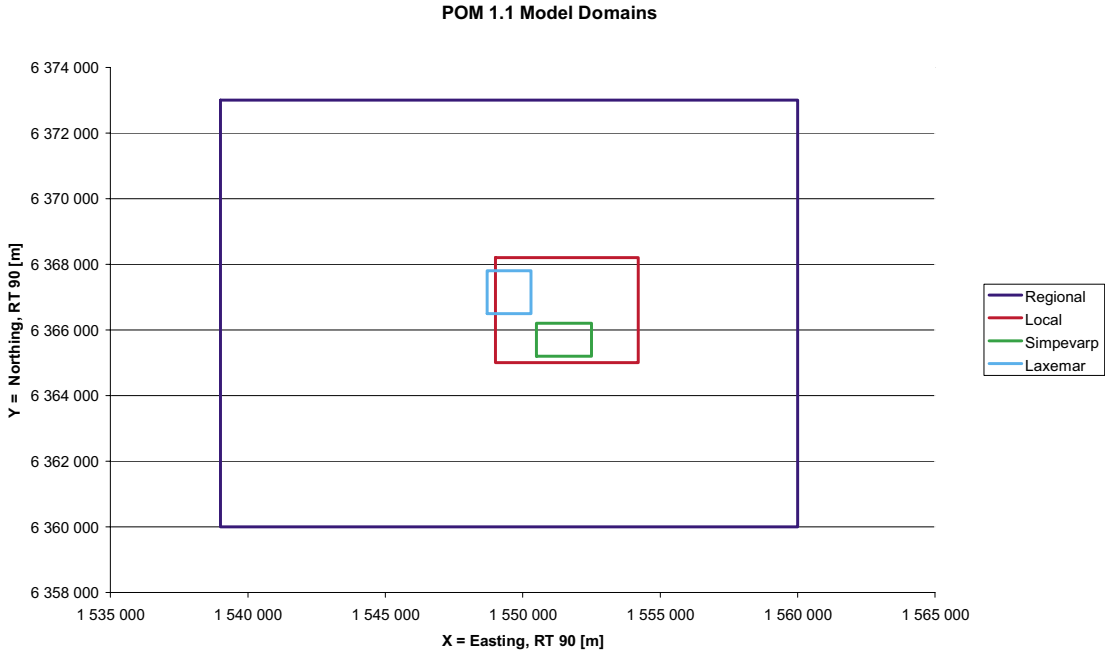

Figure 4-1. *Schematic plot of the model domains according to TD. The red square represents the original 0.2 Local-scale area. The blue and green squares represent the Local-scale areas for Laxemar and Simpevarp, respectively.*

4.2 Case 1, pom11_1v2

Case 1 is based on Version 1 of the DFN model, Initial condition1, and has a low kinematic porosity of $1.0 \cdot 10^{-3}$ leading to a relatively high value of $K/\varphi = 8 \cdot 10^{-6}$, and hence high kinematic velocities.

4.2.1 Variable density and flow calculations

Variants are compared using the following results:

- Salinity on vertical slices through the model oriented E-W and showing the borehole locations for KLX01 and KLX02;
- The evolution of salinity in the boreholes as a function of depth;
- Contours of vertical Darcy velocity at repository depth, –500 masl

A few extra plots of salinity profiles near the boreholes are given for key variants. Later in this section the predicted salinities are also compared with the field data, which unfortunately is quite sparse for Oskarshamn 1.1, at least for KLX01.

Salinity distribution

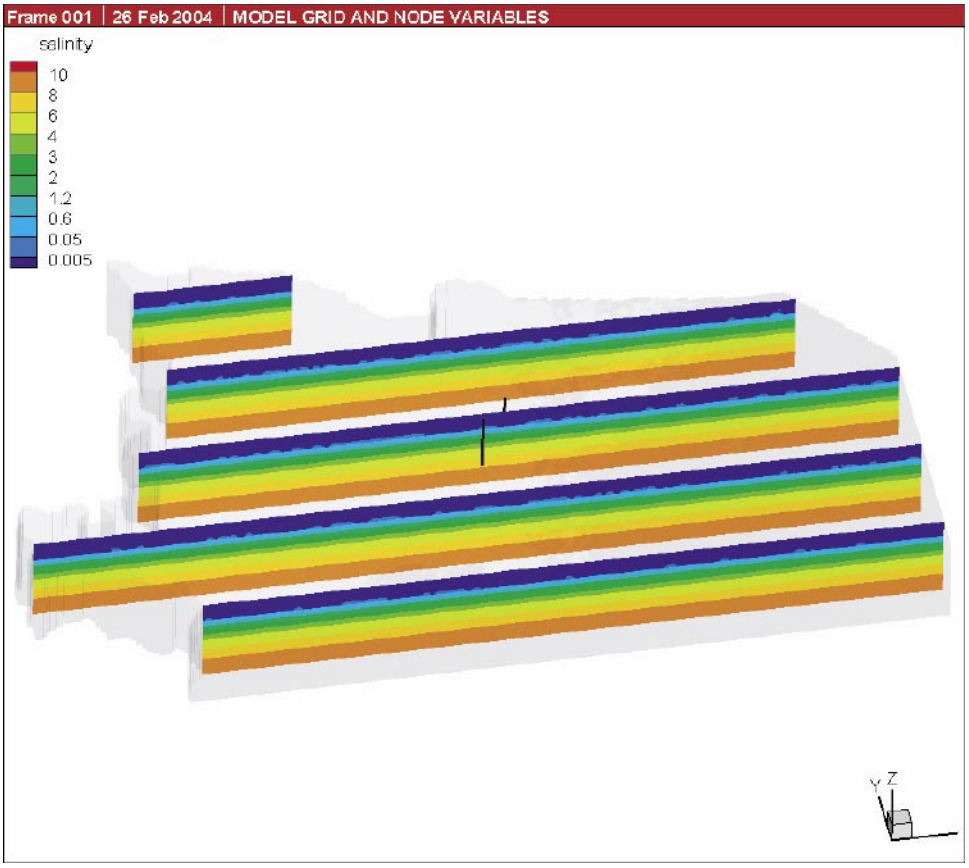

a)

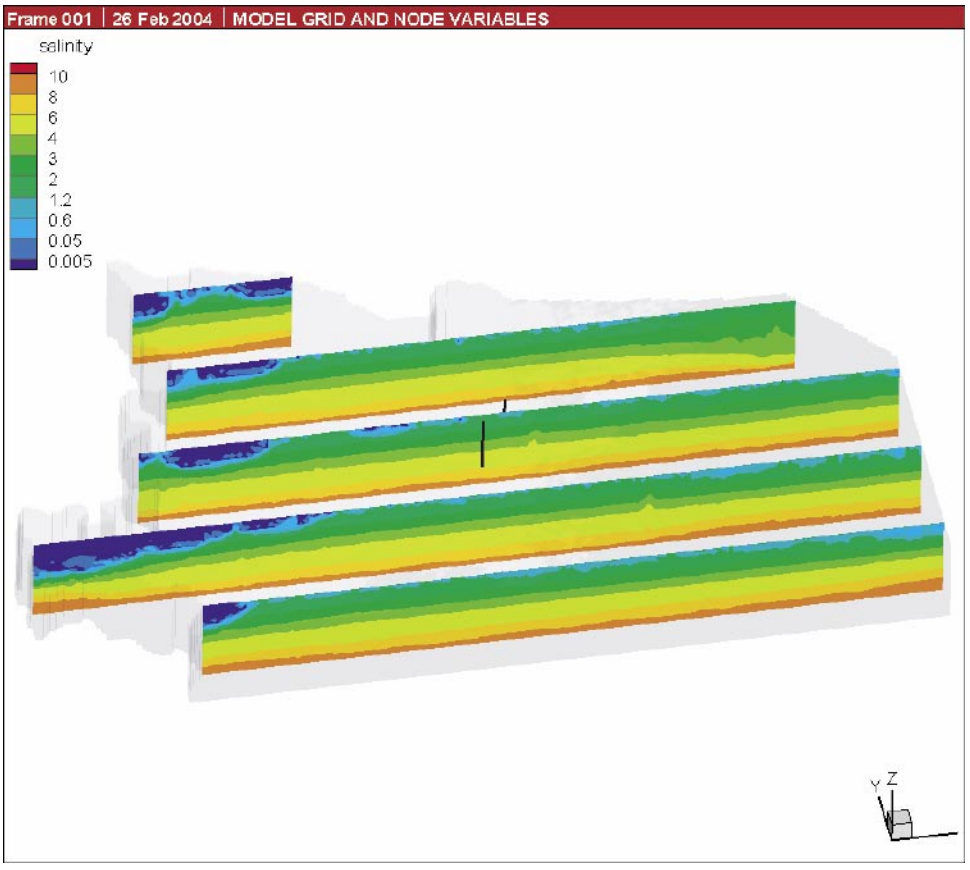

b)

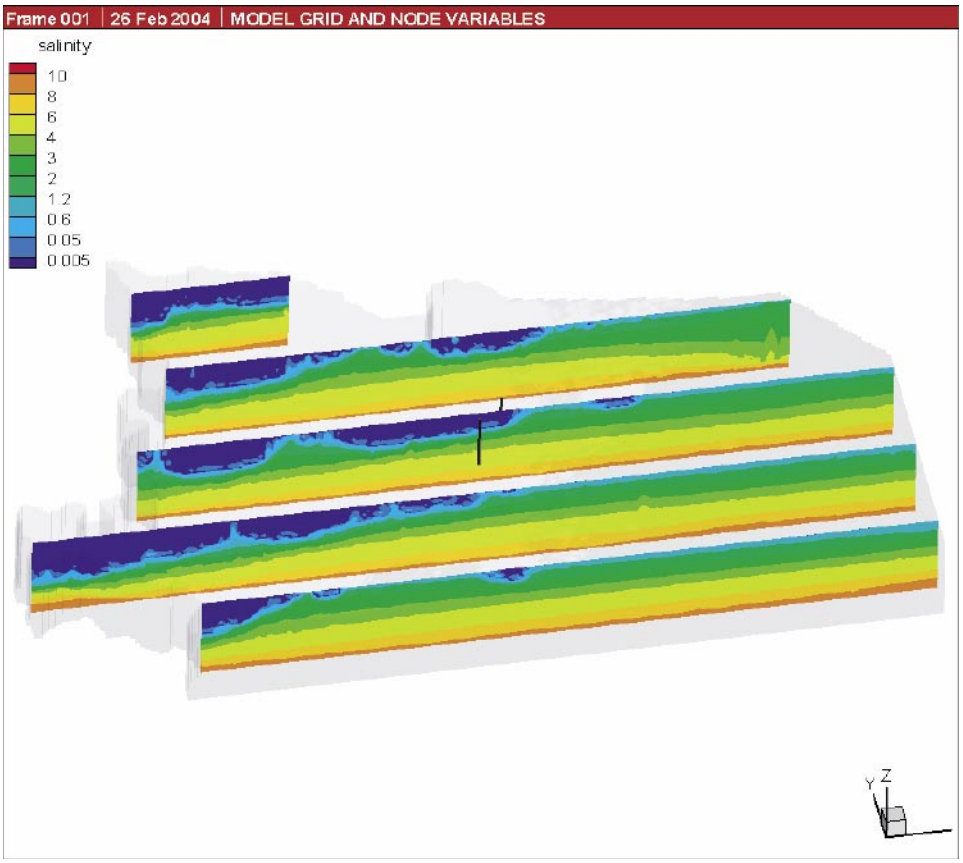

c)

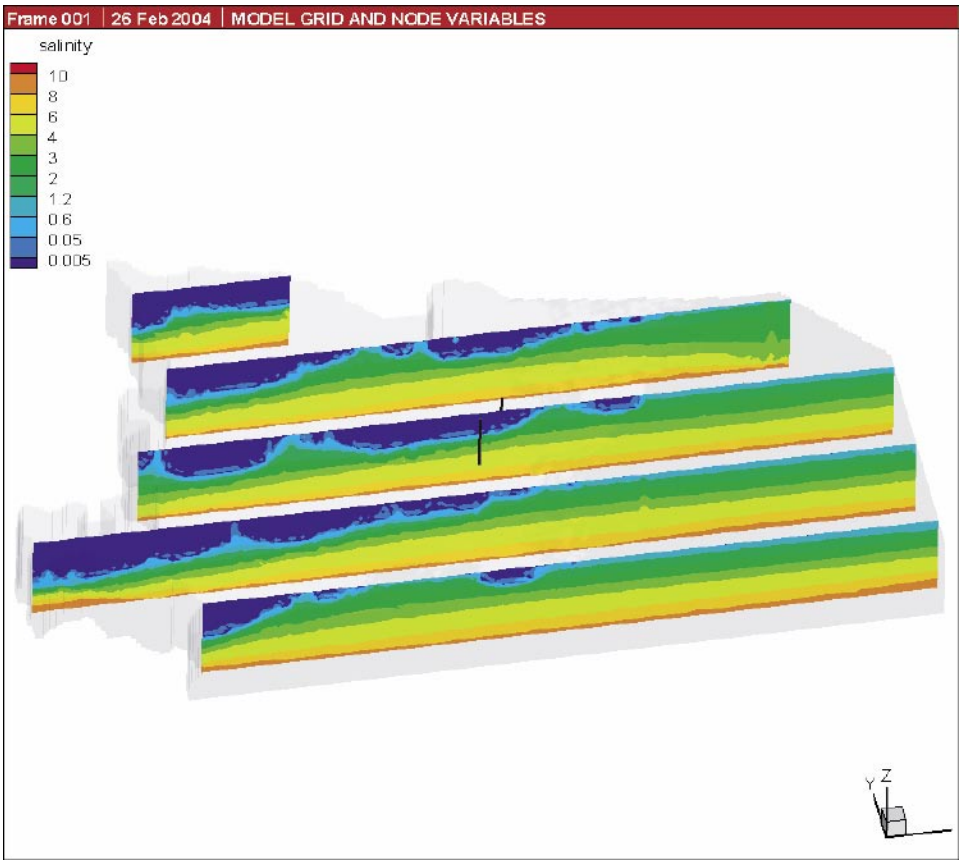

d)

Figure 4-2. *Salinity distribution in vertical slices for Case 1: pom11_1v2. The positions of KLX01 (back) and KLX02 (front) are shown. a) 10,000 BC, b) 5000 BC, 0 BC, 2000 AD.*

Figure 4-2 shows the evolution in salinity at 10,000 BC, 5000 BC, 0 AD, 2000 AD. At 5000 BC much of site is cover by the Litorina Sea which leads to an infiltration of dense brine into much of the rock. By 0AD land-rise in the West leads to a flushing of the upper rock by freshwater recharge. This continues to 2000 AD by which time the upper rock around KLX01 and KLX02 has been flushed of salinity.

The particular behaviour in boreholes KLX01 and KLX02 is shown in Figure 4-3. At 5000 BC salinity occupies the whole borehole length due to the effect of infiltration of Litorina water. However, by 0AD the profile has relaxed back toward the initial condition. Under present day conditions, the profile in KLX01 is similar to the initial condition with salinity staring at around –500 masl. In KLX02, the salinity has been pushed deeper to about –700 masl. This is a result of KLX02 being in an area of slightly higher topography and further from the coastline. Interestingly, below about –100 masl the saline interface is steeper than the initial condition. This may be physical associated with the high kinematic velocities, or it may be a result of numerical issues such as the choice time-step (20 years) and coarse grid. The issue of convergence with respect to the temporal discretisation will be dealt with Cases 7 and 8 that have the highest values of K/φ, and hence will require the smallest time-step.

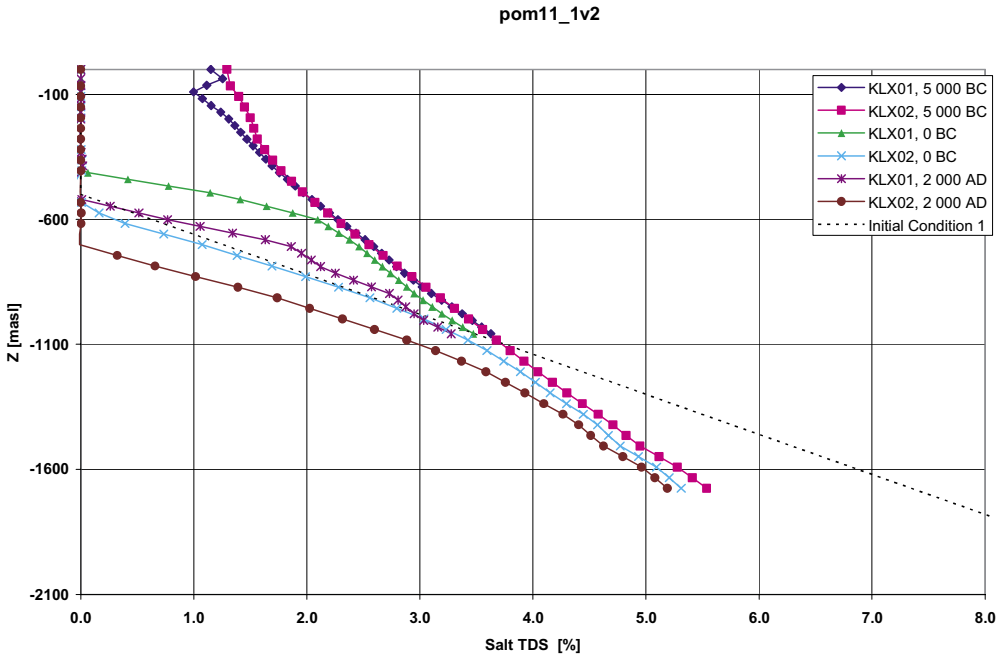

Figure 4-3. *Salinity profiles for different snapshots in time for Boreholes KLX01 and KLX02 in Case 1.*

4.3 Case 2, pom11_1v3

Case 2 is based on Version 1 of the DFN model, Initial condition1, and has a high kinematic porosity of $5.0 \cdot 10^{-3}$ leading to the lowest value of $K/\varphi = 1.5 \cdot 10^{-6}$, and hence low kinematic velocities.

4.3.1 Variable density and flow calculations

Salinity distribution

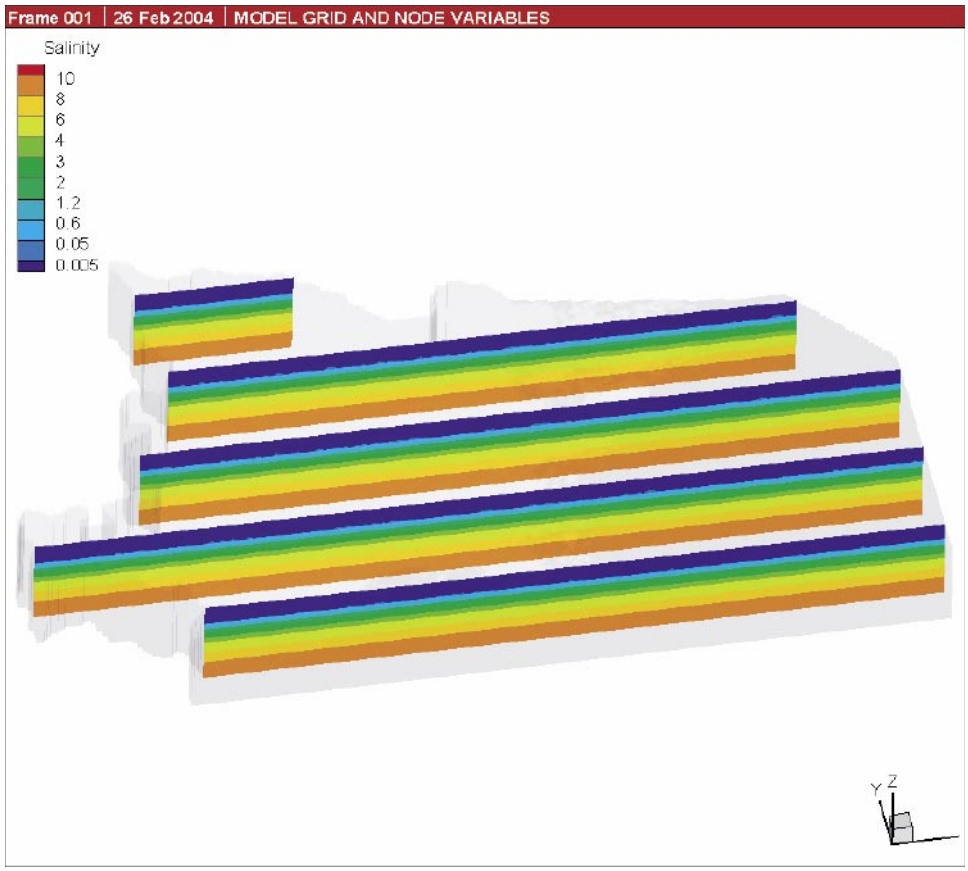

a)

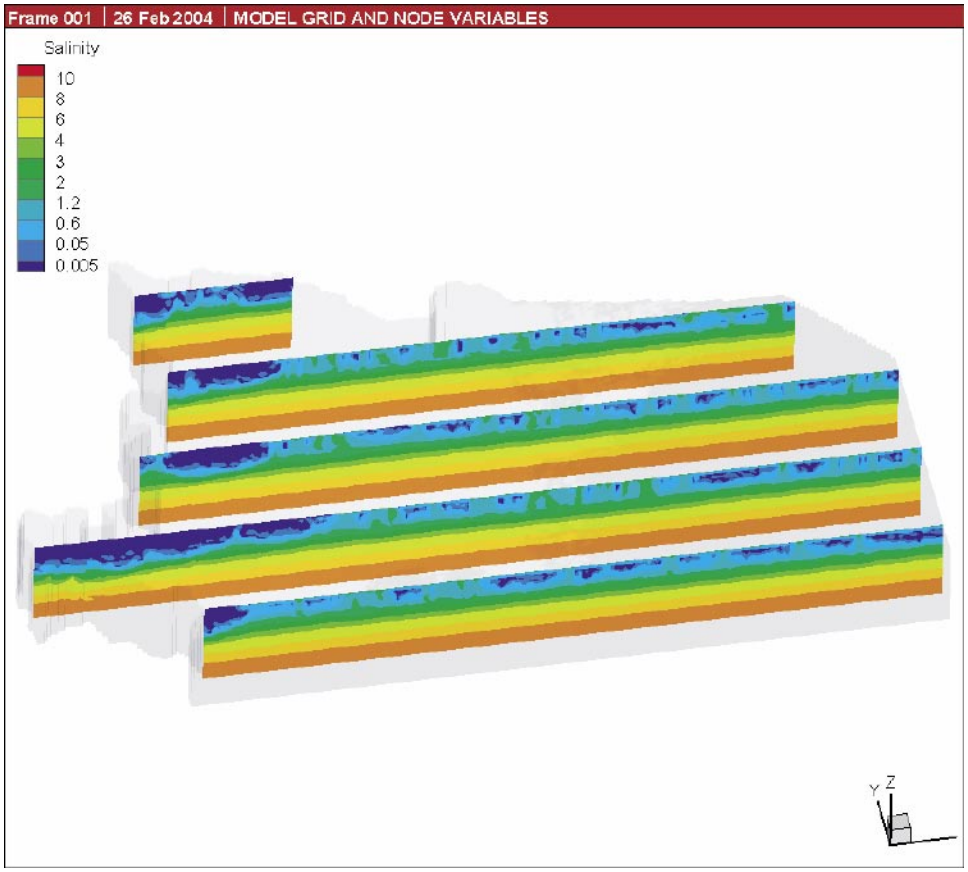

b)

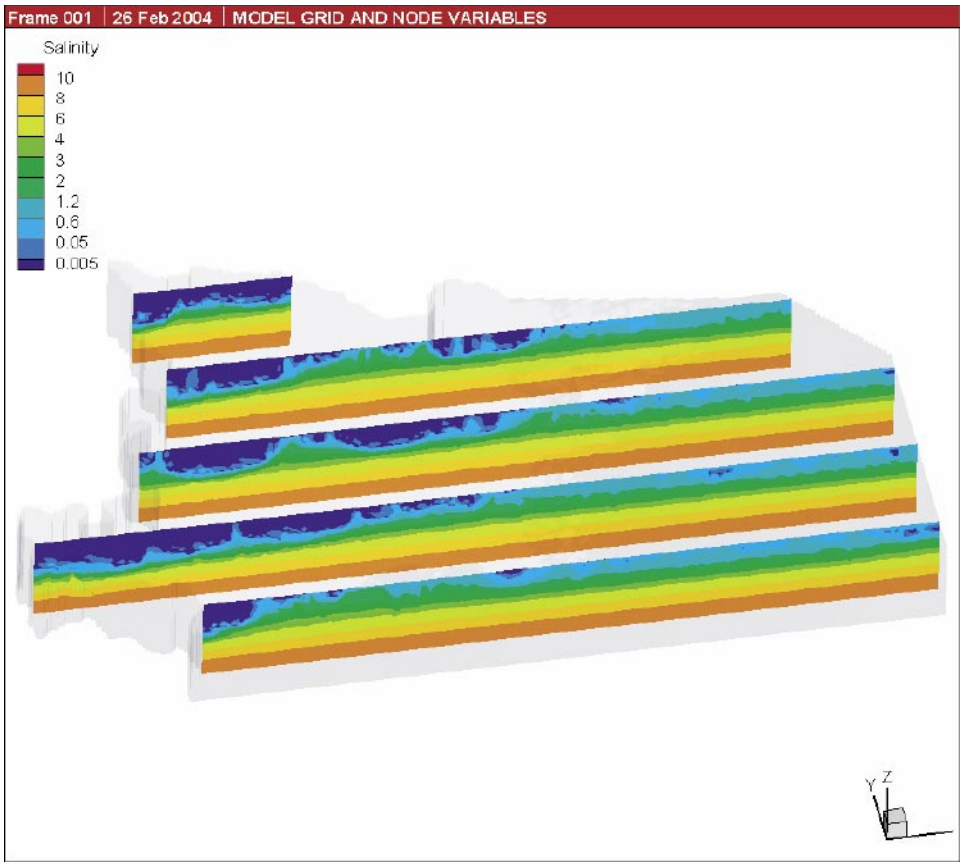

c)

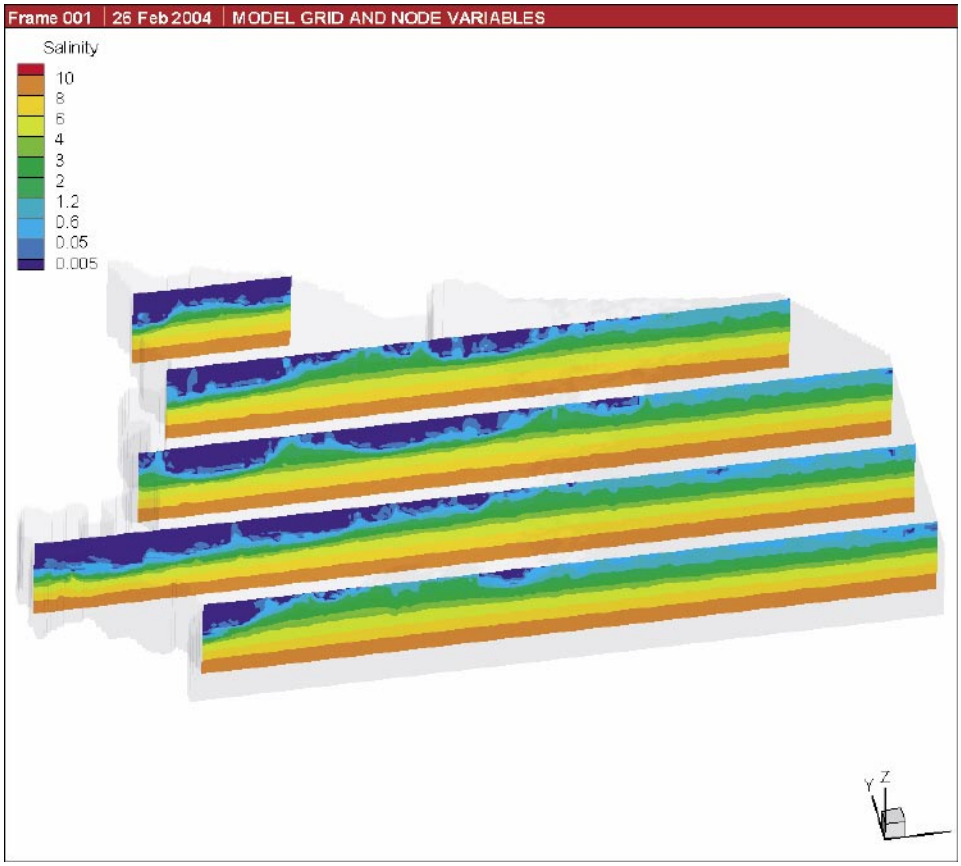

d)

Figure 4-4. *Salinity distribution in vertical slices for Case 2: pom11_1v3. a) 10,000 BC, b) 5000 BC, 0 BC, 2000 AD.*

Figure 4-4 shows the evolution in salinity for Case 2. At 5000 BC salinity is infiltrating in a more discrete way associated with the fracture zones. Presumably this is because the slower kinematic velocities give less spreading of salinity transversely away from the sub-vertical fracture zones. At a later times, the upper rock is again being flushed, but the deep rock is flushed less than in Case 1.

The particular behaviour in boreholes KLX01 and KLX02 is shown in Figure 4-5. For this case it is clear that there is very little effect on salinity below about –900 masl. In fact, the salinity profiles are unchanged from the initial guess below about –900 masl. This is interesting as it suggests for values K/φ less than about $2 \cdot 10^{-6}$ there is little flushing of the deep brine.

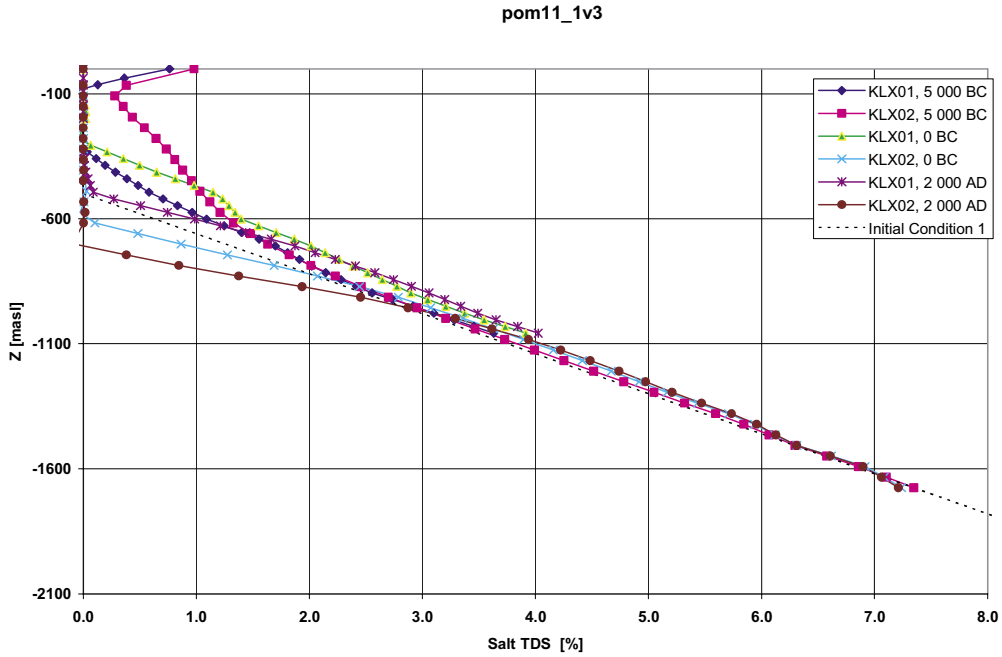

Figure 4-5. *Salinity profiles for different snapshots in time for the boreholes KLX01 and KLX02 in Case 2.*

4.4 Case 3, pom11_1v4

Case 3 is based on Version 1 of the DFN model, Initial condition1, and has an intermediate kinematic porosity of $2.0 \cdot 10^{-3}$ leading to a moderate value of $K/\varphi = 4 \cdot 10^{-6}$, and hence moderate kinematic velocities. This case is treated as central case for additional analysis and transport calculations.

4.4.1 Variable density and flow calculations

Salinity distribution

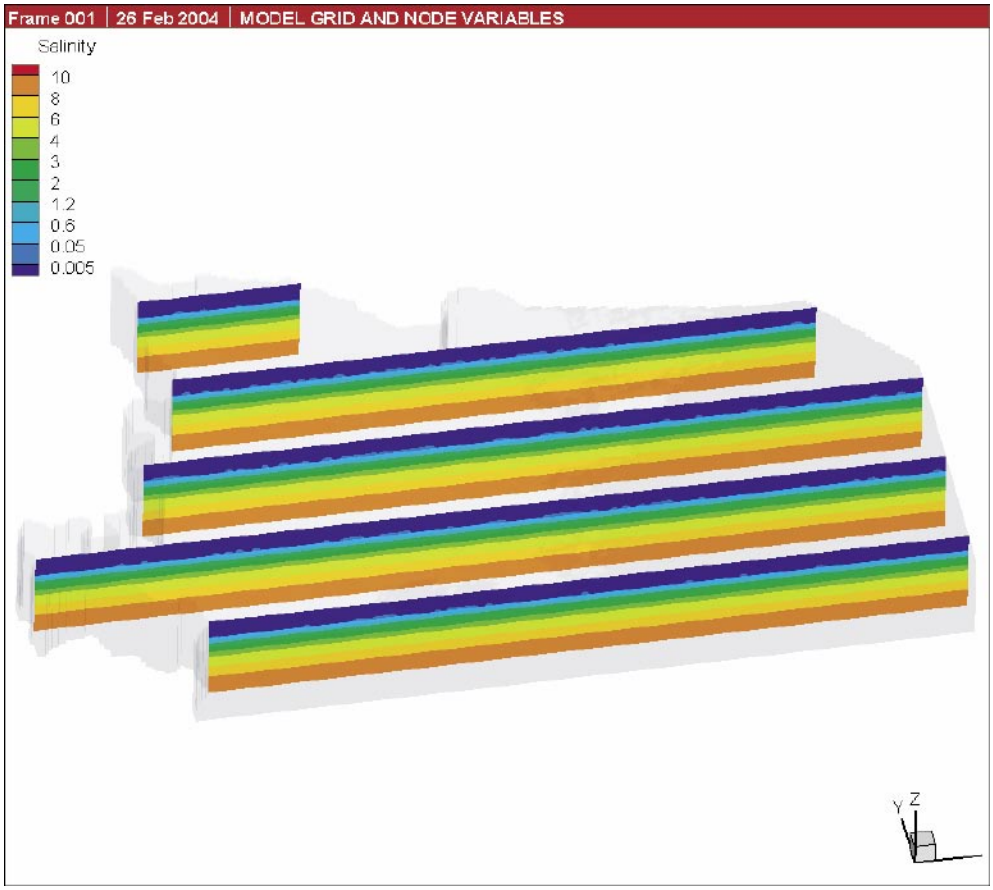

a)

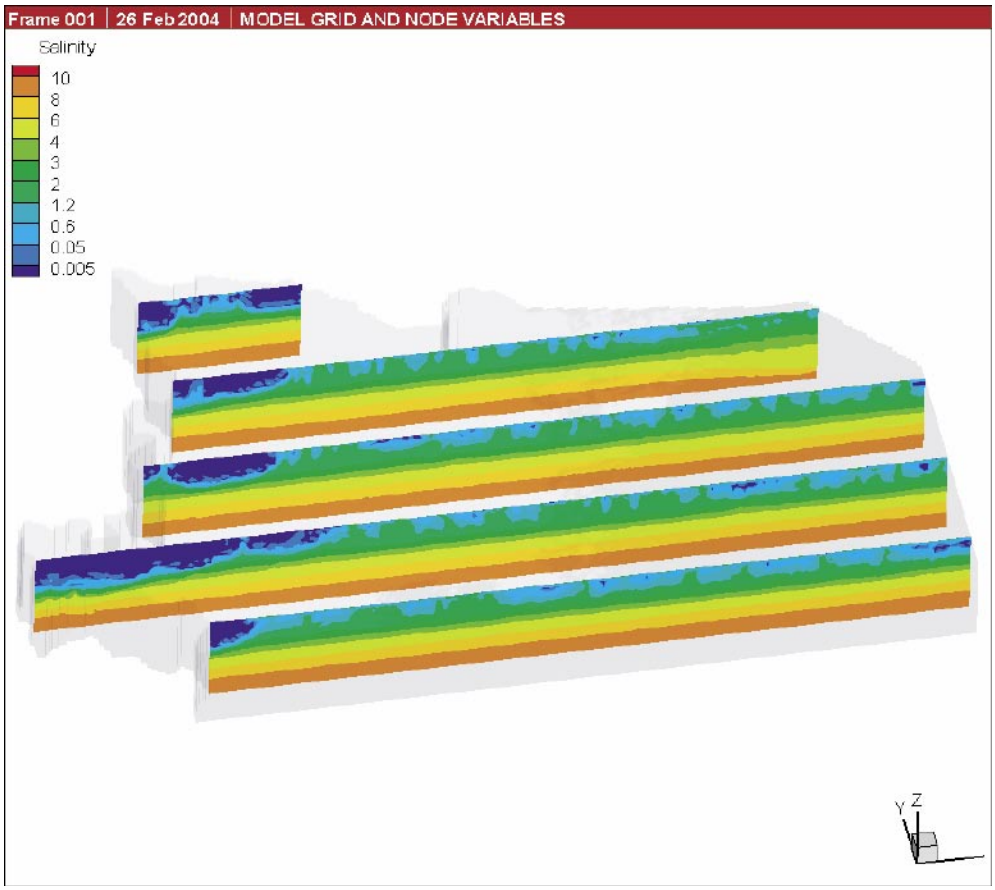

b)

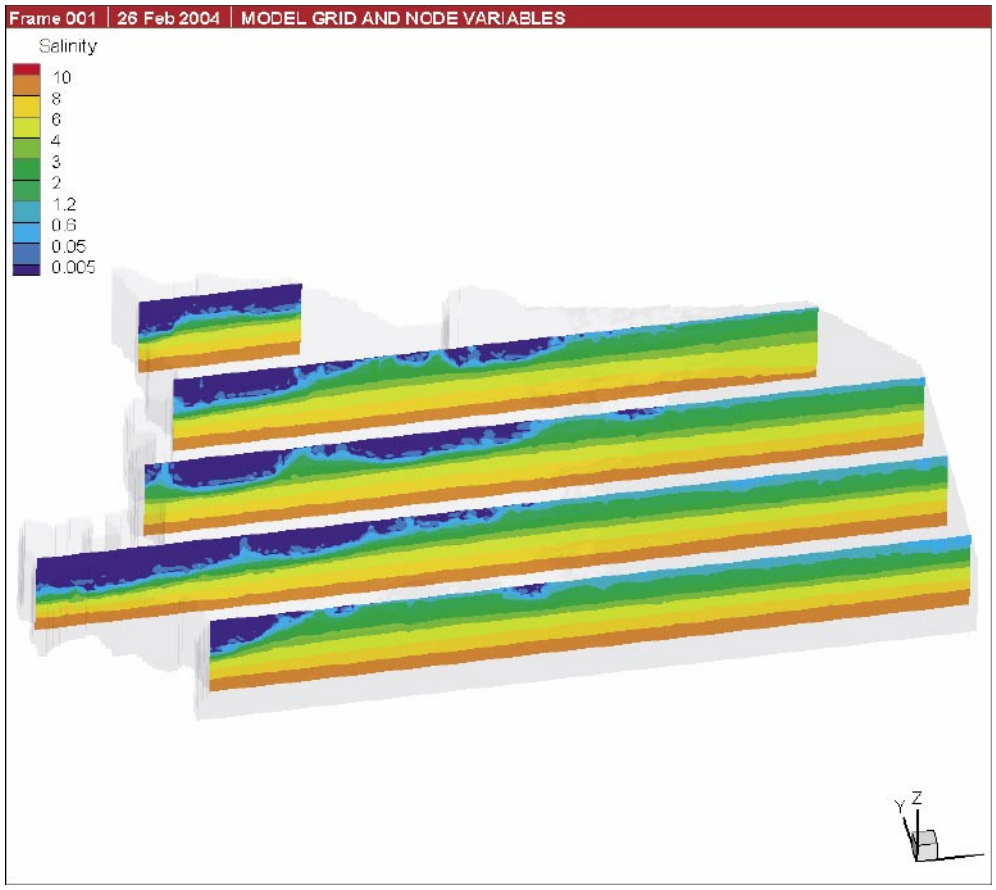

c)

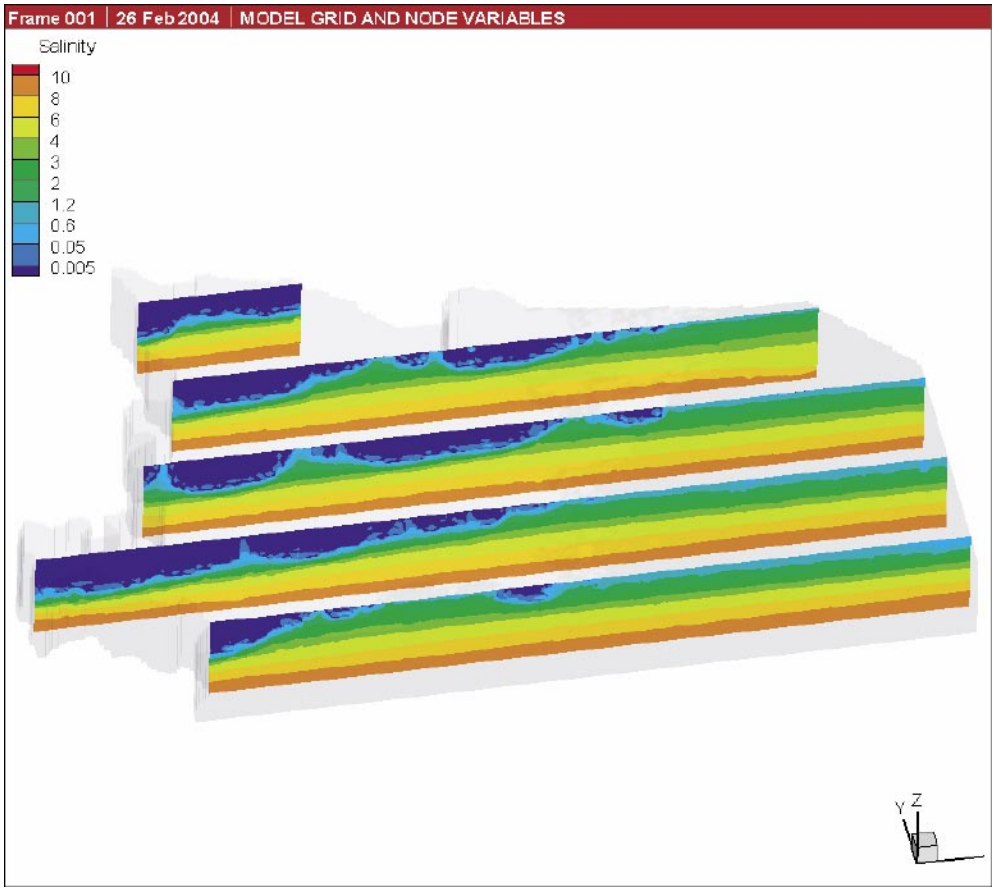

d)

Figure 4-6. *Salinity distribution in vertical slices for Case 3: pom11_1v4. a) 10,000 BC, b) 5000 BC, 0 BC, 2000 AD.*

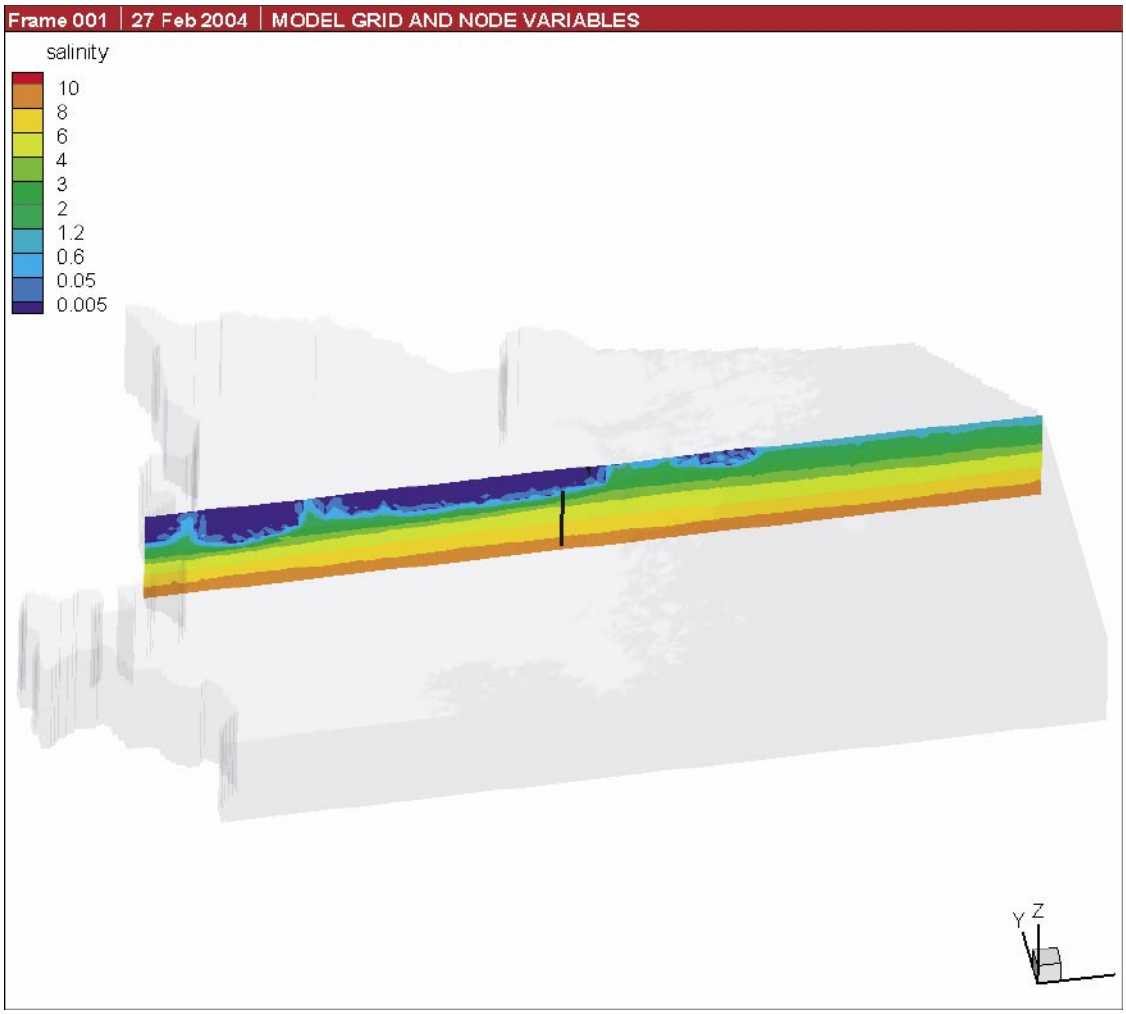

Figure 4-7. *Salinity profile in a slice through KLX01 at present time.*

Figure 4-6 shows the evolution in salinity for Case 3. As might be expected the behaviour is someway between cases 1 and 2. For the present day there is little flushing of the deep brine as for Case 2. Figure 4-7 shows a W-E slice through KLX01 for the present day illustrating how the top part of the rock around KLX01 has been completely swept of salinity, while the salinity is much shallower to the east around the island of Äspö. The evolution of salinity in close proximity to KLX01 is shown on a E-W slice in Figure 4-8 and on a S-N slice in Figure 4-9. The upcone of salinity in the East is toward the Äspö island and in the North toward an sea inlet.

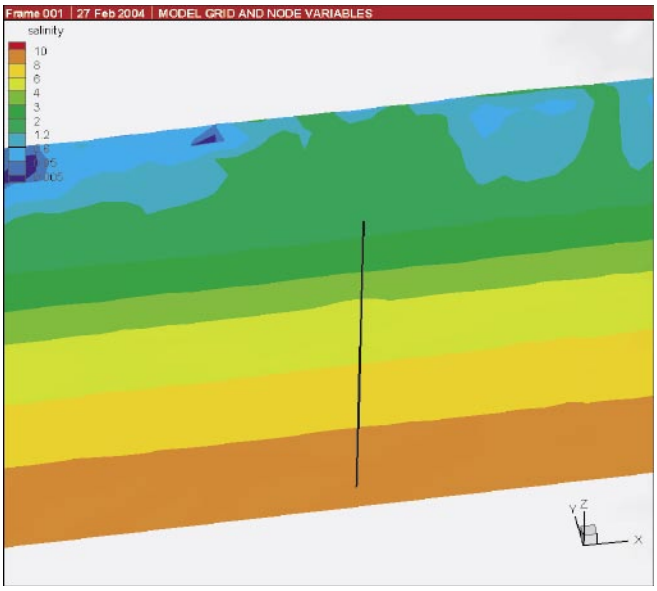

a)

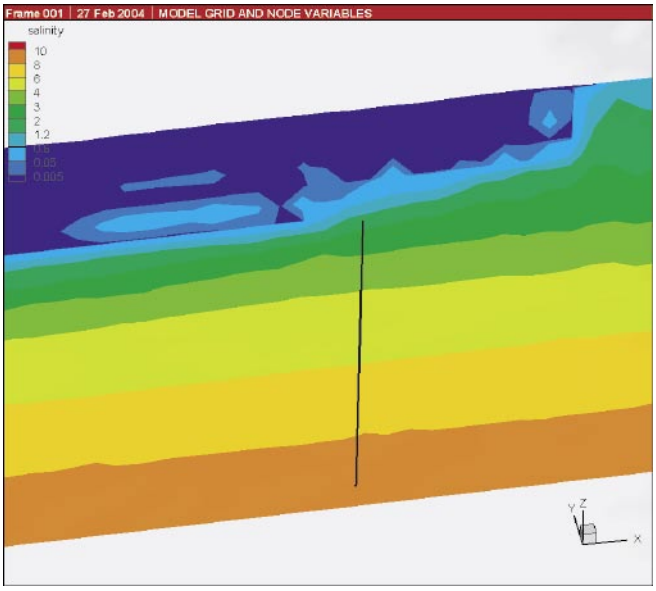

b)

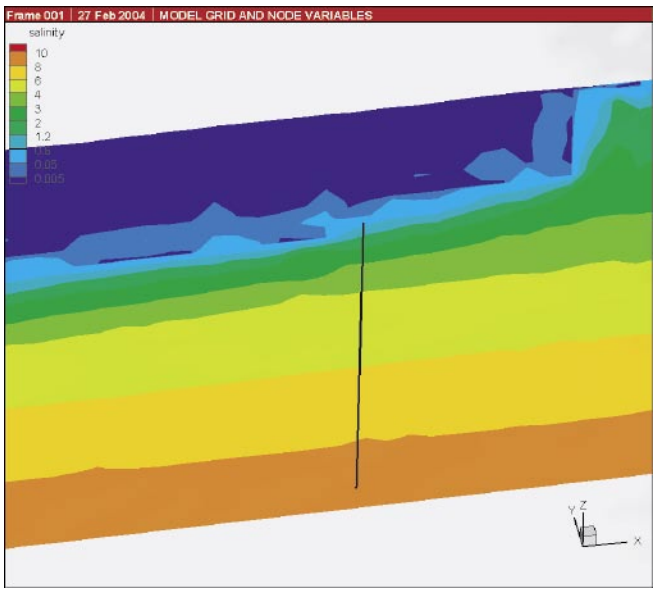

c)

Figure 4-8. *Salinity profile in a East-West slice at the vicinity of KLX01 for a) 5000 BC, b) 0 BC and c) 2000 AD in Case 3.*

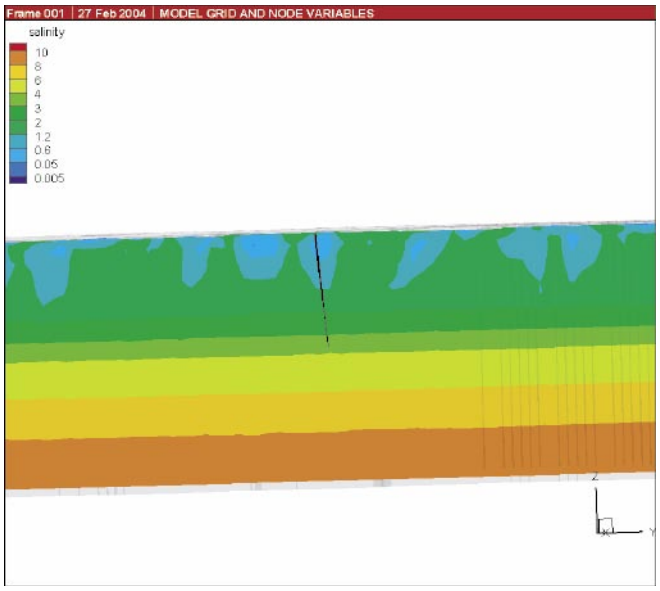

a)

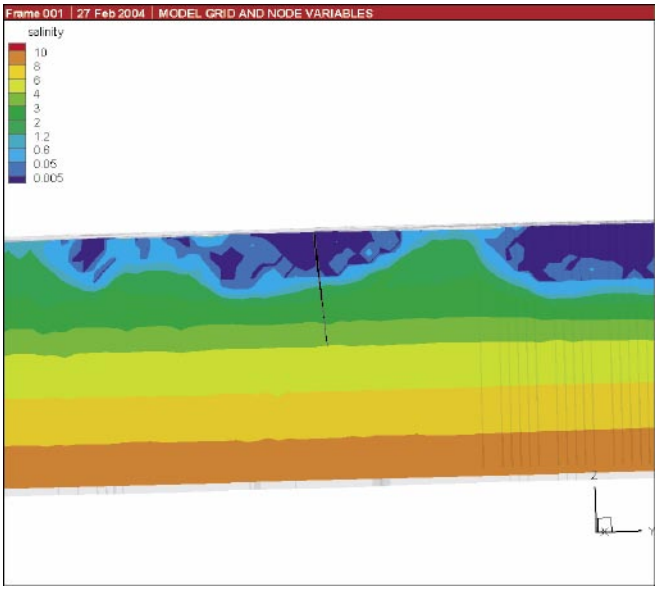

b)

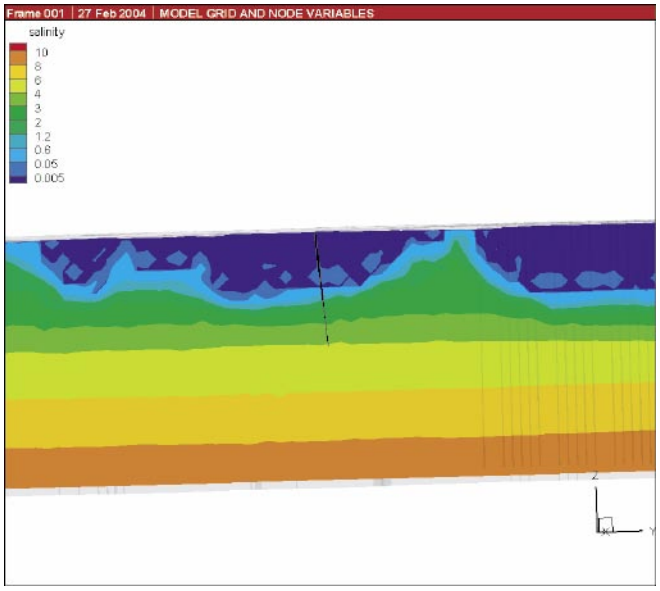

c)

Figure 4-9. *Salinity profile in a South-North slice at the vicinity of KLX01 for a) 5000 BC, b) 0 BC and c) 2000 AD in Case 3.*

The evolution in salinity profiles for KLX01 and KLX02 for Case 3 is shown in Figure 4-10. In similarity to Case 2, the salinity below about –900 masl is close to that of the initial guess, suggesting a stable area of low flow below this depth due to the brine above about 3% TDS.

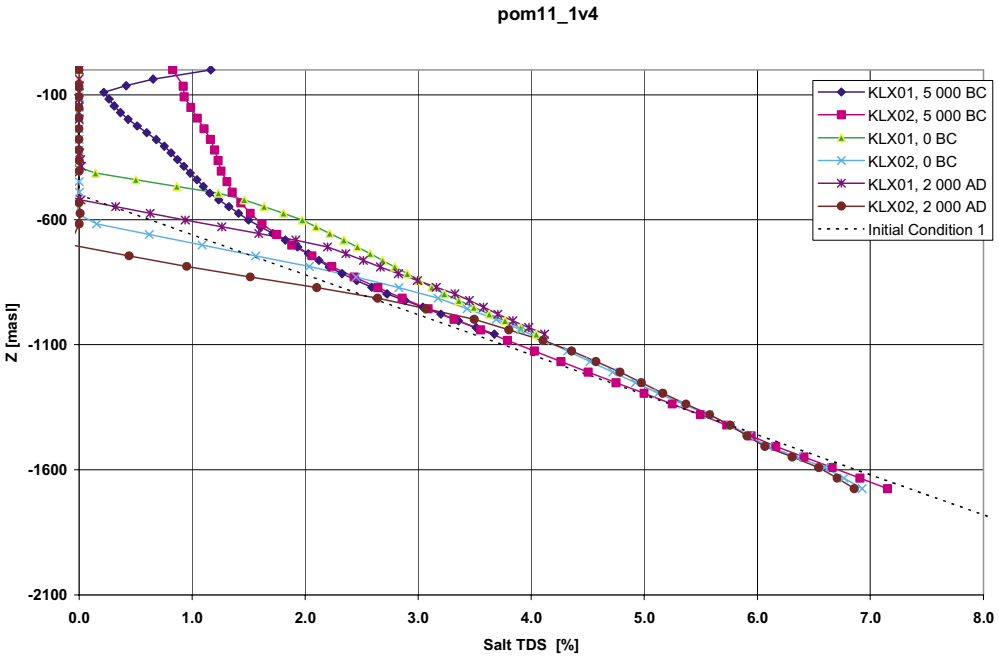

Figure 4-10. *Salinity profiles for different snapshots in time for the boreholes KLX01 and KLX02 in Case 3.*

Flow distribution

Contours of the vertical Darcy velocity under present day flow conditions are shown in Figure 4-11 on several horizontal sections at different depths. Near the surface at –10 masl and –100 masl flows are mainly downwards (recharge) around –0.001 to –0.01 m/year in the rock mass. Discharge areas are to the east (positive values of w) associated with the Baltic Sea and a few onshore discharge areas mainly located around fracture zones. Discharge rates in the fracture zones are 0.01 to 0.1 m/year in some areas. In the deeper rock, for example at repository depth of –500 masl, the flow rates are generally less than 0.001 m/year, although some higher upward flows rates in some fracture zones. The area of recharge on this section is much further inshore compared to the section at –100 masl. Clearly at this depth freshwater only penetrates to –500 masl below the higher topography and is then pushed up and over the dense brine for the remaining majority of the model area. At –1000 masl flow rates are very low in magnitude (perhaps lower contour values would show this better).

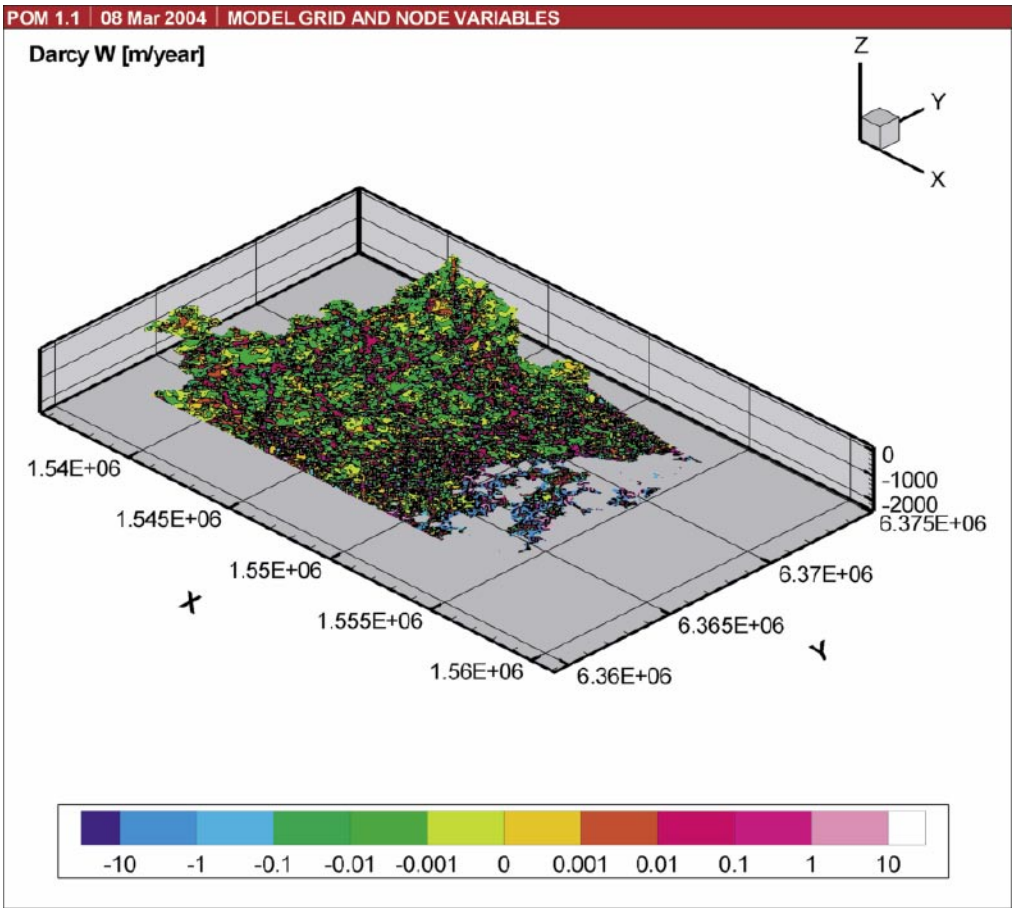
POM 1.1 | 08 Mar 2004 | MODEL GRID AND NODE VARIABLES
Darcy W [m/year]
Z
Y
X
0
-1000
-2000
6.375E+06
1.54E+06
1.545E+06
1.55E+06
1.555E+06
1.56E+06
6.37E+06
6.365E+06
6.36E+06
X
Y
-10
-1
-0.1
-0.01
-0.001
0
0.001
0.01
0.1
1
10

a)

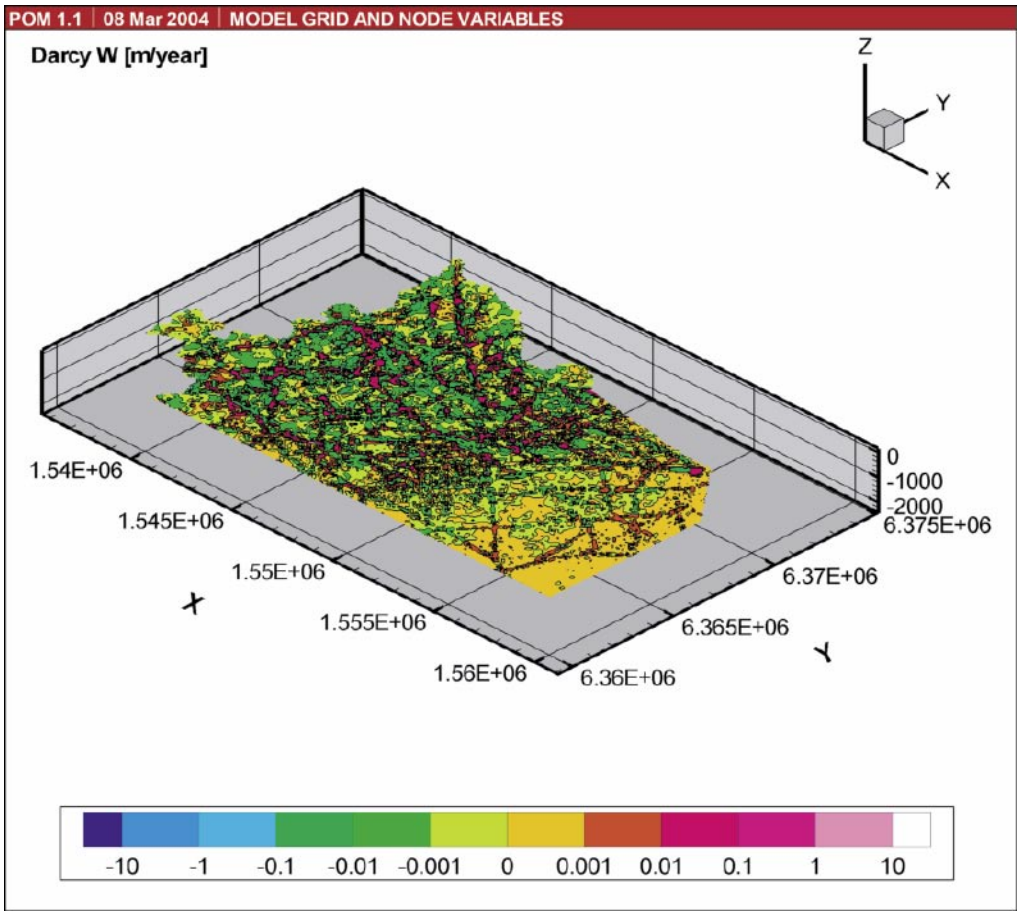
POM 1.1 | 08 Mar 2004 | MODEL GRID AND NODE VARIABLES
Darcy W [m/year]
Z
Y
X
0
-1000
-2000
6.375E+06
1.54E+06
1.545E+06
1.55E+06
1.555E+06
1.56E+06
6.37E+06
6.365E+06
6.36E+06
X
Y
-10
-1
-0.1
-0.01
-0.001
0
0.001
0.01
0.1
1
10

b)

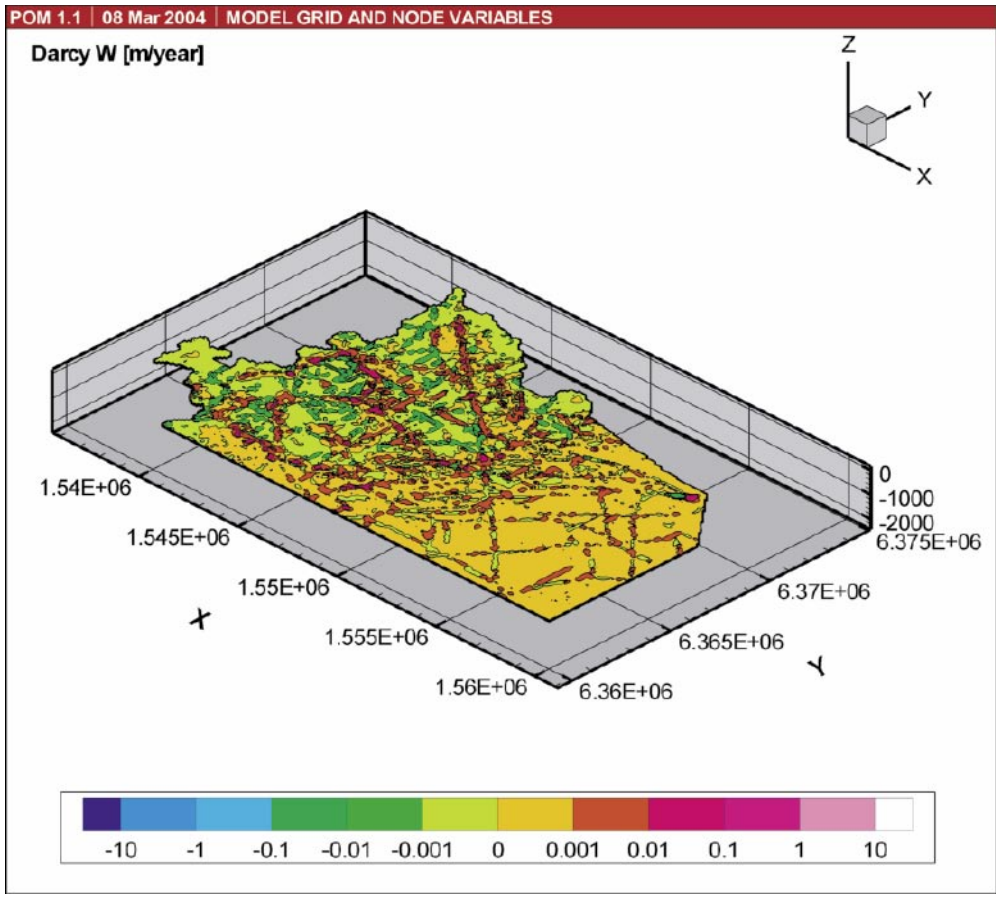

c)

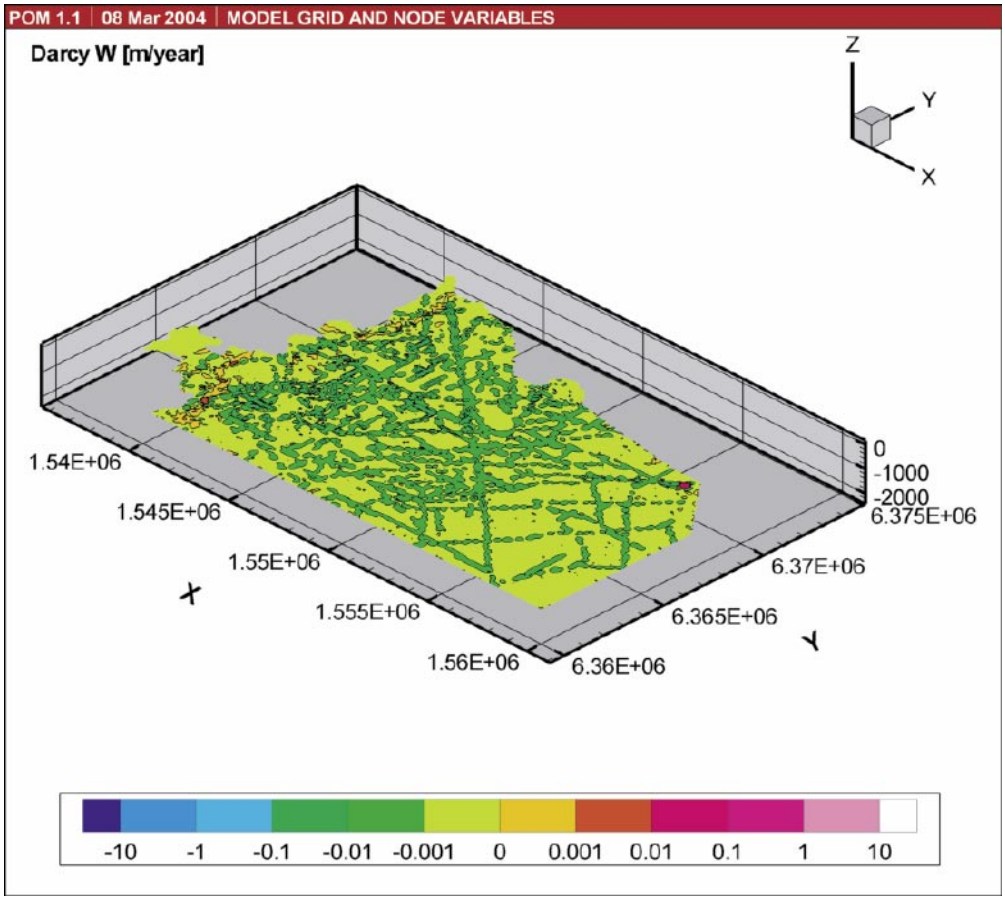

d)

Figure 4-11. *Contours of vertical Darcy velocity at present day at various depths. a) Z = –10 masl, b) Z = –100 masl, c) Z = –500 masl, Z = –1000 masl.*

4.5 Case 4, pom11_1v5

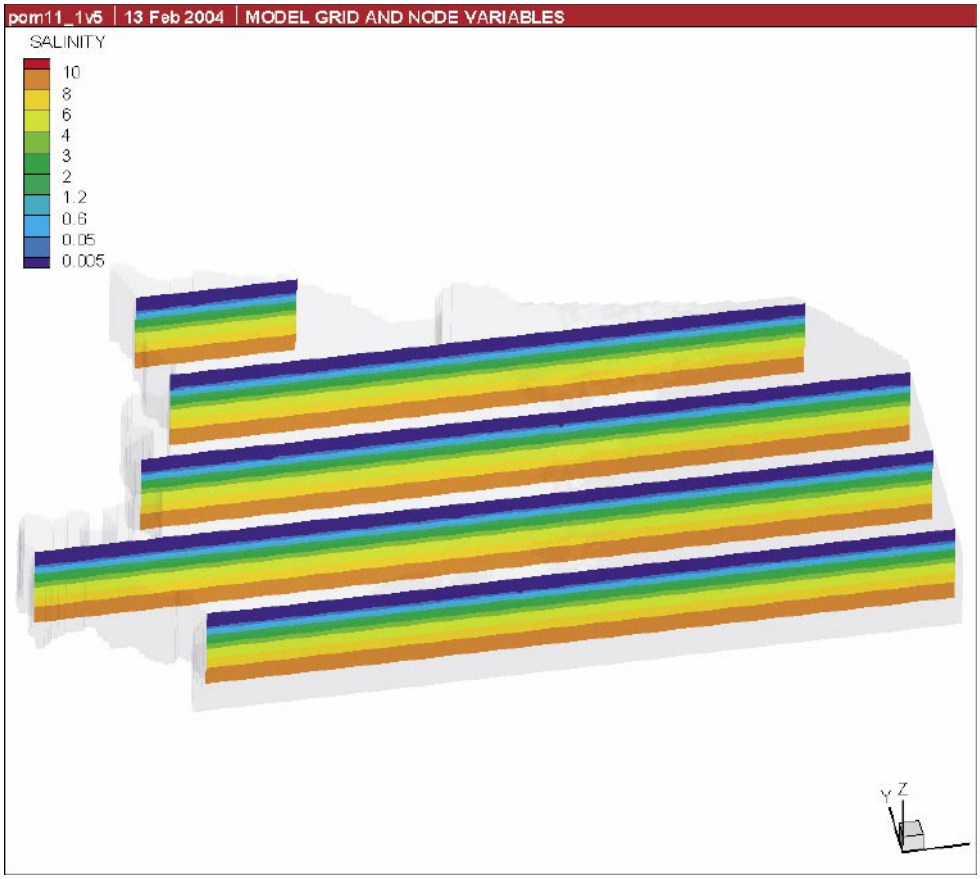

a)

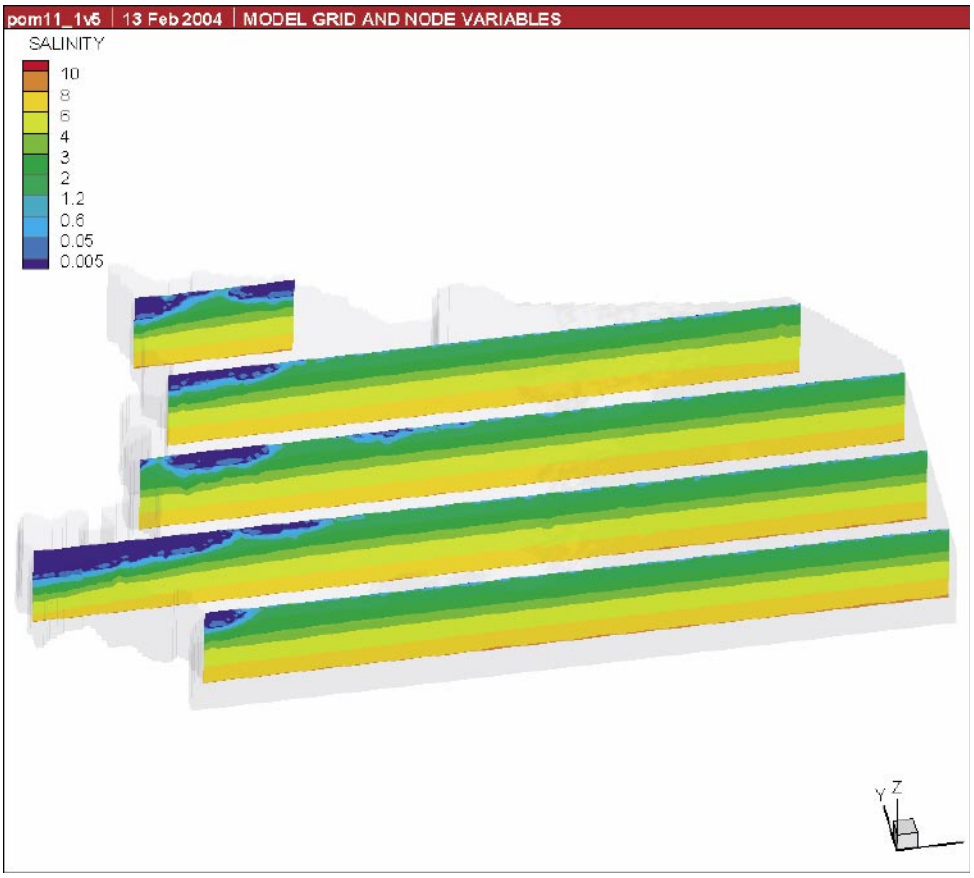

b)

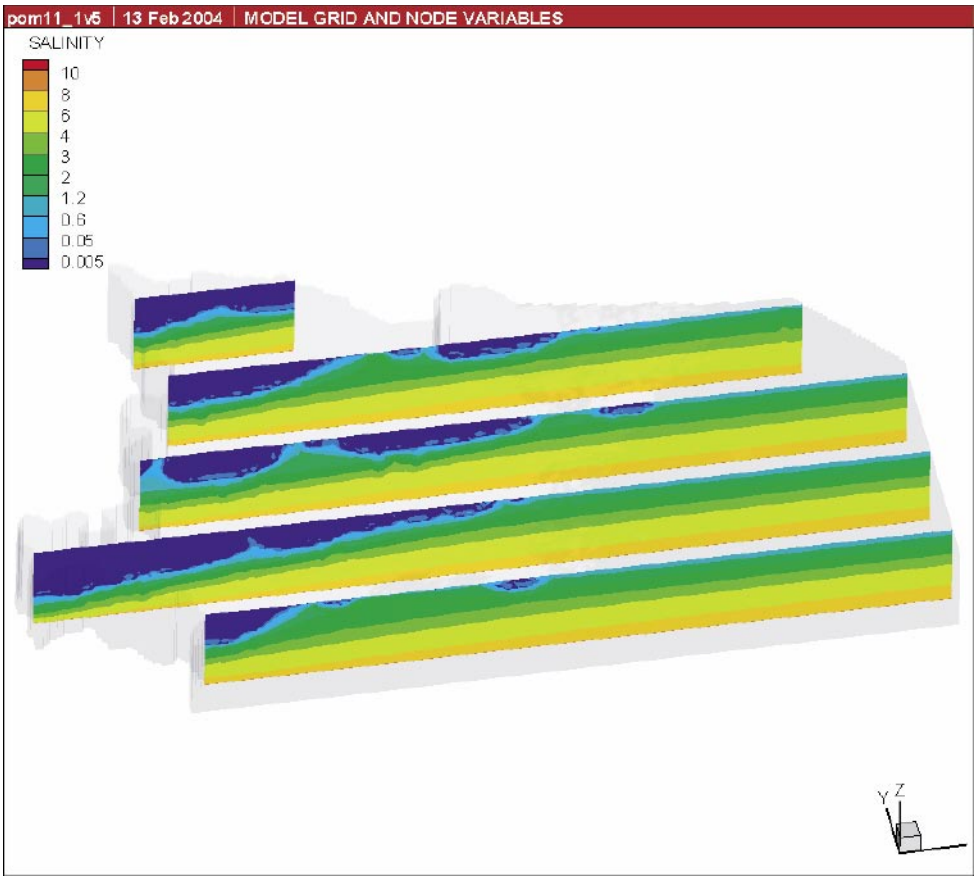

c)

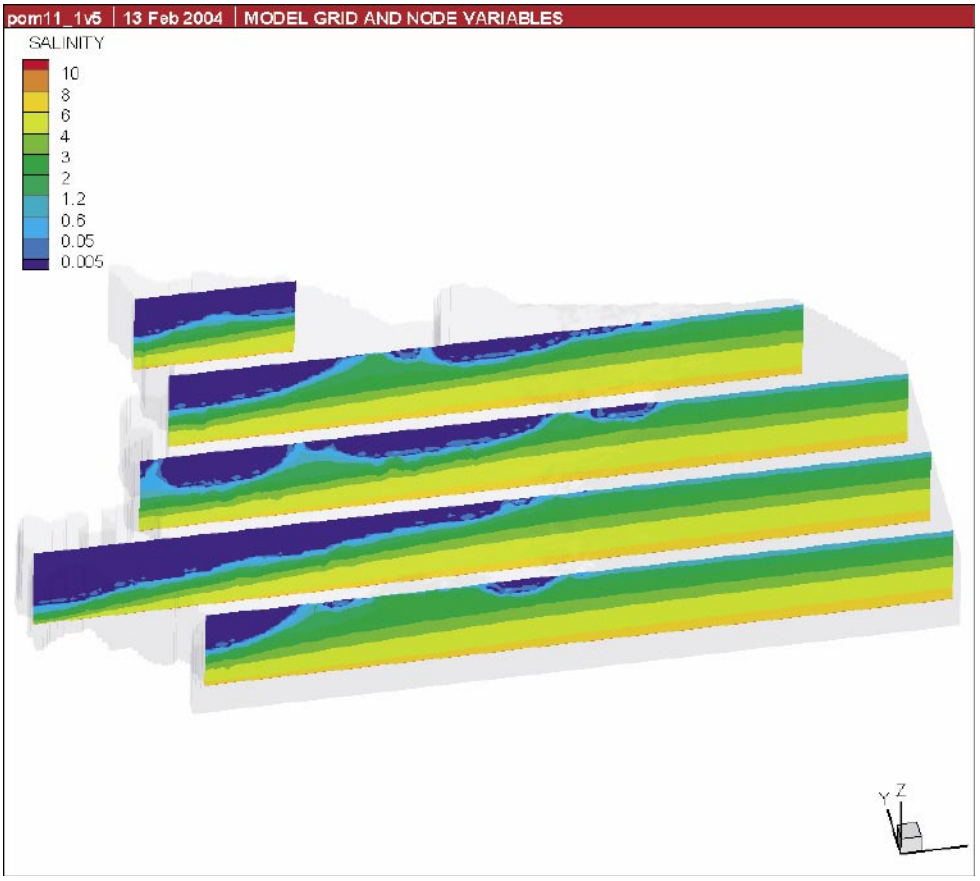

d)

Figure 4-12. *Salinity distribution in vertical slices for Case 4: pom11_1v5. a) 10,000 BC, b) 5000 BC, 0 BC, 2000 AD.*

Case 4 is based on Version 2 of the DFN model with a fracture-intensity 5 times higher, Initial condition1, and has an intermediate kinematic porosity of $2.0 \cdot 10^{-3}$ leading to the highest value of $K/\varphi = 1.2 \cdot 10^{-4}$, and hence high kinematic velocities. As discussed in Section 3.4, the average permeability for this case is about 20 times higher than for the Version 1 DFN model. This case is treated as an extreme or pessimistic case for additional analysis and transport calculations.

4.5.1 Variable density and flow calculations

Salinity distribution

Figure 4-12 shows the evolution in salinity for Case 4. The most notable feature here is the reduced salinity at depth suggesting much enhanced flushing of salinity due the higher flow. This is entirely physically possible, but there may be other numerical factors that lead to enhanced mixing. One possibility is that the 20 years time-step is too coarse a temporal discretisation for this case. Extra calculations based on Case 4, but with shorter time-steps were performed and are reported in Section 4.8. In fact, it was found that was less mixing for a smaller time–step.

Figure 4-13 shows the salinity profile in KLX01 and KLX02 for Case 4. This clearly shows the enhanced mixing of freshwater and brine at depth with a steep salinity profile that is below the initial condition.

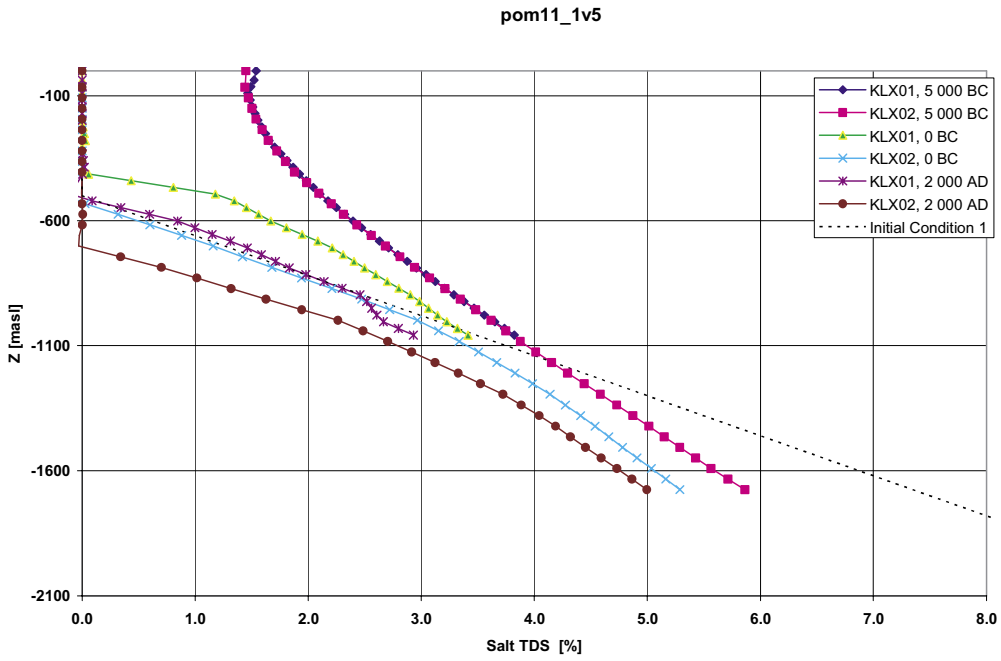

Figure 4-13. *Salinity profiles for different snapshots in time for the boreholes KLX01 and KLX02 in Case 4.*

4.6 Case 5, pom11_1v6

Case 5 is based on Version 3 of the DFN model with a fracture size going down to 50 m, Initial condition1, and has an intermediate kinematic porosity of $2.0 \cdot 10^{-3}$ leading to a moderate value of $K/\varphi = 5 \cdot 10^{-6}$, and hence moderate kinematic velocities. As discussed in section 3-4, the average permeability for this case is slightly higher than Version 1, and is more homogeneous.

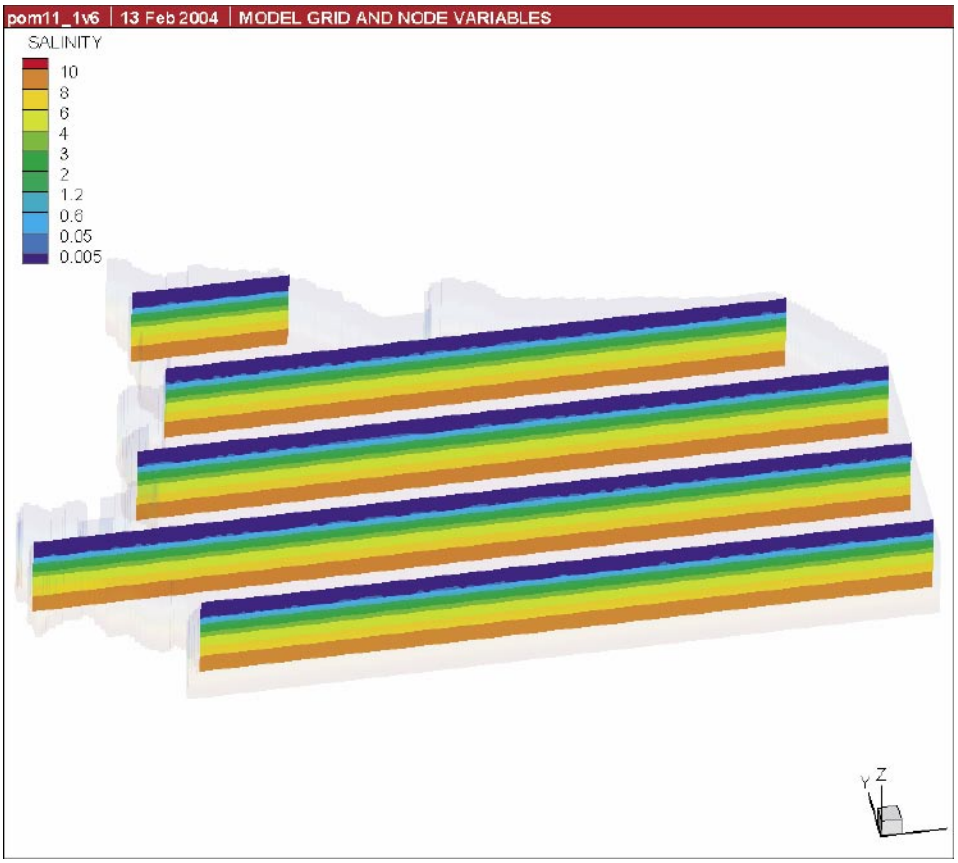
pom11_1v6 | 13 Feb 2004 | MODEL GRID AND NODE VARIABLES
SALINITY
10
8
6
4
3
2
1.2
0.8
0.05
0.005
Y Z

a)

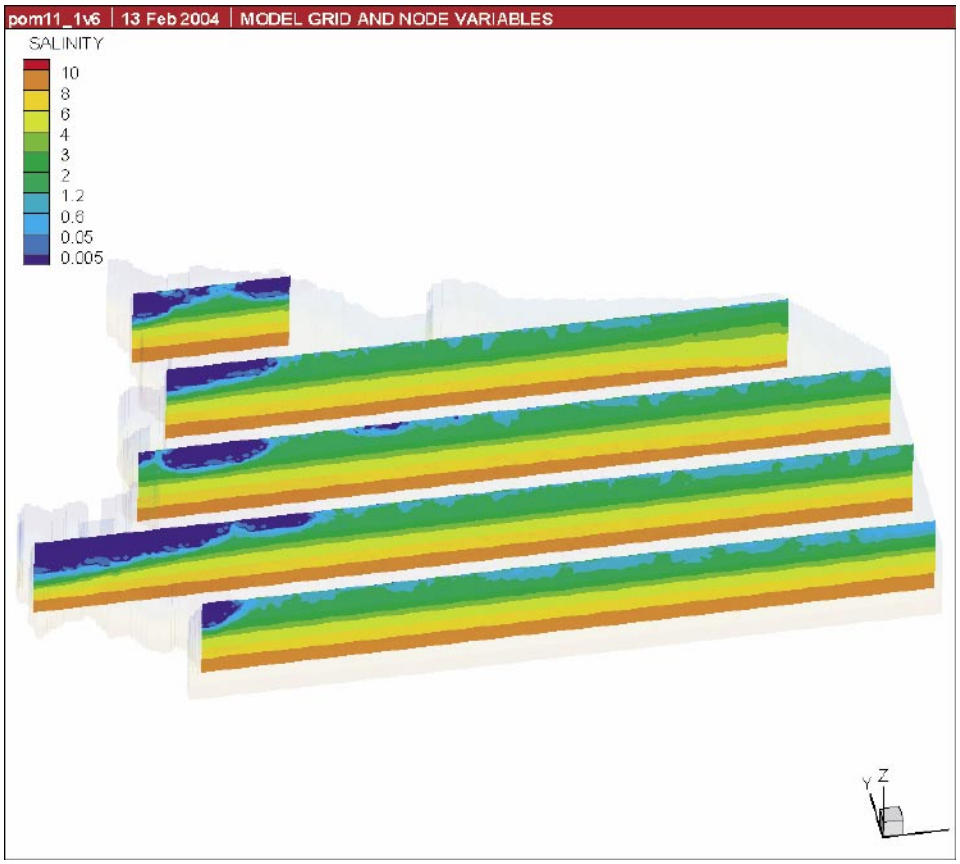
pom11_1v6 | 13 Feb 2004 | MODEL GRID AND NODE VARIABLES
SALINITY
10
8
6
4
3
2
1.2
0.8
0.05
0.005
Y Z

b)

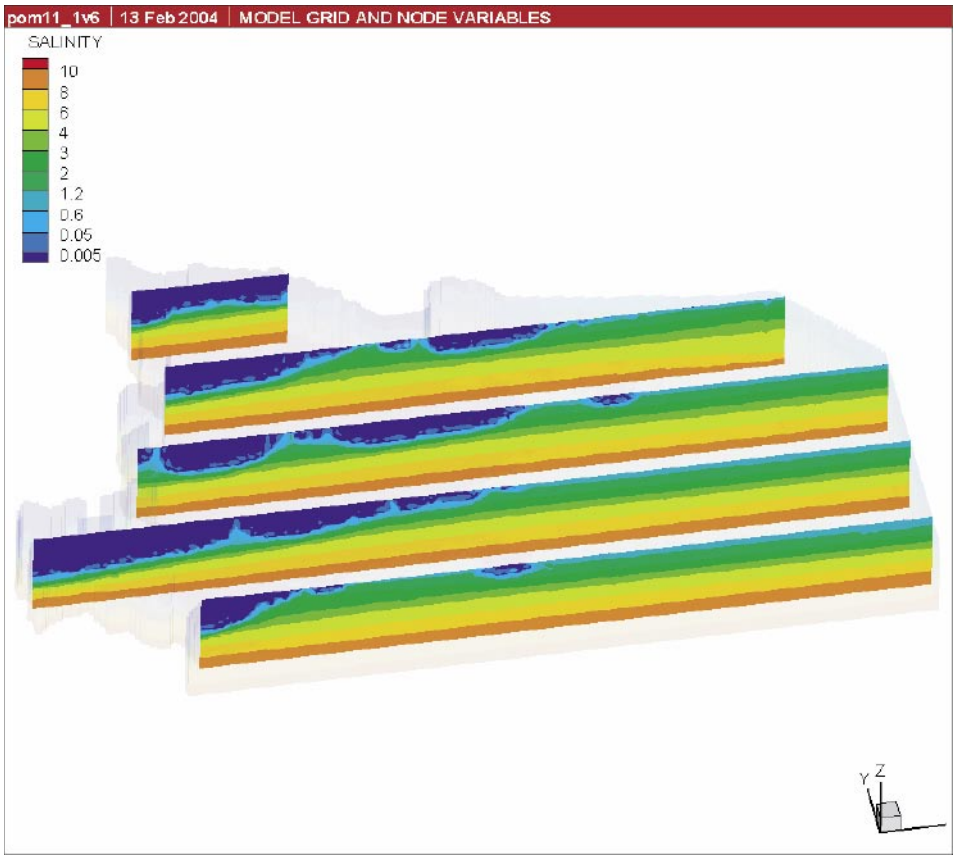

c)

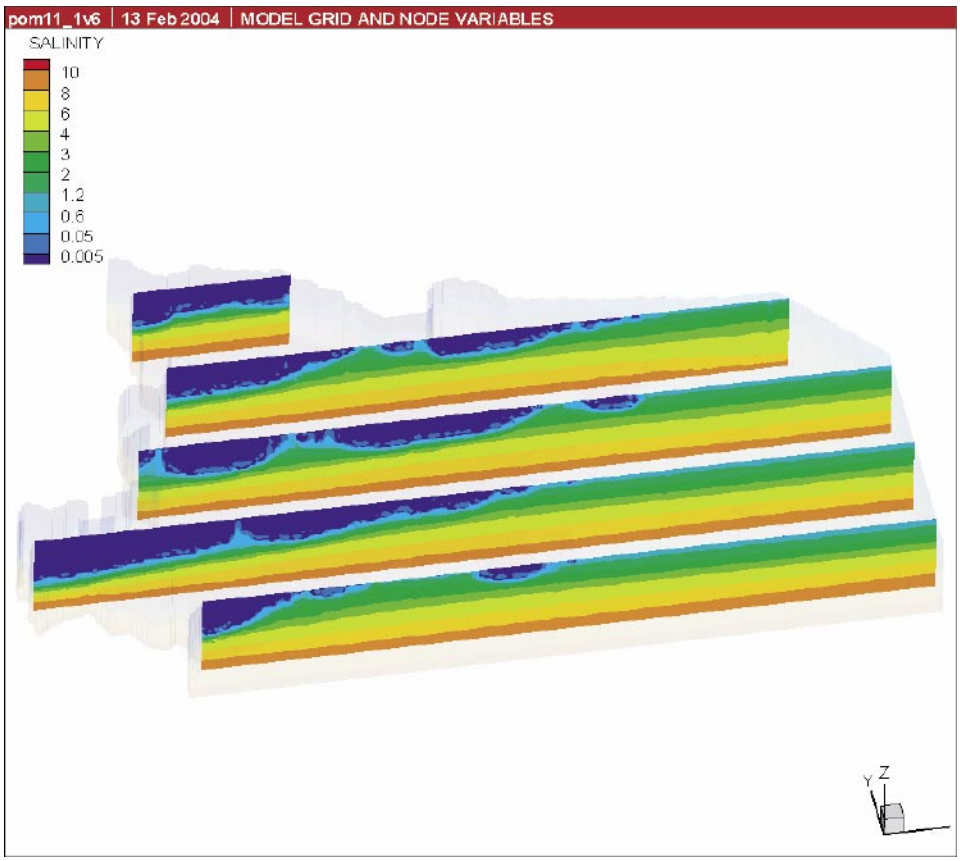

d)

Figure 4-14. *Salinity distribution in vertical slices for Case 5: pom11_1v6. a) 10,000 BC, b) 5000 BC, 0 BC, 2000 AD.*

4.6.1 Variable density and flow calculations

Salinity distribution

Figure 4-14 shows the evolution in salinity for Case 5. This case is very similar to Case 3 and demonstrates that using a cut-off in fracture length at 100 m is reasonable assumption for the particular DFN parameters used in Version 1 and for a element size of 100 m. This may not be the case for different DFN parameterizations such as at Forsmark where the exponent for the Power-law length distribution was higher, 2.97 rather than 2.6. A different correlation between fracture transmissivity and length would also require the issue of cutting-off the DFN distributions to be revisited. The salinity profiles in KLX01 and KLX02 for Case 5 are shown in Figure 4-15. Again, the profiles are much like Case 3.

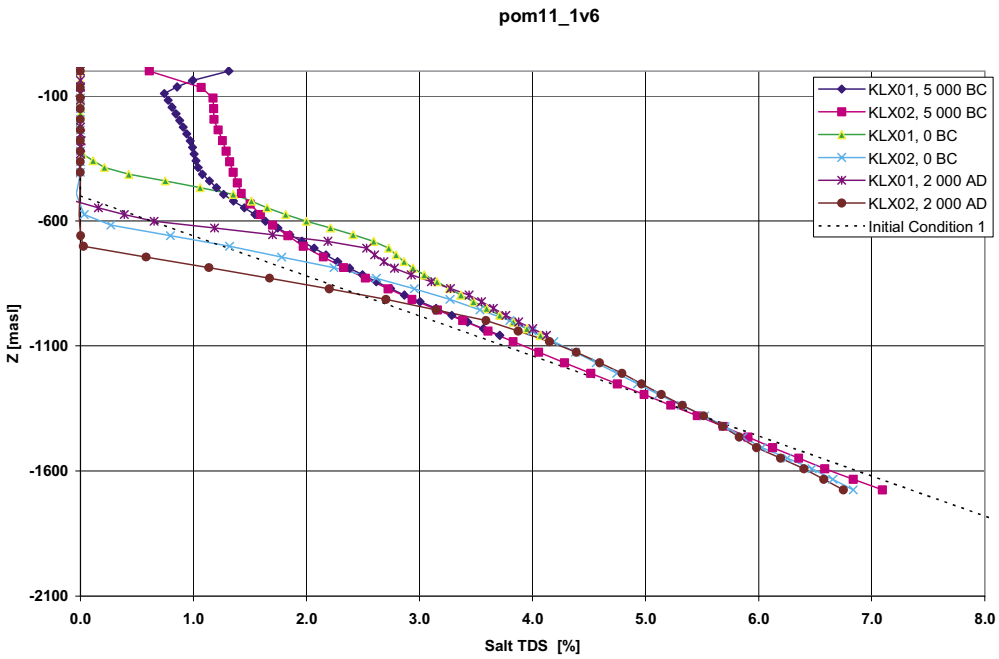

Figure 4-15. *Salinity profiles for different snapshots in time for the boreholes KLX01 and KLX02 in Case 5.*

4.7 Case 6, pom11_1v7

Case 6 is based on Version 1 of the DFN model, Initial condition 2, and has an intermediate kinematic porosity of $2.0 \cdot 10^{-3}$ leading to a moderate value of $K/\varphi = 4 \cdot 10^{-6}$, and hence moderate kinematic velocities. The purpose of this case is to check the sensitivity to the initial condition. Since the initial condition is uncertain, it is important to see if by starting at a time sufficiently far in the past, then the sensitivity to the initial condition can be minimised. In this case, the initial condition has brine starting much deeper, at -1000 masl rather than –500 masl. This means that to obtain the same salinity profile as for Initial condition 1, then the salinity associated with the Litorina pulse around 7000 years ago would have sink down to the deep rock to make up the difference between the two initial conditions. This process will require that the Litorina period is sufficiently saline and lasted long enough for a sufficient flux of salinity to enter the subsurface. Thus, several parameters and boundary conditions will affect this concept. Here, we just consider a single variant to see if the top surface salinity boundary condition, described in Figure 3-18, can compensate for a different initial saline condition.

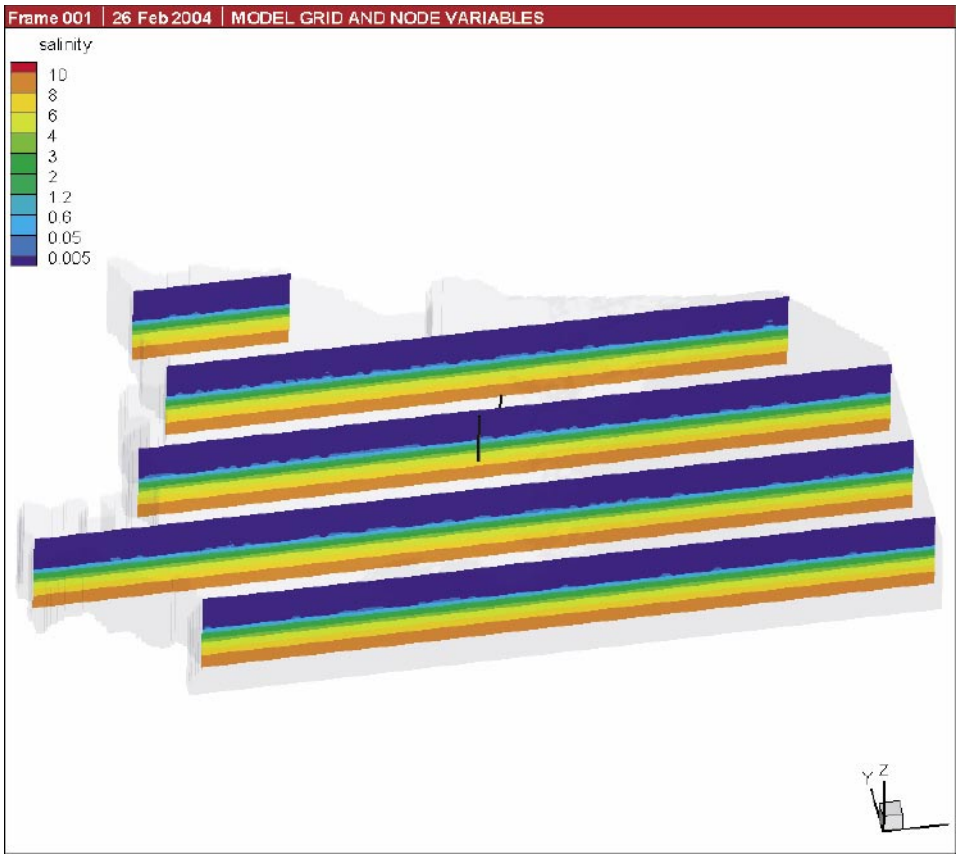
Frame 001 | 26 Feb 2004 | MODEL GRID AND NODE VARIABLES
salinity
10
8
6
4
3
2
1.2
0.6
0.05
0.005
Y Z

a)

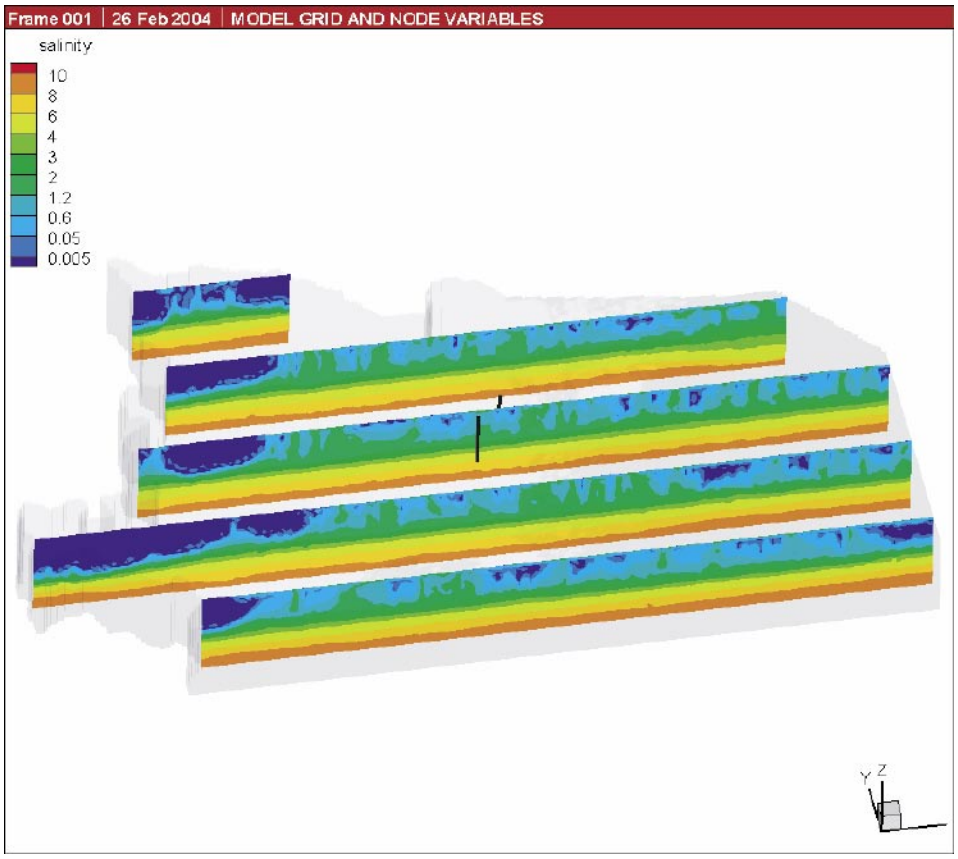
Frame 001 | 26 Feb 2004 | MODEL GRID AND NODE VARIABLES
salinity
10
8
6
4
3
2
1.2
0.6
0.05
0.005
Y Z

b)

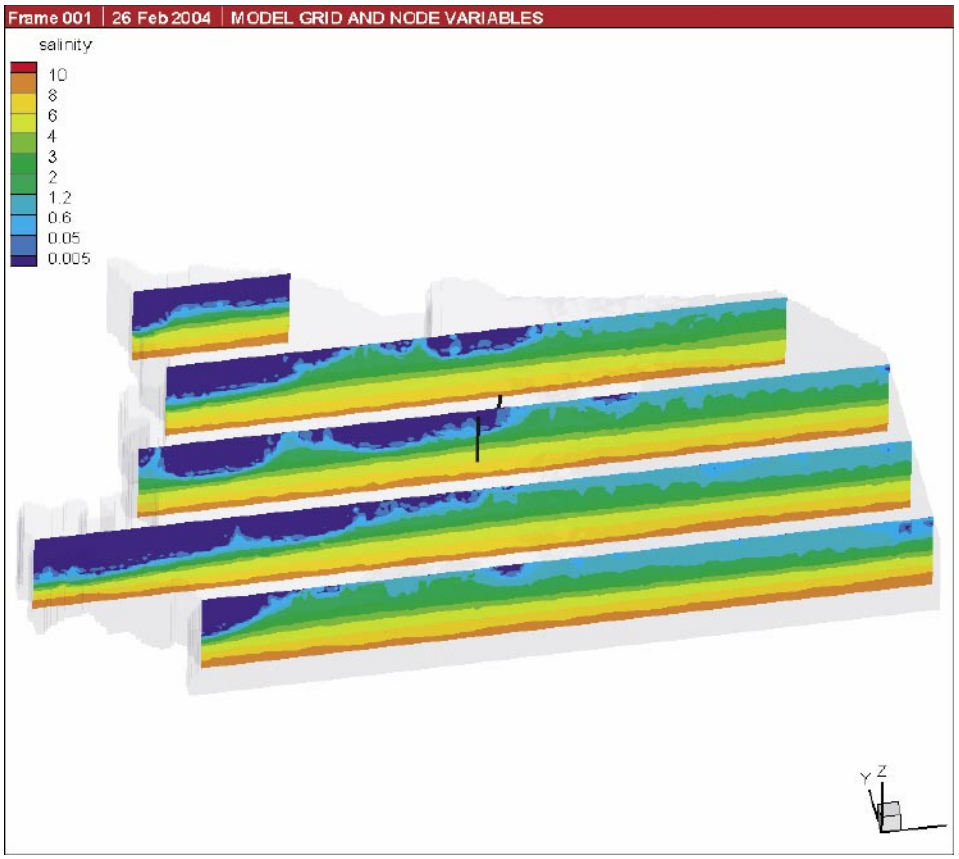

c)

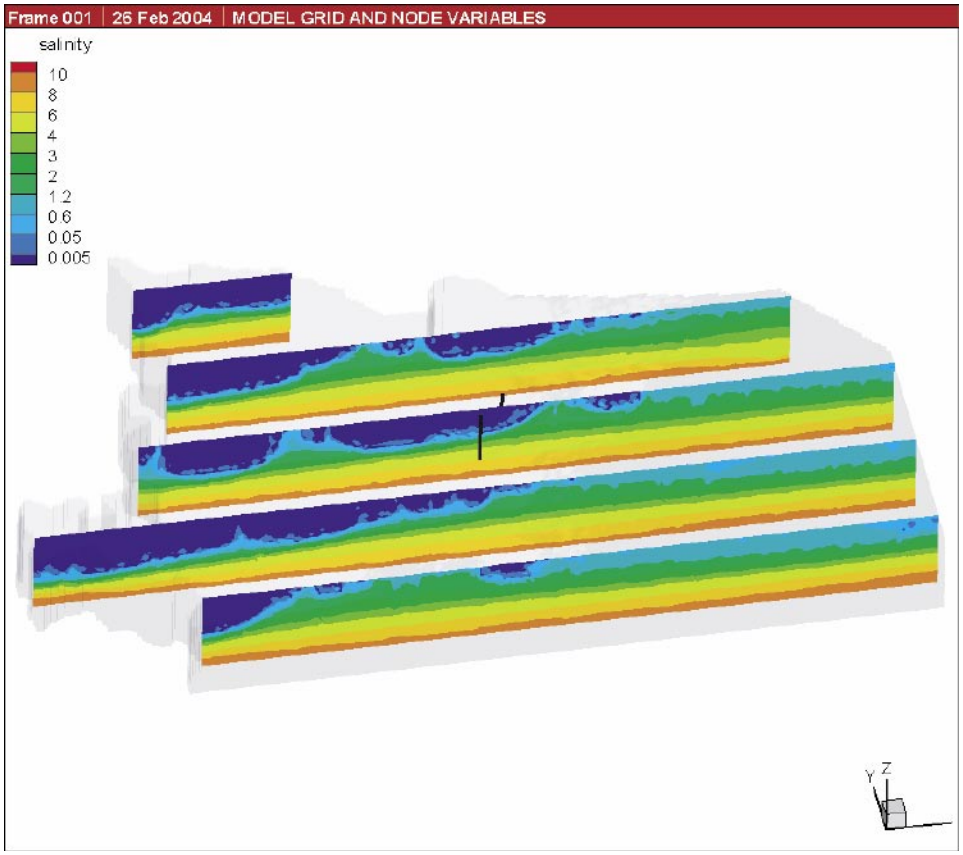

d)

Figure 4-16. *Salinity distribution in vertical slices for Case 6: pom11_1v7. a) 10,000 BC, b) 5000 BC, 0 BC, 2000 AD.*

4.7.1 Variable density and flow calculations

Salinity distribution

Figure 4-16 shows the evolution in salinity for Case 6. The deeper initial salinity profile can be seen at -10,000 BC. At 5000 BC there is infiltration of the Litorina Sea over much of the domain, except in the West. By the present day some of this Litorina pulse has been flushed out. It also clear that the salinity from the top surface boundary condition is weaker than that of the deep brine at the base of the model, so there is no possibility that the Litorina pulse could completely make up for the difference in initial conditions. Figure 4-17 shows the salinity profiles in KLX01 and KLX02. What is interesting here is that in KLX02, the salinity has increases at depth between 5000 BC and 0 AD as the Litorina pulse sinks down. However, at –1500 masl the salinity is unchanged from the initial condition at around 5% TDS. This would suggest that the Litorina Sea concentration would have to be higher to, around 10% to completely make up for the difference in initial condition.

These results would suggest that a set of saline boundary conditions could be chosen to reduce the sensitive to the boundary conditions with the key parameters being the maximum salinities of the initial condition and the Baltic Sea.

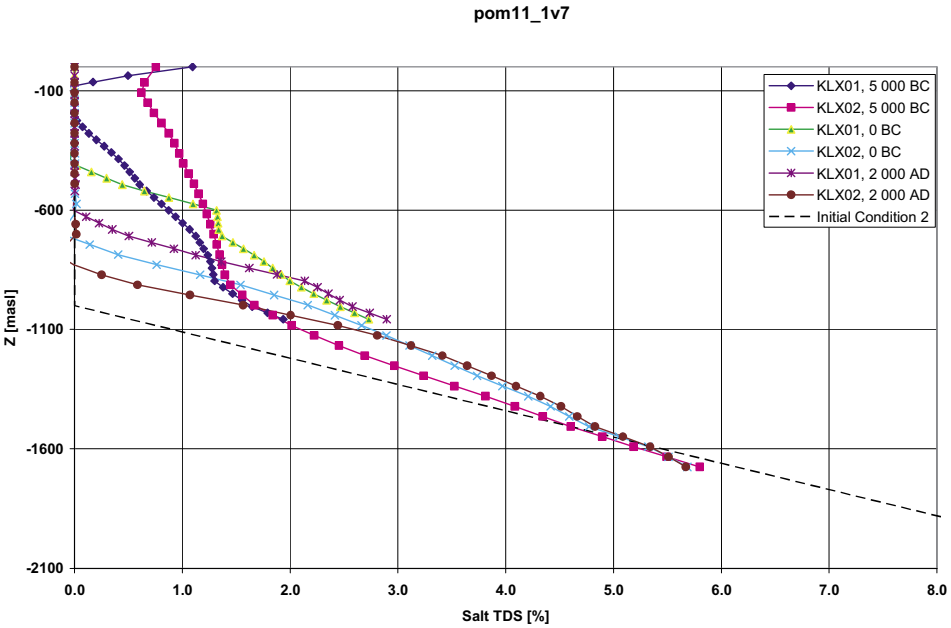

Figure 4-17. *Salinity profiles for different snapshots in time for the boreholes KLX01 and KLX02 in Case 6.*

4.8 Temporal discretisation

Two extra cases, 7 and 8, were performed to check the sensitivity to the choice of time-step. In the Forsmark modelling 20 years had been found to be an appropriate time-step, but in cases such as Case 4 the permeability is much higher so smaller time-step may be required. Taking Case 4 as the extreme case with the highest value of K/φ, two runs were performed with time-steps of 10 years and 5 years.

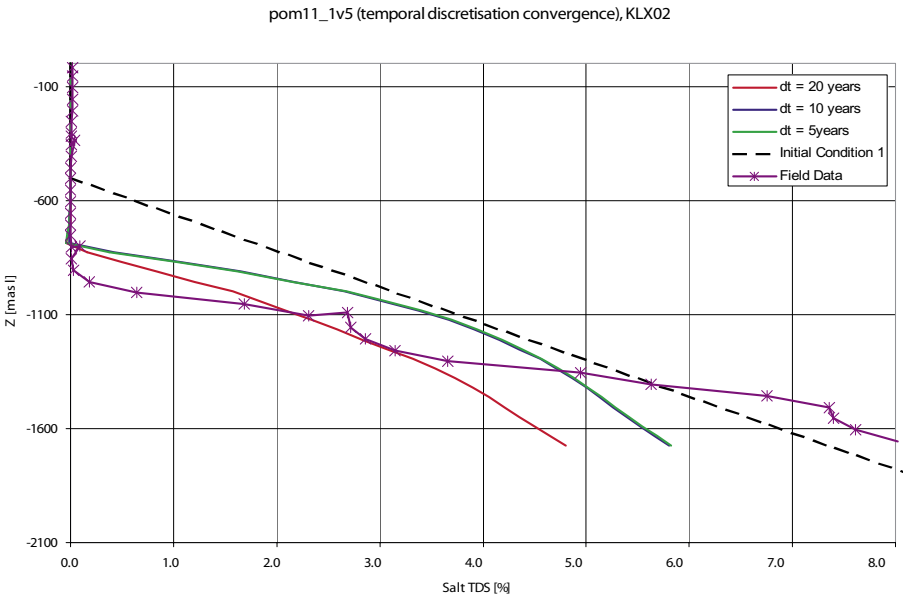

Figure 4-18. *Salinity profiles for different time-steps sizes for Case 4 and for KLX02. The field measurements are also shown.*

Figure 4-18 shows a comparison of the salinity profiles in KLX02 (the deeper borehole) for a time-step of 20 years (Case 4), 10 years (Case 7) and 5 years (Case 8). The profiles for 5 and 10 years almost overlay each other, suggesting that the results are converged with respect to time-step at 10 years. For these shorter time-steps, the salinity is higher and nearer to the initial condition around –1000 masl, but there is still a steeper gradient at greater depths. This would imply that for higher values of K/φ there is physically more mixing of water at large depths due to the higher kinematic velocities.

4.9 Transport calculations

In addition to understanding the salinity and flow conditions at the site, standard safety assessment performance measures were also requested. It should be noted that these results are only preliminary indications of what might be obtained, since extra spatial refinement would be required in the local-scale to obtain results appropriate for use in a safety assessment. For brevity, only two cases will be considered: Case 3 as a central case, and Case 4 as a pessimistic case. For a CPM model, the F-quotient is calculated as the integral of flow-wetted surface divided by Darcy velocity along a pathline.

4.9.1 Case 3

Figure 4-19 shows the set of start points (a regular grid of 861 points in each area with a 50 m spacing) for the two sites: Laxemar (north-west) and Simpevarp (south-east). The start points are coloured by Log (travel time) and the fracture zones are shown. This reveals some interesting results. Firstly, the fracture zones have a very big influence on travel time. Secondly, travel times are generally shorter in Laxemar than Simpevarp. Figure 4-20 shows an equivalent plot for the exit points. There are several short paths that travel almost vertically up some fracture zones, and many discharge points are close to the local-scale areas.

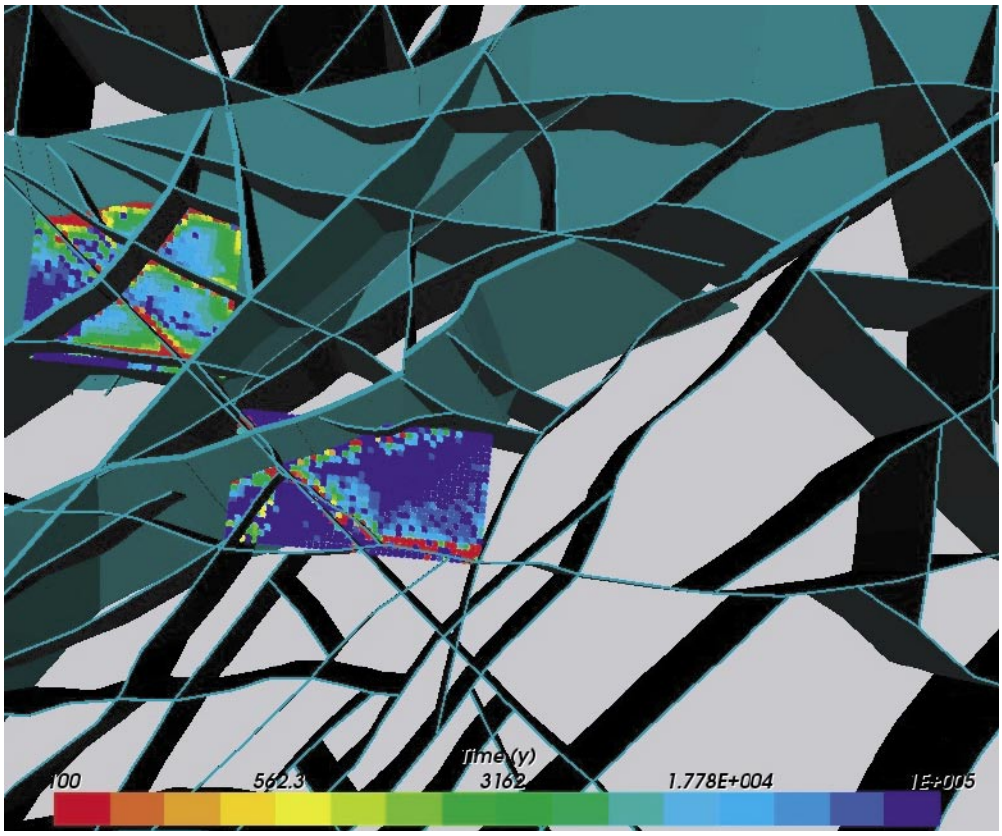

Figure 4-19. *Case 3, low K/φ – start points coloured by total travel time (Log-scale 100–10,000 years) and fracture zones.*

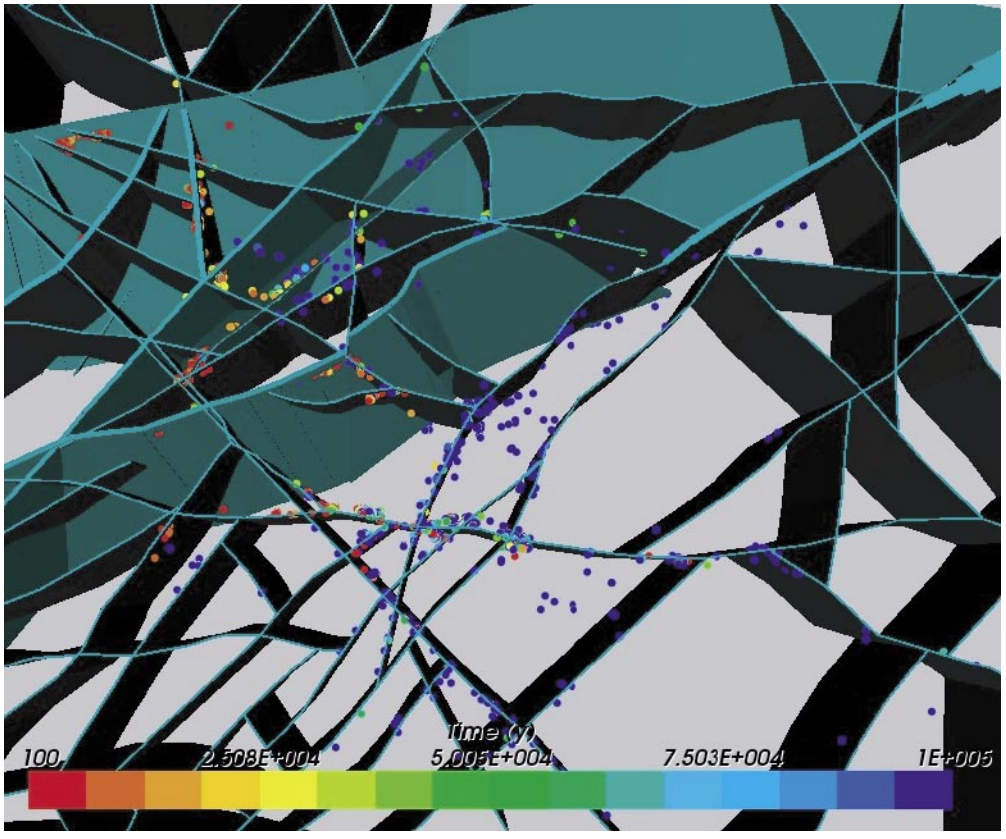

Figure 4-20. *Case 3, low K/φ – exit points coloured by total travel time (Log-scale 100–10,000 years) and fracture zones.*

The equivalent plots for F-quotient are shown in Figure 4-21 and Figure 4-22. Figure 4-23 shows the full pathlines colour by travel-time along the path. The reason for the difference smaller travel-times and F-quotients in the Laxemar area are partly due to more fractures zones, but also to the position of the saline transition zone. The start-points at Laxemar are essentially in freshwater, whereas at Simpevarp the area is the saline area. This is shown in Figure 4-24 by superimposing the start-points on two vertical slices coloured by contours of salinity.

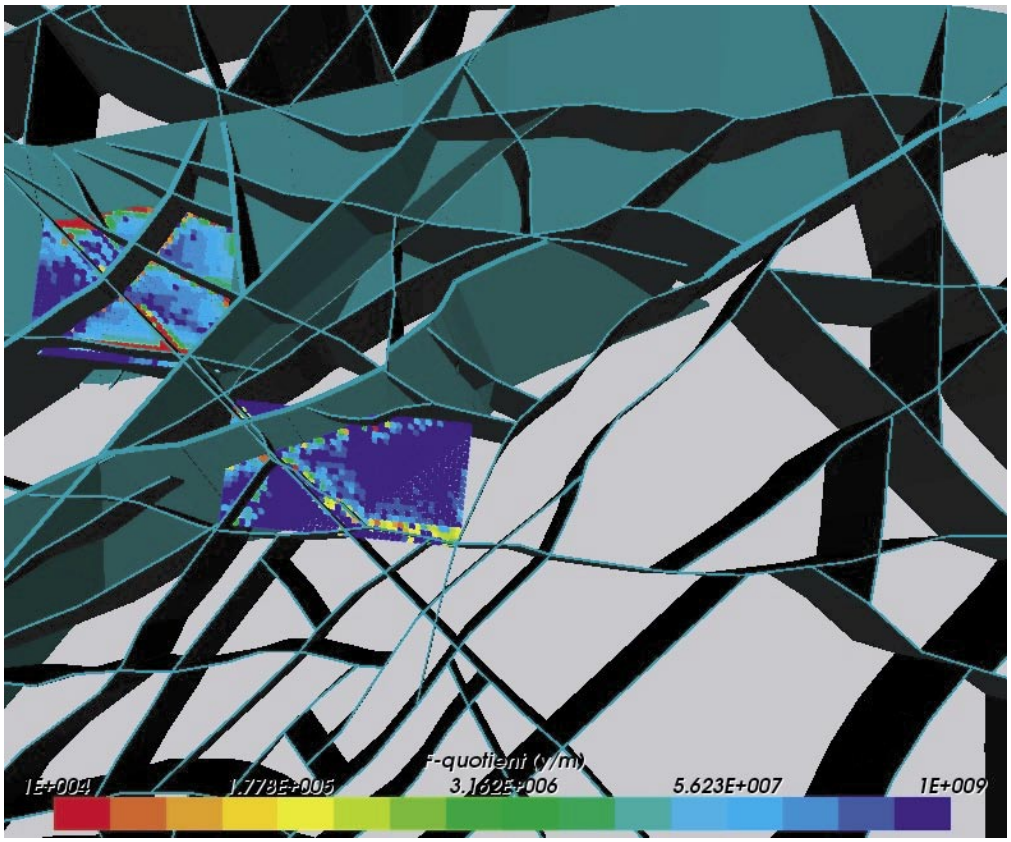

Figure 4-21. *Case 3, low K/φ – start points coloured by total F-quotient (Log-scale 10^4–10^9 years/m) and fracture zones.*

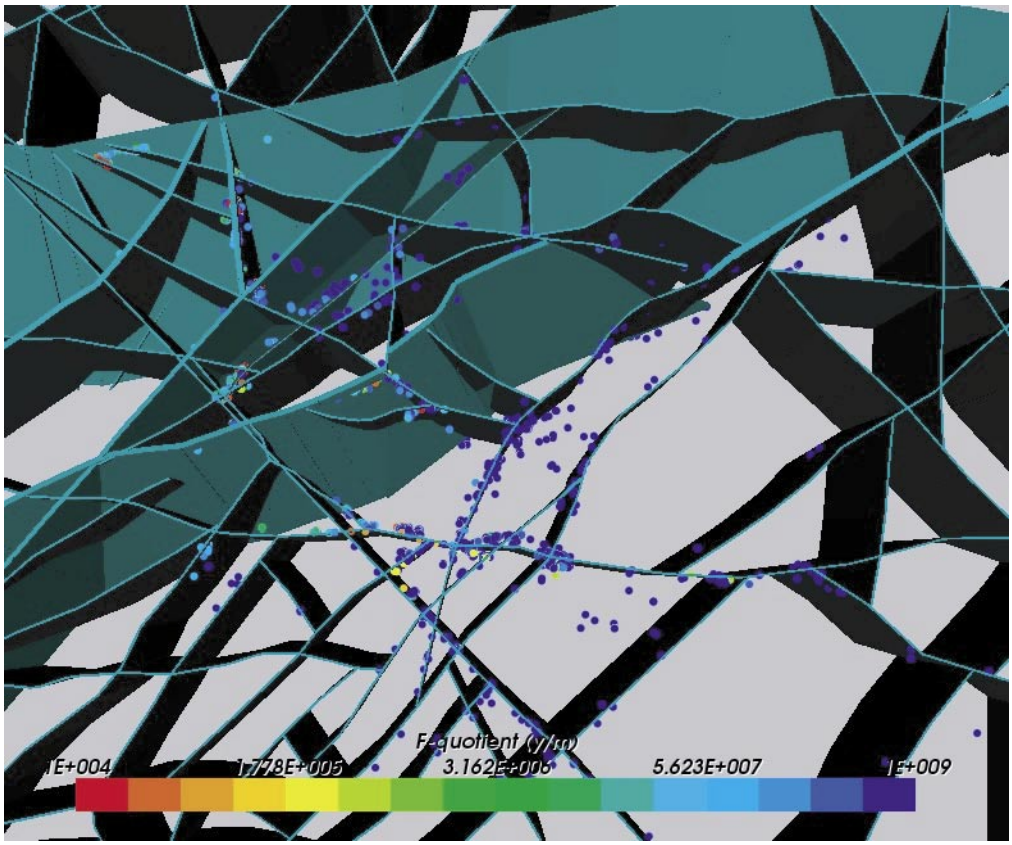

Figure 4-22. *Case 3, low K/φ – start points coloured by total F-quotient (Log-scale 10^4–10^9 years/m) and fracture zones.*

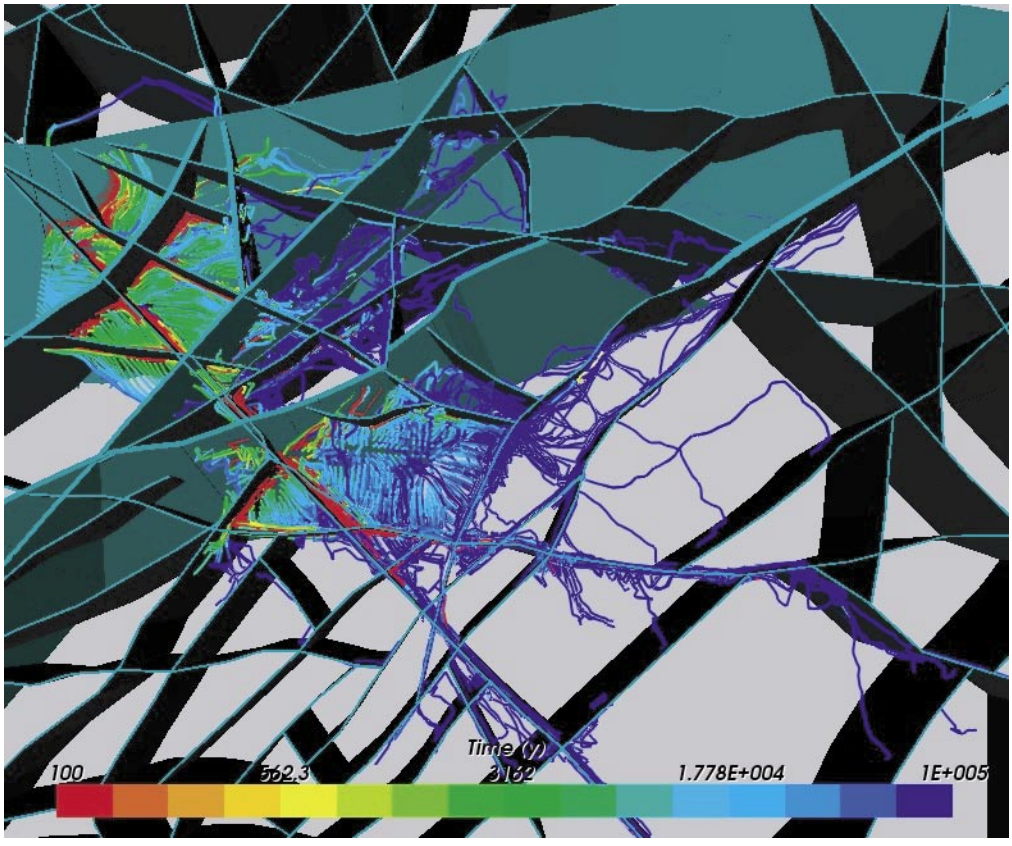

Figure 4-23. *Case 3, low K/φ – particle tracks coloured by travel time (Log-scale 100–10,000 years) along the path and fracture zones.*

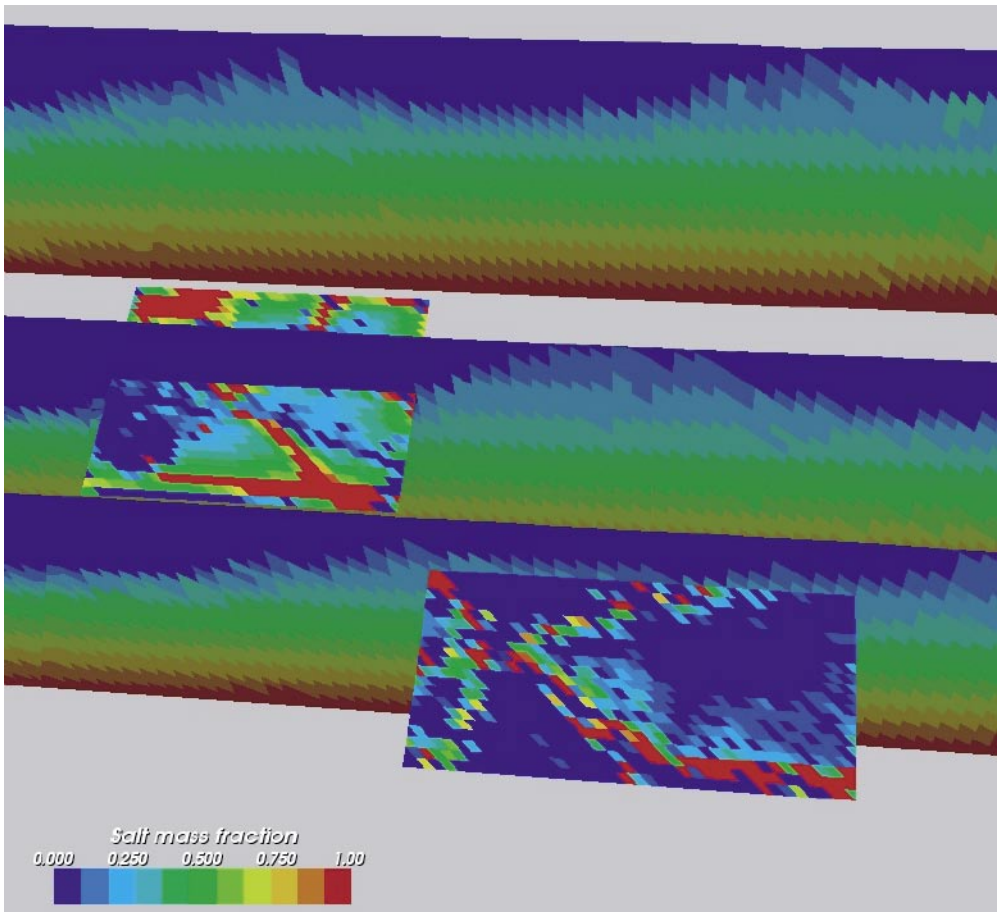

Figure 4-24. *Case3, Salinity distribution on 3 vertical slicesand pathline starting points coloured by travel time (Log-scale 100–10,000 years).*

Performance measure statistics

The transport performance measures are also presented as histograms and cumulative distributions CDF. Figure 4-25 and Figure 4-26 show the travel times (t_w) for both sites combined. This demonstrates a bi-modal behaviour due to some particles starting in or near a fracture zone. The same bi-modal behaviour is shown for Darcy velocity (q_c) and F-quotient.

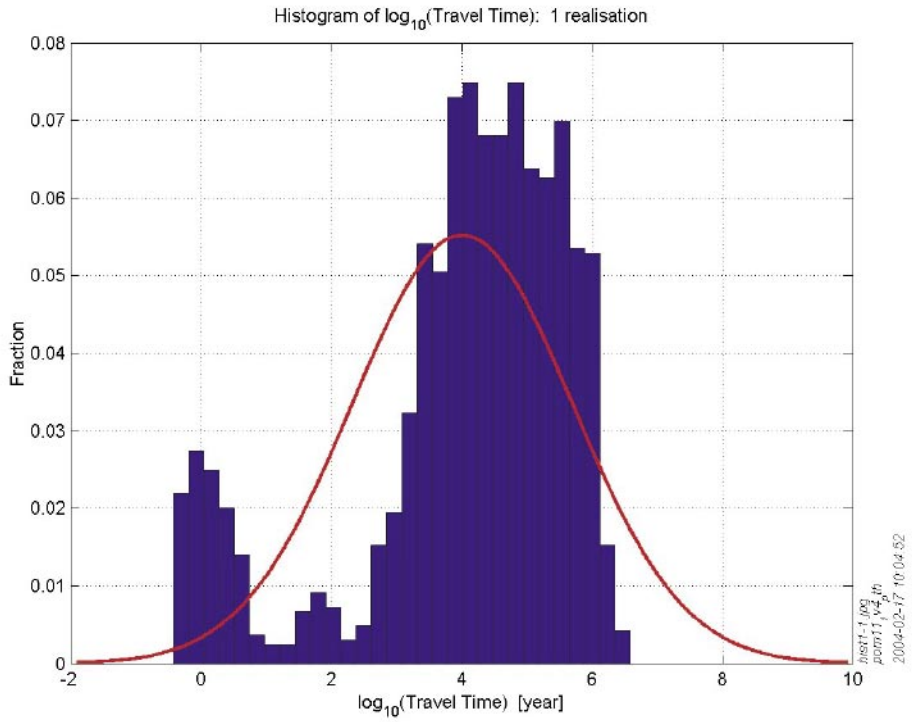

Figure 4-25. *Histogram of t_w using the flow porosity 10^{-5} in the rock mass and $5 \cdot 10^{-5}$ in the fracture zones in Case 3.*

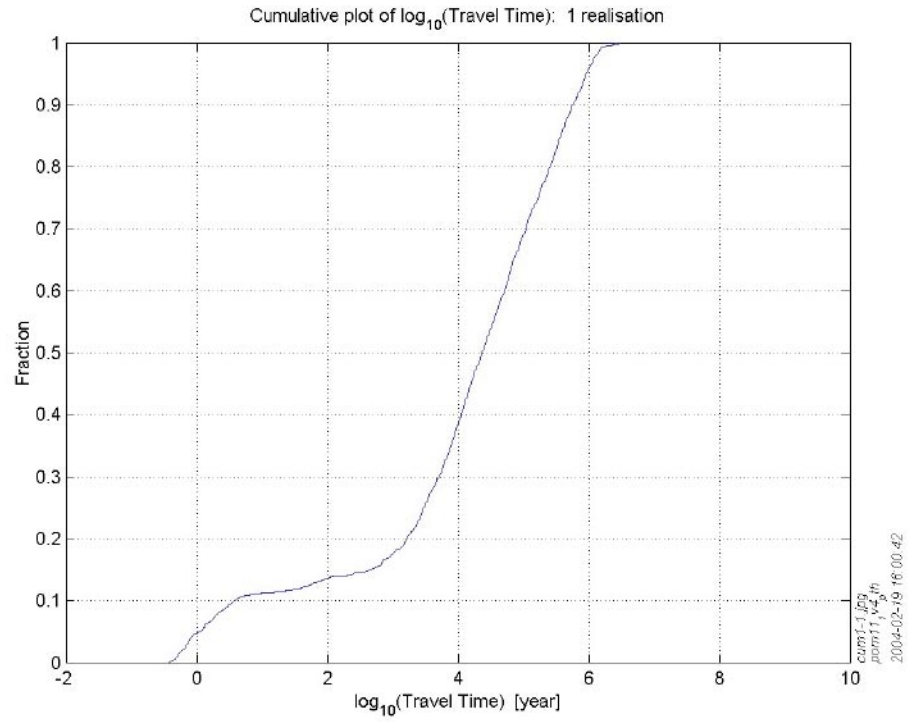

Figure 4-26. *Cumulative distribution t_w using the flow porosity 10^{-5} in the rock mass and $5 \cdot 10^{-5}$ in the fracture zones in Case 3.*

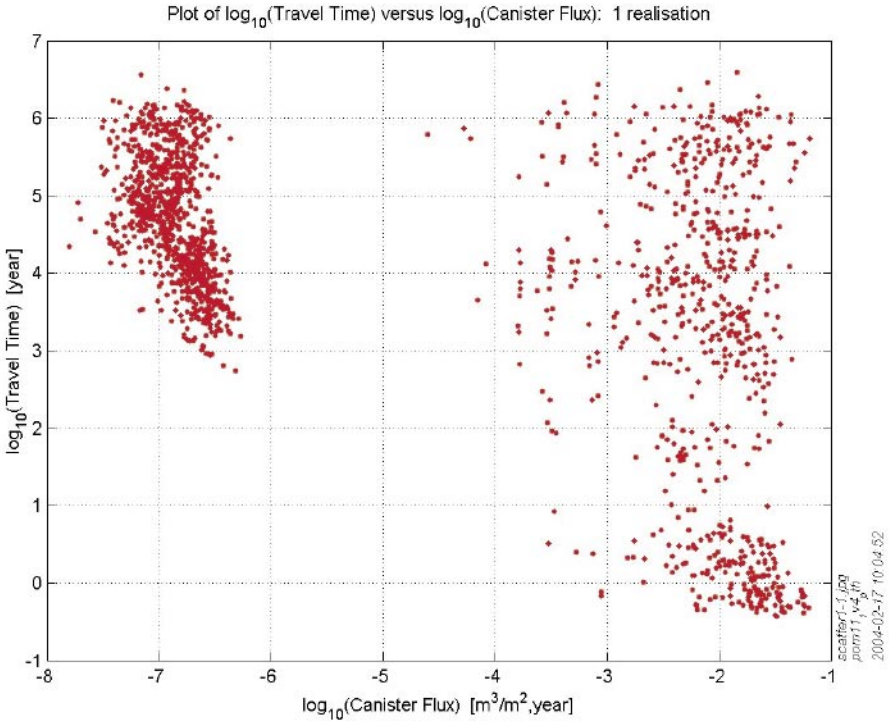

Figure 4-27. *t_w versus q_c, using flow porosity $1 \cdot 10^{-5}$ in the rock mass and $5 \cdot 10^{-5}$ in the fracture zones for Case 3.*

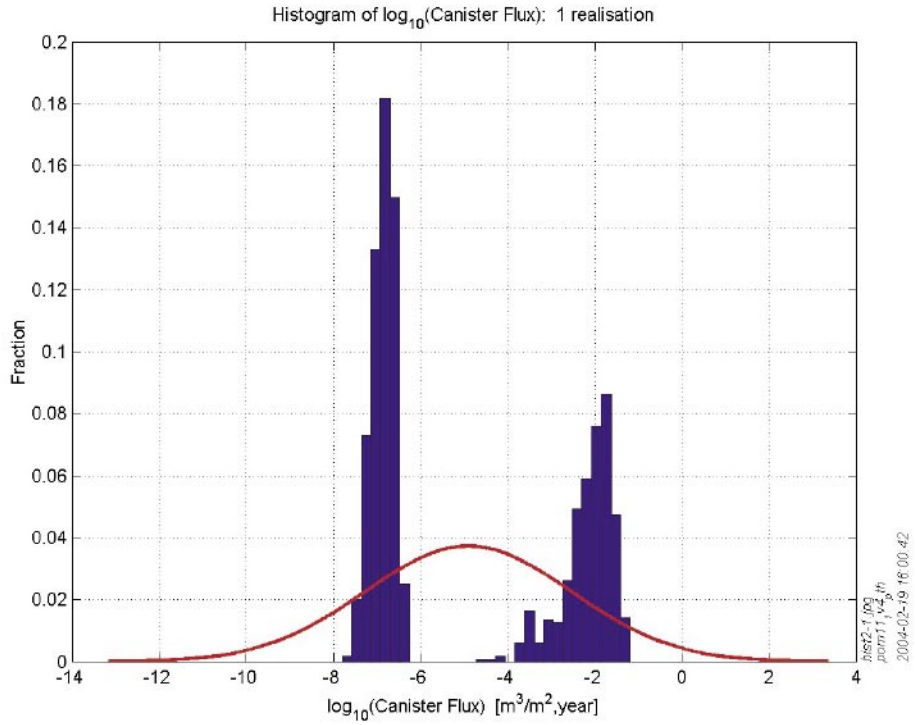

Figure 4-28. *Histogram of canister flux q_c for Case 3.*

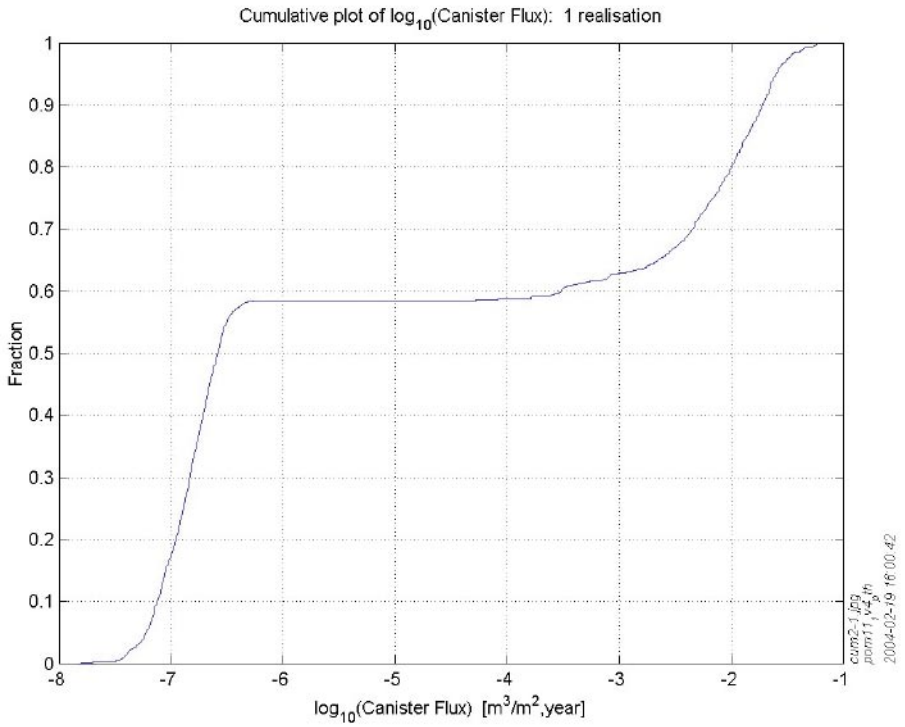

Figure 4-29. *Cumulative distribution of canister flux q_c in Case 3.*

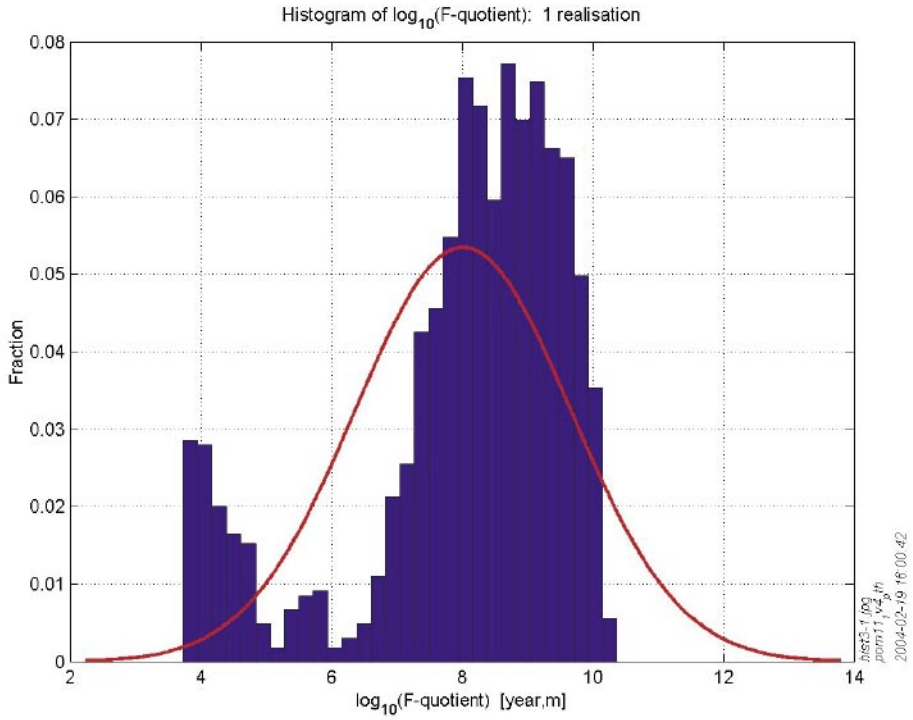

Figure 4-30. *Histogram of F-quotient for Case 3.*

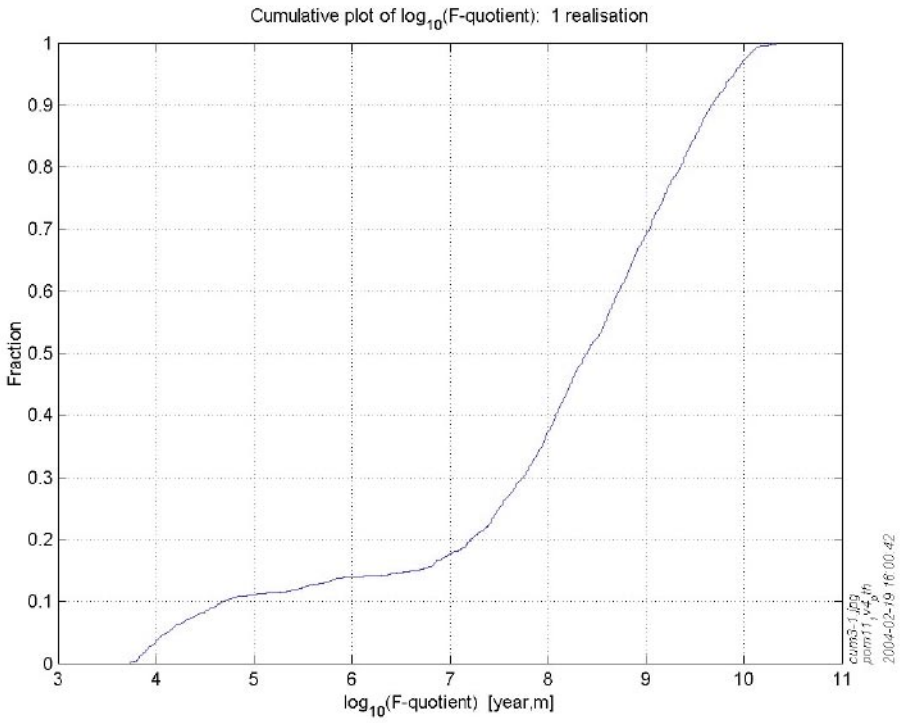

Figure 4-31. *Cumulative distribution of F-quotient in Case 3.*

The statistical summary for the ensemble of Case 3 is shown in Table 4-4, where the statistics are calculated for numbers in $\log_{10}$ space. The keyword Top denotes that statistics are calculated for pathlines reaching the top surface of the model, the keyword Total indicates that it is the whole ensemble, and the keyword Fraction denotes the fraction of starting positions for which that statistics are calculated for.

Table 4-4. Statistical summary for the whole ensemble of Case 3, one realisation and 1 752 starting positions.

Statistical	$\log_{10}(t_w)$	$\log_{10}(q_c)$	$\log_{10}(F)$	$\log_{10}(L)$
Entity	Top	Total	Top	Top
Mean	4.012	–4.912	8.014	3.377
Median	4.368	–6.586	8.396	3.287
5th percentile	0.066	–7.221	4.123	2.882
25th percentile	3.475	–6.896	7.496	3.050
75th percentile	5.227	–2.168	9.176	3.694
95th percentile	5.965	–1.598	9.896	4.064
St deviation	1.690	2.361	1.651	0.380
Variance	2.856	5.573	2.726	0.144
Min value	–0.422	–7.800	3.734	2.756
Max value	6.590	–1.189	10.369	4.308
Fraction	0.939	1.000	0.939	0.939

4.9.2 Laxemar vs Simpevarp

To quantify the differences between Laxemar and Simpevarp statistics were also calculated for the two sites separately. Table 4-5 and Table 4-6 give the performance measure statistics for the two sites individually. Figure 4-32 and Figure 4-33 show the histograms for t_w and F at Laxemar, respectively. Figure 4-34 and Figure 4-35 show the histograms for t_w and F at Simpevarp, respectively. The medians of both t_w and F are about one order of magnitude less for Laxemar than for Simpevarp. Both t_w and F show a bi-modal behaviour which is associated with some particles starting a fracture zone and the rest in the background rock. The effect is more pronounced at Laxemar due to the larger number of fracture zones crossing the local-scale area.

Table 4-5. Statistical summary for the Laxemar area of Case 3, one realisation and 891 starting positions.

Statistical	$Log_{10}(t_w)$	$Log_{10}(q_c)$	$Log_{10}(F)$	$Log_{10}(L)$
Entity	Top	Total	Top	Top
Mean	3.366	–4.584	7.402	3.223
Median	3.832	–6.448	7.859	3.137
5th percentile	–0.170	–7.015	3.921	2.867
25th percentile	3.038	–6.696	7.033	2.977
75th percentile	4.400	–1.980	8.431	3.338
95th percentile	5.815	–1.556	9.771	4.001
St deviation	1.765	2.331	1.731	0.333
Variance	3.117	5.435	2.996	0.111
Min value	–0.422	–7.800	3.734	2.756
Max value	6.590	–1.199	10.369	4.239
Fraction	0.951	1.000	0.951	0.951

Table 4-6. Statistical summary for the Simpevarp area of Case 3, one realisation and 861 starting positions.

Statistical	$Log_{10}(t_w)$	$Log_{10}(q_c)$	$Log_{10}(F)$	$Log_{10}(L)$
Entity	Top	Total	Top	Top
Mean	4.697	–5.252	8.662	3.541
Median	5.037	–6.820	9.003	3.587
5th percentile	1.626	–7.325	5.480	2.964
25th percentile	4.382	–7.068	8.403	3.240
75th percentile	5.530	–2.322	9.448	3.810
95th percentile	6.028	–1.694	9.960	4.091
St deviation	1.292	2.344	1.275	0.358
Variance	1.670	5.495	1.624	0.128
Min value	0.071	–7.723	4.028	2.763
Max value	6.553	–1.189	10.322	4.308
Fraction	0.927	1.000	0.927	0.927

Laxemar

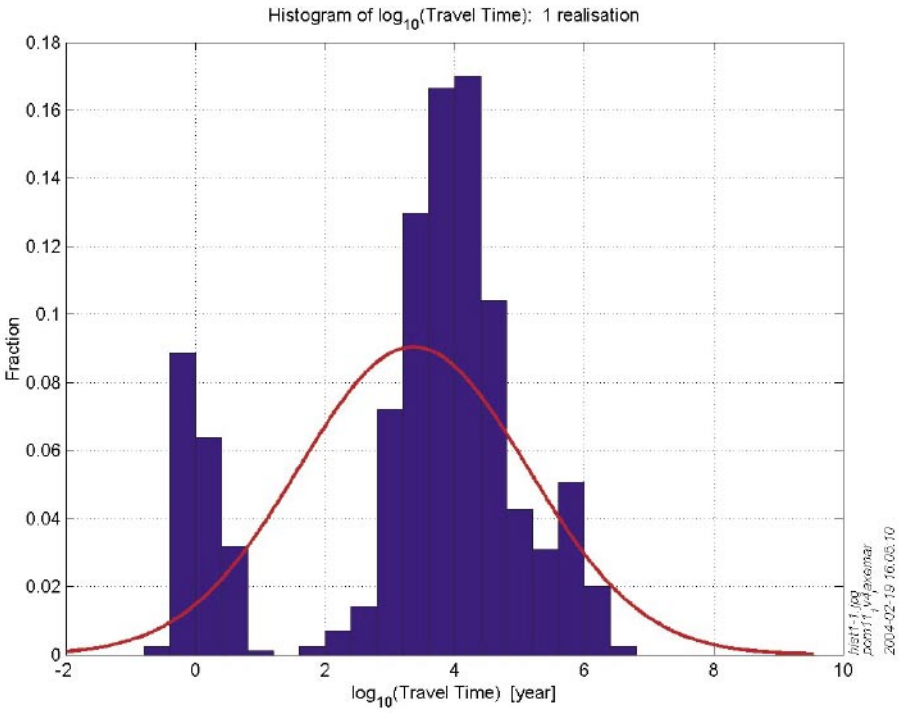

Figure 4-32. *Histogram of tw using the flow porosity 10^{-5} in the rock mass and $5 \cdot 10^{-5}$ in the fracture zones in Case 3. Path lines starts in Laxemar.*

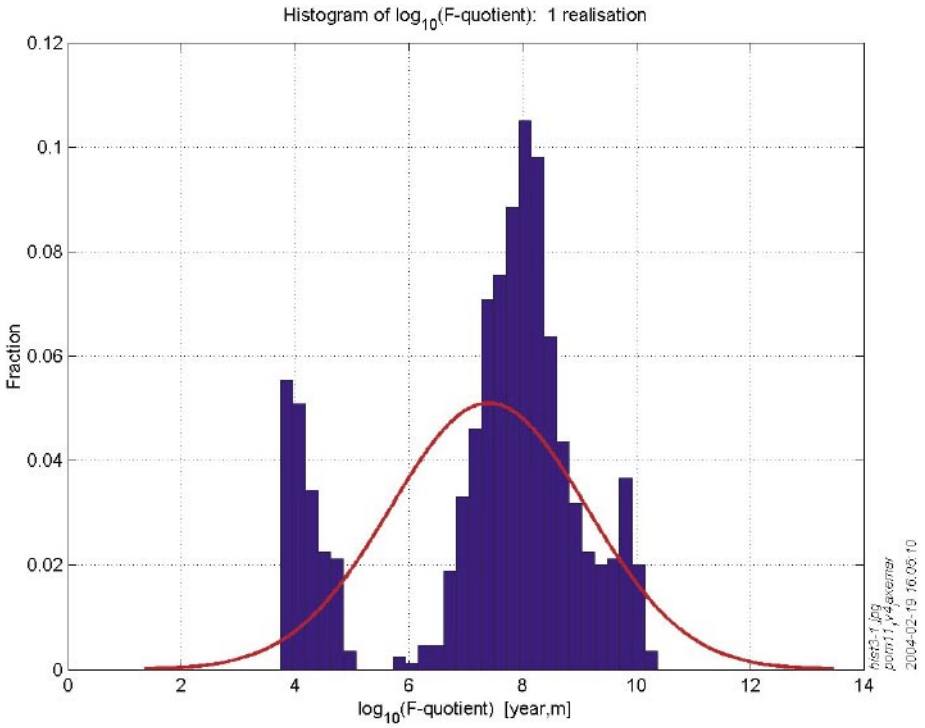

Figure 4-33. *Histogram of F-quotient for Laxemar in Case 3.*

Simpevarp

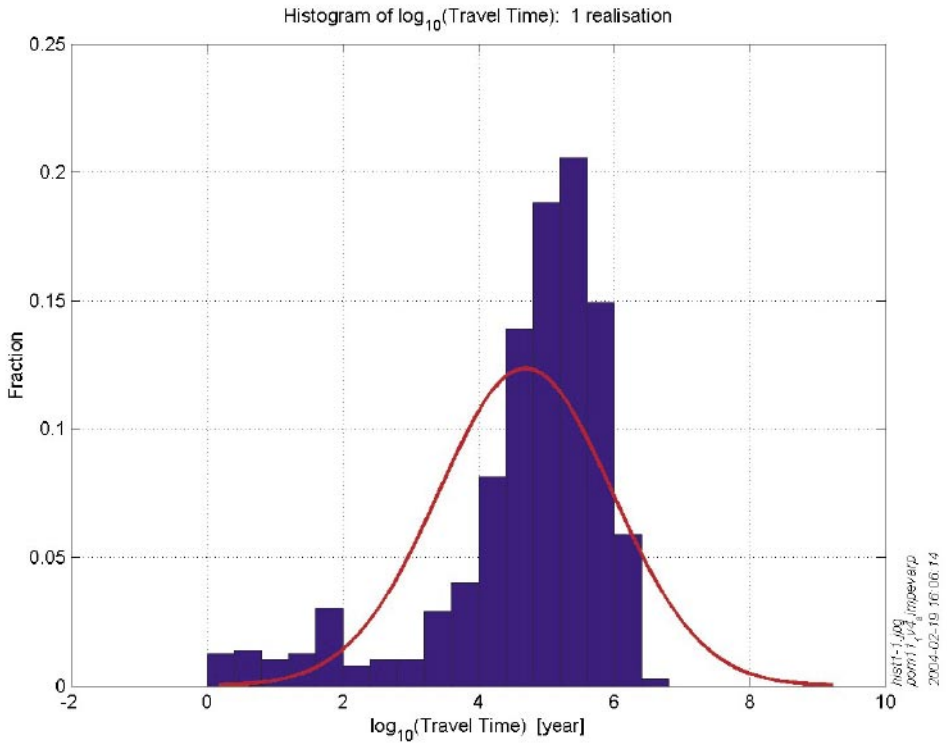

Figure 4-34. *Histogram of t_w using the flow porosity 10^{-5} in the rock mass and $5{\cdot}10^{-5}$ in the fracture zones in Case 3. Pathlines start in Simpevarp.*

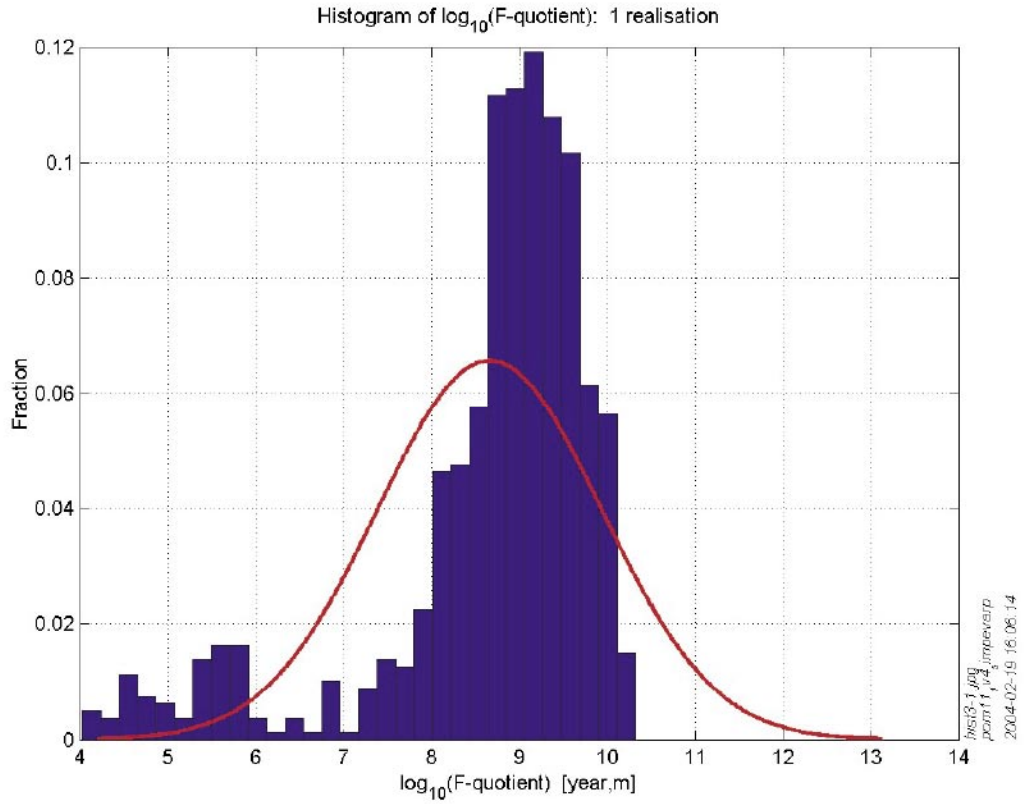

Figure 4-35. *Histogram of F-quotient for Simpevarp in Case 3.*

A quantitative comparison of each performance measure between particles starting in the Laxemar and Simpevarp areas is given in Table 4-7, Table 4-8 and Table 4-9.

Table 4-7. Comparison of $log_{10}(t_w)$ between Laxemar, Simpevarp and the whole ensemble.

Statistical	Laxemar	Simpevarp	Ensemble
Entity	Top	Top	Top
Mean	3.366	4.697	4.012
Median	3.832	5.037	4.368
5th percentile	–0.170	1.626	0.066
25th percentile	3.038	4.382	3.475
75th percentile	4.400	5.530	5.227
95th percentile	5.815	6.028	5.965
St deviation	1.765	1.292	1.690
Variance	3.117	1.670	2.856
Min value	–0.422	0.071	–0.422
Max value	6.590	6.553	6.590
Fraction	0.951	0.927	0.939
Number starting	891	861	1752

Table 4-8. Comparison of $log_{10}(q_c)$ between Laxemar, Simpevarp and the whole ensemble.

Statistical	Laxemar	Simpevarp	Ensemble
Entity	Total	Total	Total
Mean	–4.584	–5.252	–4.912
Median	–6.448	–6.820	–6.586
5th percentile	–7.015	–7.325	–7.221
25th percentile	–6.696	–7.068	–6.896
75th percentile	–1.980	–2.322	–2.168
95th percentile	–1.556	–1.694	–1.598
St deviation	2.331	2.344	2.361
Variance	5.435	5.495	5.573
Min value	–7.800	–7.723	–7.800
Max value	–1.199	–1.189	–1.189
Fraction	1.000	1.000	1.000
Number starting	891	861	1752

Table 4-9. Comparison of log_{10}(F) between Laxemar, Simpevarp and the whole ensemble.

Statistical	Laxemar	Simpevarp	Ensemble
Entity	Top	Top	Top
Mean	7.402	8.662	8.014
Median	7.859	9.003	8.396
5th percentile	3.921	5.480	4.123
25th percentile	7.033	8.403	7.496
75th percentile	8.431	9.448	9.176
95th percentile	9.771	9.960	9.896
St deviation	1.731	1.275	1.651
Variance	2.996	1.624	2.726
Min value	3.734	4.028	3.734
Max value	10.369	10.322	10.369
Fraction	0.951	0.927	0.939
Number starting	891	861	1752

4.9.3 Case 4

This case is included as a possible interpretation of the fracture data that results in a higher permeability for the rock mass due to an underlying fracture-intensity 5 times higher. The pathlines are shown in Figure 4-36. In this case, the travel times are higher but pathlines are less concentrated toward the fracture zones as there is less of a contrast between the rock mass and fracture zones.

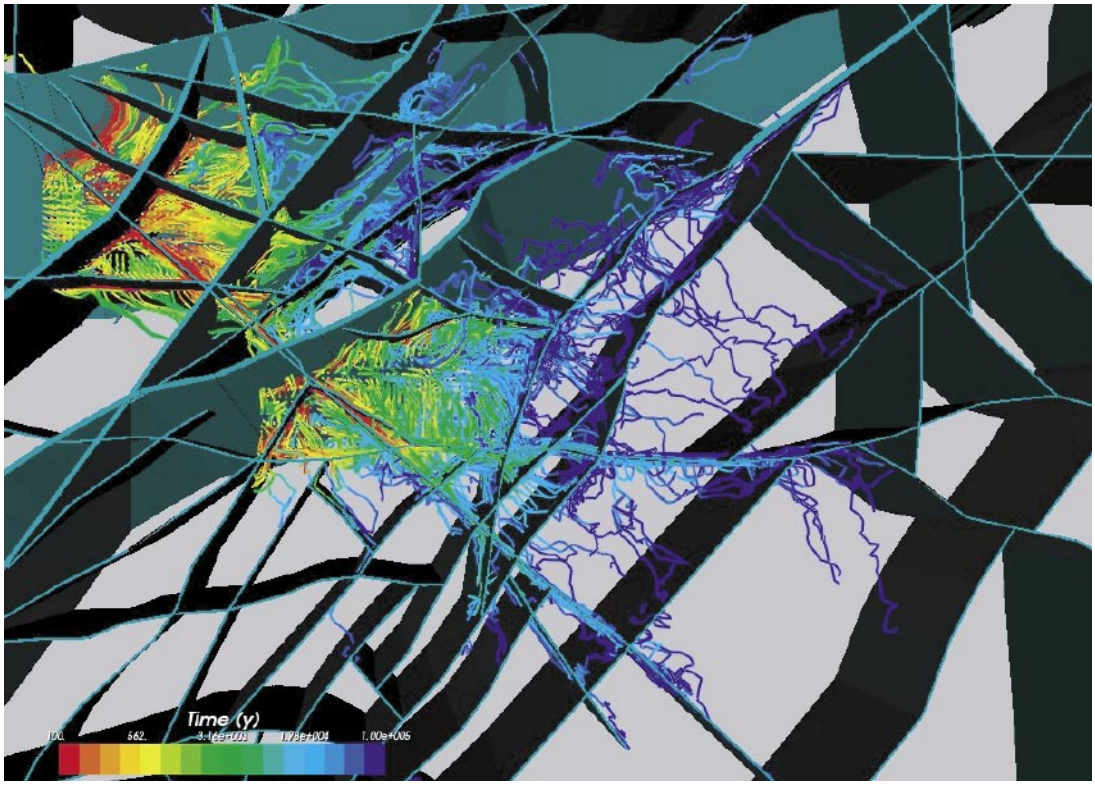

Figure 4-36. *Case 4, high K/φ – pathlines coloured by travel time along path fracture zones.*

Performance measure statistics

Figure 4-37 to Figure 4-39 show the histograms for t_w, q_c and F-quotient for Case 4, respectively. Travel times and F-quotient are reduced by about an order of magnitude, and the bi-modal distribution is still evident.

The statistical summary for the ensemble of Case 4 is shown in Table 4-10, where the statistics are calculated for numbers in $\log_{10}$ space. The keyword Top denotes that statistics are calculated for pathlines reaching the top surface of the model, the keyword Total indicates that it is the whole ensemble, and the keyword Fraction denotes the fraction of starting positions for which that statistics are calculated for.

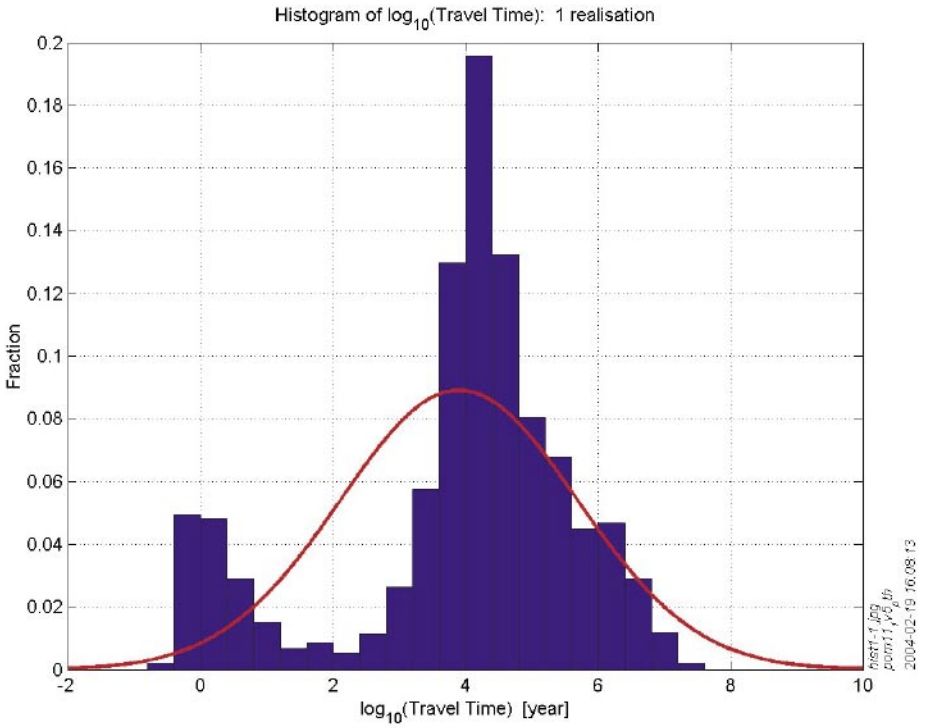

Figure 4-37. *Histogram of t_w using the flow porosity $1e10^{-5}$ in the rock mass and $5 \cdot 10^{-5}$ in the fracture zones in Case 4.*

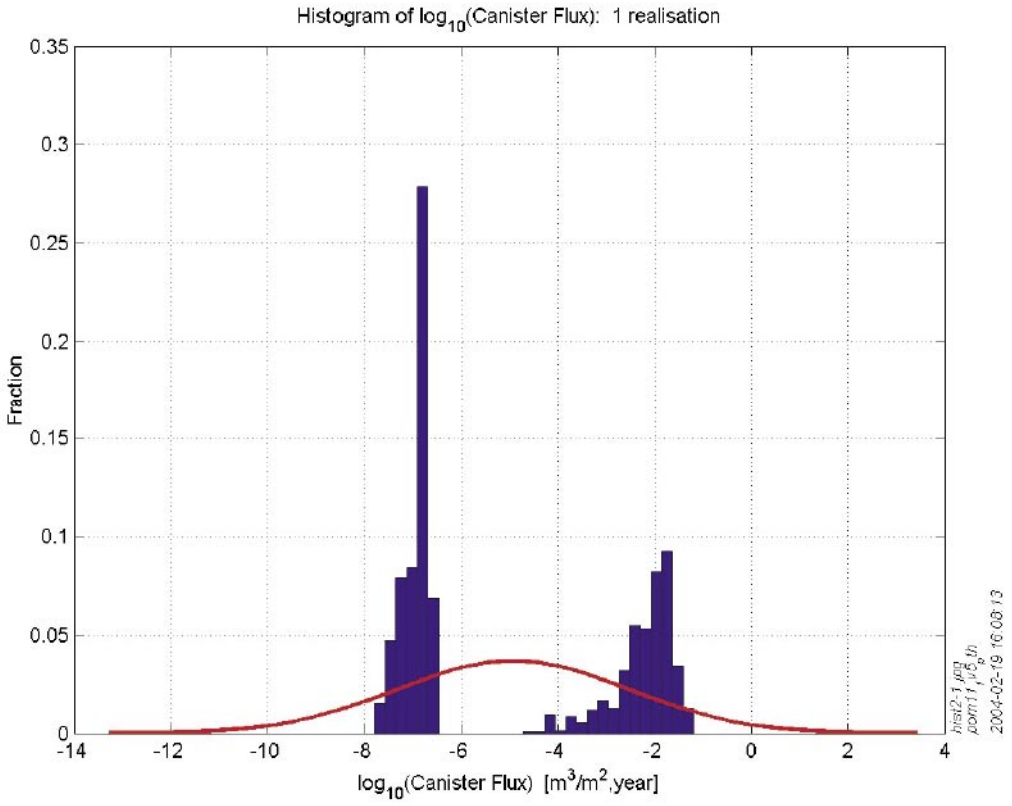

Figure 4-38. *Histogram of qc for Case 4.*

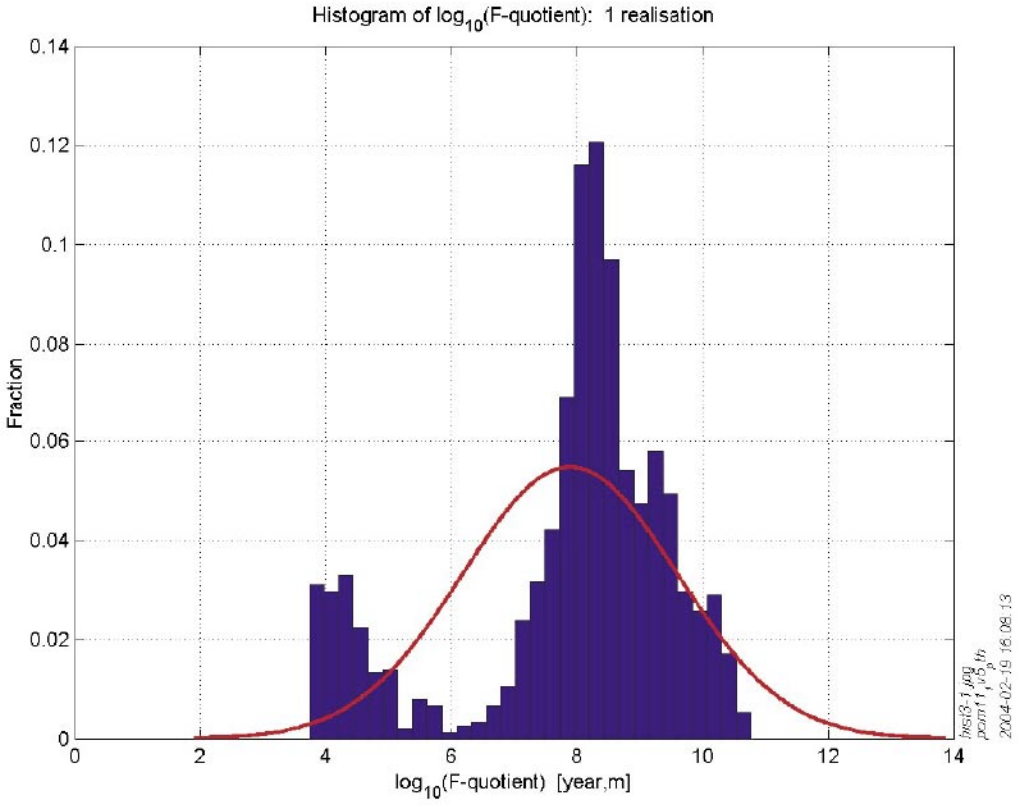

Figure 4-39. *Histogram of F-quotient for Case 4.*

Table 4-10. Statistical summary for the whole ensemble of Case 4, one realisation and 1752 starting positions.

Statistical	$Log_{10}(t_w)$	$Log_{10}(q_c)$	$Log_{10}(F)$	$Log_{10}(L)$
Entity	Top	Total	Top	Top
Mean	3.904	–5.003	7.889	3.242
Median	4.239	–6.723	8.265	3.145
5th percentile	–0.003	–7.452	4.101	2.835
25th percentile	3.556	–6.923	7.580	2.985
75th percentile	4.960	–2.245	8.966	3.410
95th percentile	6.332	–1.656	10.076	4.064
St deviation	1.792	2.388	1.710	0.357
Variance	3.211	5.701	2.924	0.128
Min value	–0.427	–7.788	3.735	2.703
Max value	7.307	–1.195	10.775	4.297
Fraction	0.866	1.000	0.866	0.866

5 Summary and conclusions

The general methodology for modelling transient salt transport and groundwater flow using CONNECTFLOW that was developed for Forsmark has been applied successfully also for Simpevarp. Because of time constraints only a key set of variants were performed that focussed on the influences of DFN model parameters, the kinematic porosity, and the initial condition. Salinity data in deep boreholes available at the time of the project was too limited to allow a good calibration exercise. However, the model predictions are compared with the available data from KLX01 and KLX02 below. Once more salinity data is available it may be possible to draw more definite conclusions based on the differences between variants. At the moment though the differences should just be used understand the sensitivity of the models to various input parameters.

5.1 Comparison of cases

Here we summarise the cases performed in terms of the prediction of salinity at various times in the past and a comparison between the present day profiles with the observed salinity.

5.1.1 KLX01

Figure 5-1 shows the salinity profiles for the 6 main cases at 5000 BC together with the two initial conditions. For all cases the salinity is higher than the initial condition resulting from the infiltration of saline Litorina water that covered the area at this time. The highest profiles are for the cases with high K/φ suggesting a greater saline flux for these cases.

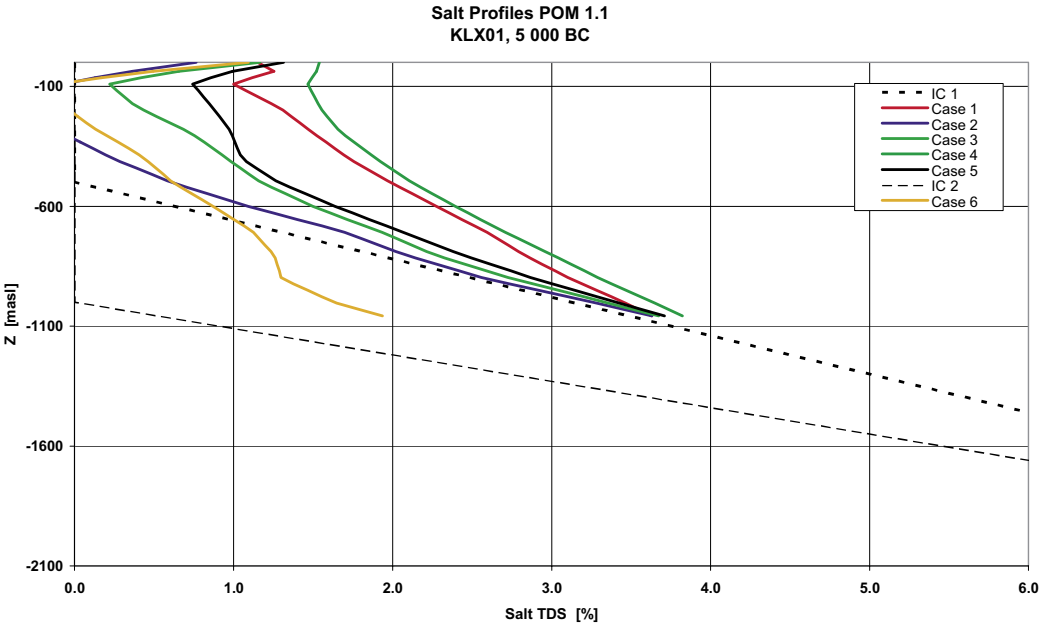

Figure 5-1. *Salinity profiles at 5000 BC for different cases for the borehole KLX01.*

Figure 5-2 and Figure 5-3 show the salinity profiles for 0 BC and 2000 AD respectively. The results are relatively insensitive and are clustered around Initial condition 1. The observed data for KLX01 is very limited, only 3 points. As far as it goes, the data is in line with the predictions.

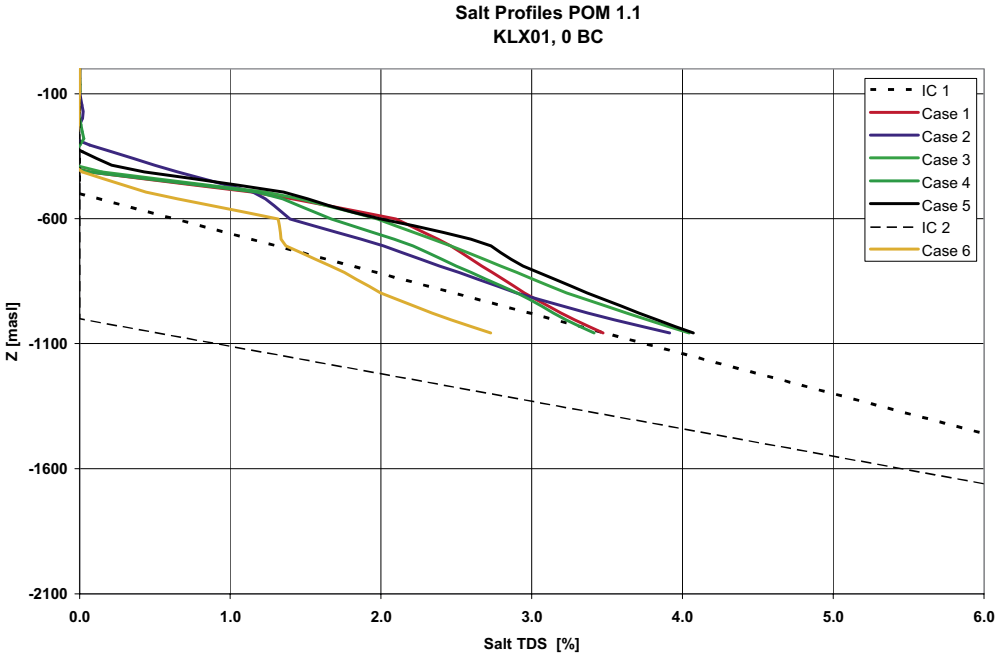

Figure 5-2. *Salinity profiles at 0 BC for different cases for the borehole KLX01.*

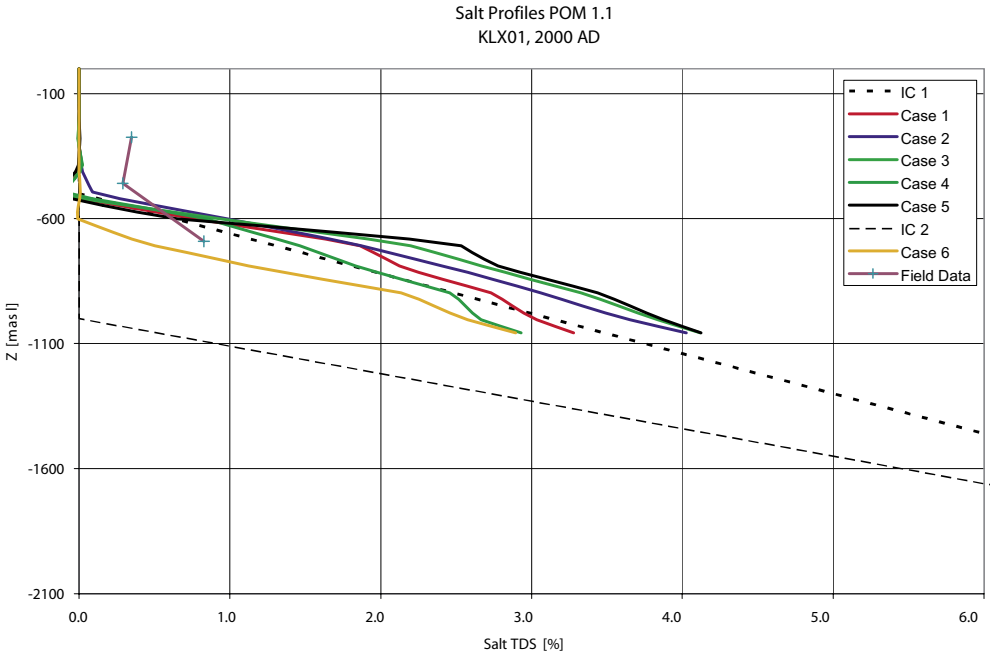

Figure 5-3. *Salinity profiles at 2000 AD for different cases for the borehole KLX01. Field data and both initial conditions are included.*

5.1.2 KLX02

KLX02 is much more interesting as it goes much deeper and there observed data is of a better quality. At 5000 BC, Figure 5-4, again all profiles are above the initial condition although for there is a steeper slope for the variants with high K/φ (Need to replace 1v5 with time converged solutions). By 0 BC, Figure 5-5, 1v7 with the lower initial condition (IC2) has moved up much more in line with the other cases that use IC1.

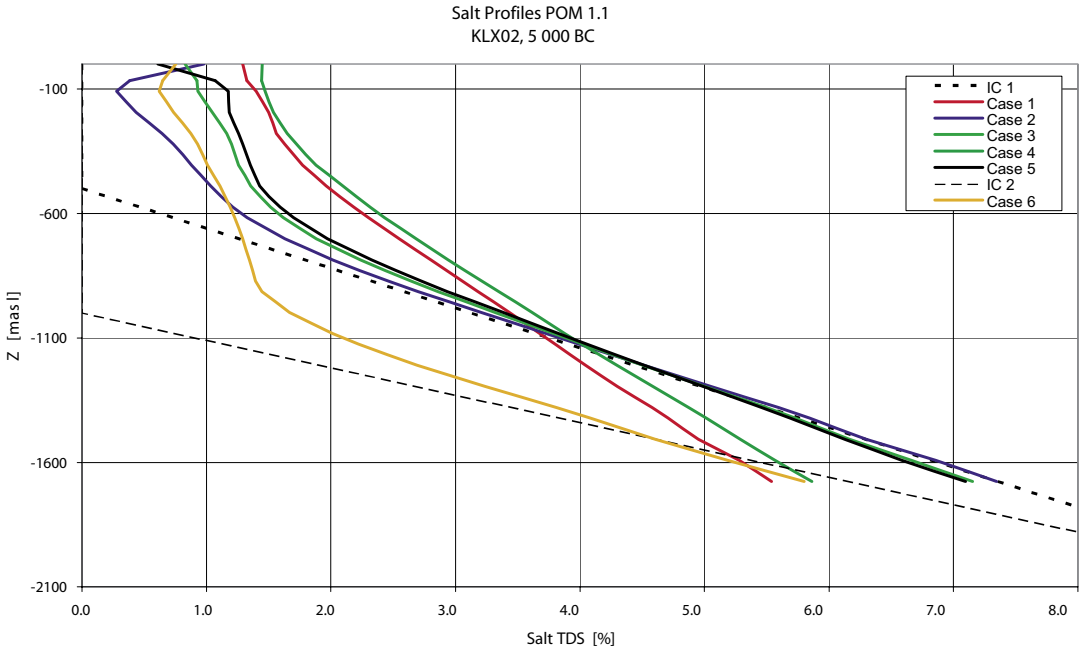

Figure 5-4. *Salinity profiles at 5000 BC for different cases for the borehole KLX02.*

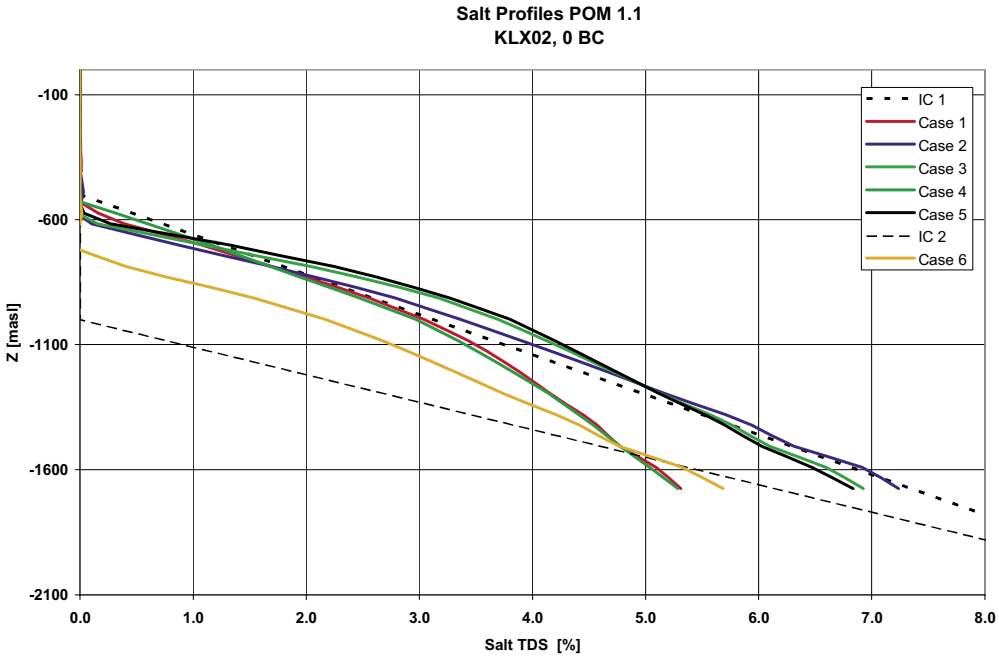

Figure 5-5. *Salinity profiles at 0 BC for different cases for the borehole KLX02.*

Figure 5-6 shows the profiles in KLX02 for the present day compared with the observed data. The field data has a relatively shallow slope and mostly lower than IC1. Several alternative changes could be made to better fit the data. That is, there is probably not a unique approach or set of parameters. High values of K/φ might make it hard to get a match to such a shallow salinity gradient. Otherwise a higher salinity at depth or higher salinity for the Litorina Sea would probably give a better match. The two short steps in the observed data are interesting and if seen in other future deep boreholes may help to calibrate features of the structural model as they may suggest compartmentalisation, for example due to sealing fracture zones.

It can be concluded that really only two distinct sets of results have been obtained for the cases considered in Cases 1 to 5, and that it is the ratio K/φ that is key. For values of $K/\varphi < 5 \cdot 10^{-6}$ m/s, KLX02 is close to the initial guess. For values of $K/\varphi > 10^{-5}$ m/s, salinity gradients are steeper suggesting greater flushing of saline waters at depth.

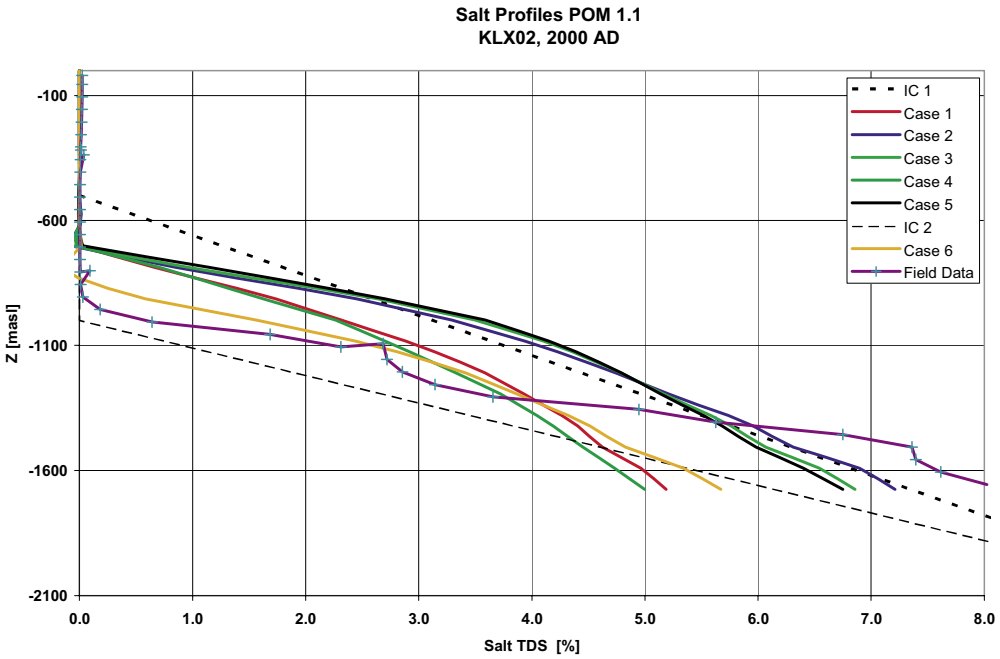

Figure 5-6. *Salinity profiles at 2000 AD for different cases for the borehole KLX02. Field data and both initial conditions are included.*

5.2 Transport calculations

Figure 5-7 and Figure 5-8 summarise the transport performance measure statistics. Figure 5-7 shows the travel-time is bi-modal. This is due to a few particles starting in the fractures zones and the rest starting in the background rock. The travel times are much shorter in the fracture zones due to their very high relative permeability. In the future, calculations need to be performed with more refinement in the local-scale area or the use of nested models to better resolve the variations in flow within the repository area. The current results probably give an indication of the relative performance measures between sites, but details such as respect distances between start locations and fracture zones will have a large effect on the distribution of performance measures, and generally reducing the occurrence of high flow rates. The pessimistic results of Case 4 based on a high fracture-intensity need some consideration as to whether they are possible. The best way to do this would be to use a DFN model to predict equivalent permeabilities on a range of interval lengths that can be compared with packer-interval test data to establish if such a high conductive fracture-intensity can be realised. A quantitative comparison of the performance measures between Cases 3 and 4 is made in Table 5-2 and Table 5-3.

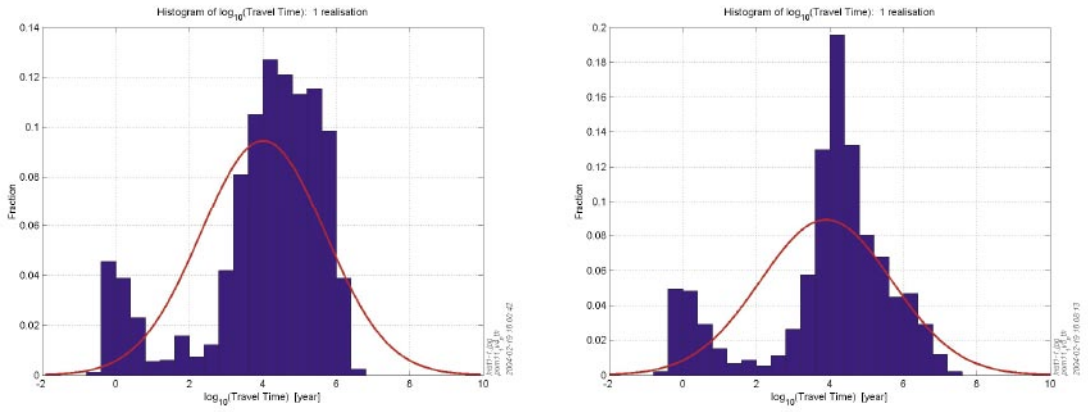

Figure 5-7. *Comparison of t_w distribution for Case 3 (left) and Case 4 (right).*

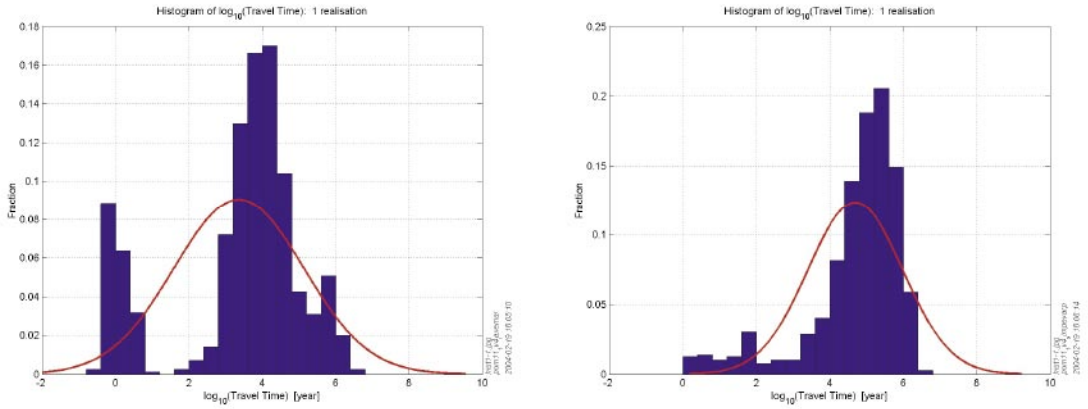

Figure 5-8. *Comparison of t_w Laxemar (left) and Simpevarp (right) for Case 3.*

Table 5-1. Comparison of $\log_{10}(t_w)$ between Case 3 and Case 4.

Statistical	Case 3	Case 4
Entity	Top	Top
Mean	4.012	3.904
Median	4.368	4.239
5th percentile	0.066	–0.003
25th percentile	3.475	3.556
75th percentile	5.227	4.960
95th percentile	5.965	6.332
St deviation	1.690	1.792
Variance	2.856	3.211
Min value	–0.422	–0.427
Max value	6.590	7.307
Fraction	0.939	0.866

Table 5-2. Comparison of $\log_{10}(q_c)$ between Laxemar, Simpevarp and the whole ensemble.

Statistical	Case 3	Case 4
Entity	Total	Total
Mean	–4.912	–5.003
Median	–6.586	–6.723
5th percentile	–7.221	–7.452
25th percentile	–6.896	–6.923
75th percentile	–2.168	–2.245
95th percentile	–1.598	–1.656
St deviation	2.361	2.388
Variance	5.573	5.701
Min value	–7.800	–7.788
Max value	–1.189	–1.195
Fraction	1.000	1.000

Table 5-3. Comparison of $\log_{10}(F)$ between Laxemar, Simpevarp and the whole ensemble.

Statistical	Case 3	Case 4
Entity	Top	Top
Mean	8.014	7.889
Median	8.396	8.265
5th percentile	4.123	4.101
25th percentile	7.496	7.580
75th percentile	9.176	8.966
95th percentile	9.896	10.076
St deviation	1.651	1.710
Variance	2.726	2.924
Min value	3.734	3.735
Max value	10.369	10.775
Fraction	0.939	0.866

The smaller travel times and F-quotients in Laxemar than Simpevarp are a consequence of two reasons: there are more fracture zones crossing the Laxemar area; and also there is less salinity at repository depth for Laxemar. The effect of the extra fracture zones should be verified by use of more detailed local-scale models to check whether it is not just an effect of the coarse discretisation of the fracture zones.

Some additional observations on the transport are:

- There are fast paths to the surface in NW Laxemar and the intersection of two fracture zones just East of Laxemar.
- Discharge in Simpevarp is through a large fracture to the North and the intersection of two fracture zones South and SW.
- High K/φ obviously gives faster paths, but also fewer long paths (again probably due to a deeper saline interface in this case).

6 References

1. **Hartley L J, Holton D, 2003.** CONNECTFLOW (Release 2.0) Technical Summary Document. SERCO/ERRA-C/TSD02V1.
2. **Hartley L J, Hoch A R, Cliffe K A C, Jackson C P, Holton D, 2003.** NAMMU (Release 7.2) Technical Summary Document. SERCO/ERRA-NM/TSD02V1.
3. **Hartley L J, Holton D, Hoch A R, 2003.** NAPSAC (Release 4.4) Technical Summary Document. SERCO/ERRA-N/TSD02V1 (2003).
4. **Hoch A R, Hartley L J, 20003.** NAMMU (Release 7.2) Verification Document. SERCO/ERRA-NM/VD02V2.
5. **Hoch A R, Hartley L J, Holton D, 2002.** NAPSAC (Release 4.3) Verification Document. SERCO/ERRA-NM/VD02V1.
6. **Jackson C P, Hoch A R, Todman S, 2000.** Self-consistency of a heterogeneous continuum porous medium representation of a fractured medium. WATER RESOURCES RESEARCH, VOL. 36, NO. 1, PAGES 189–202.
7. **Marsic N, Hartley L, Jackson P, Poole M, Morvik A, 2001.** Development of hydrogeological modelling tools based on NAMMU, R-01-49.

Appendix

Evolution of the shoreline in history for the study area

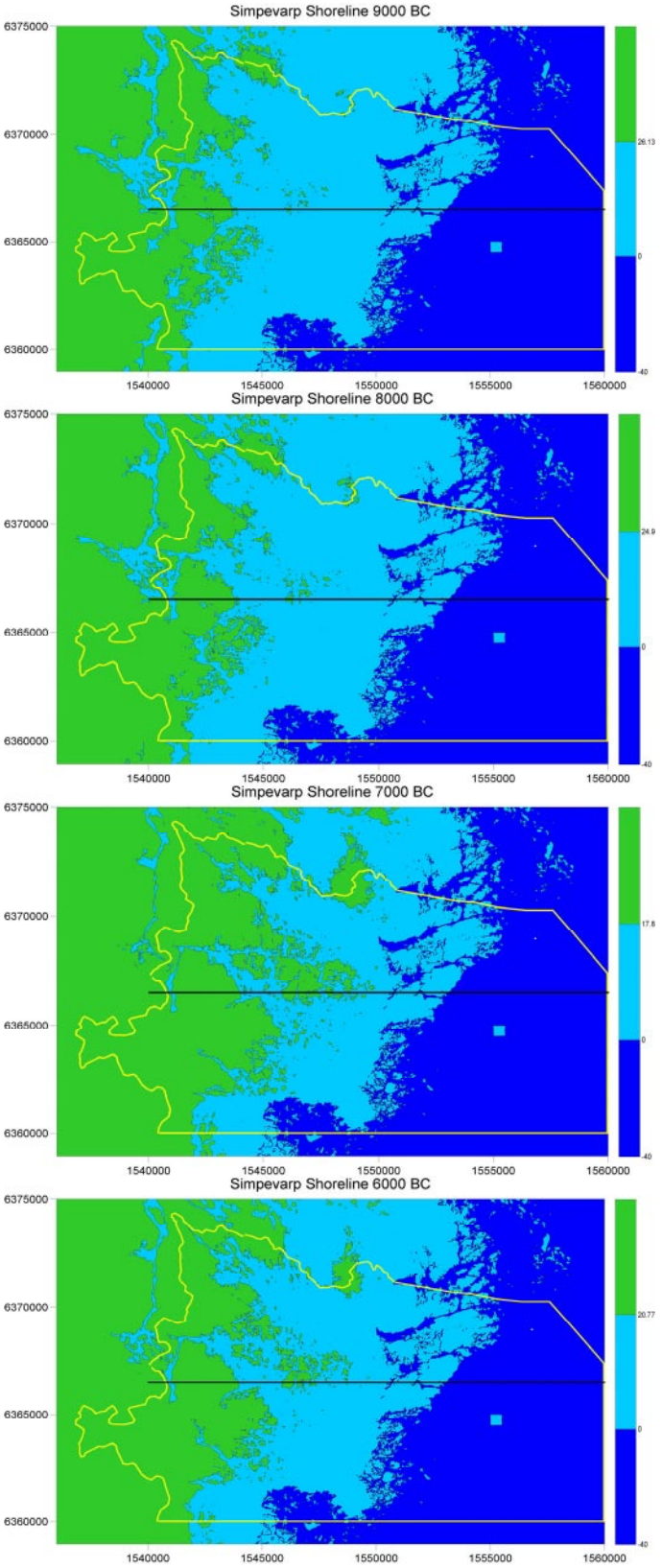

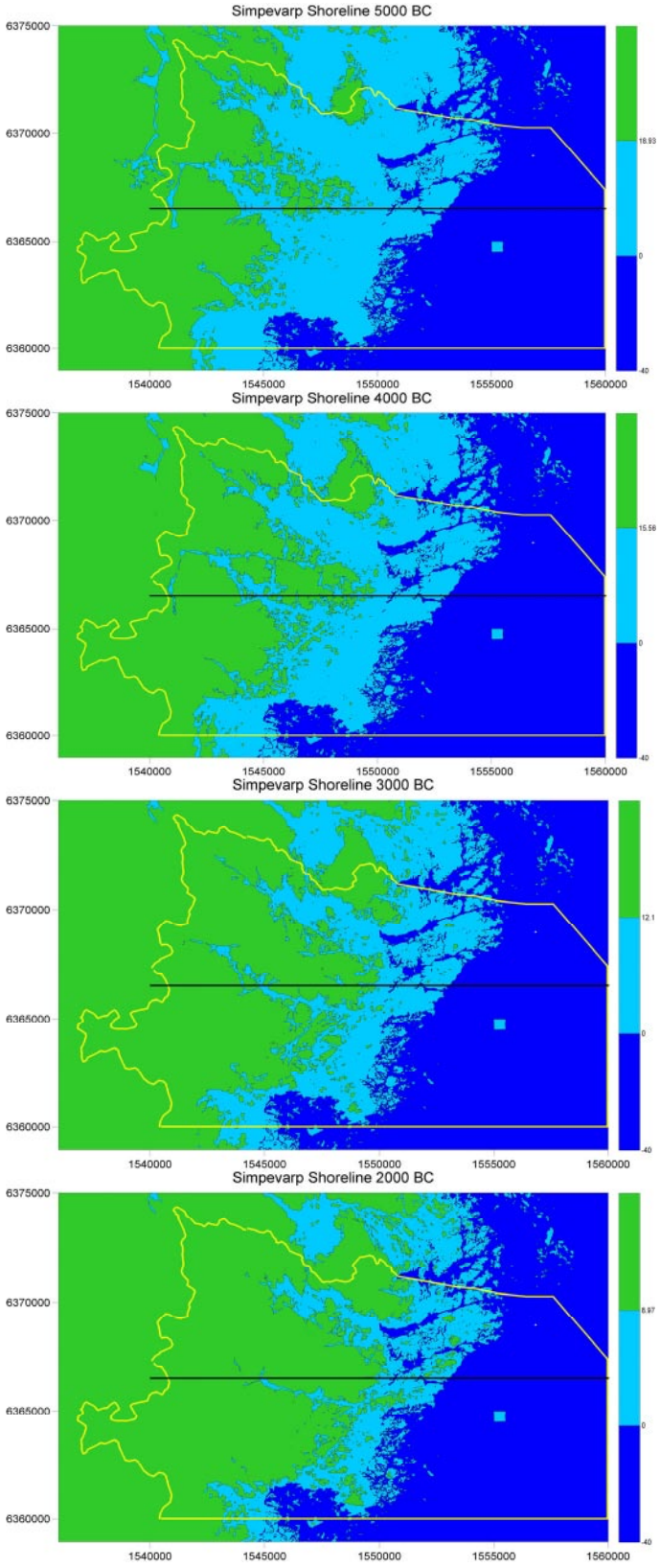
Simpevarp Shoreline 5000 BC
6375000
6370000
6365000
6360000
1540000
1545000
1550000
1555000
1560000
18.93
0
-40
Simpevarp Shoreline 4000 BC
6375000
6370000
6365000
6360000
1540000
1545000
1550000
1555000
1560000
15.58
0
-40
Simpevarp Shoreline 3000 BC
6375000
6370000
6365000
6360000
1540000
1545000
1550000
1555000
1560000
12.1
0
-40
Simpevarp Shoreline 2000 BC
6375000
6370000
6365000
6360000
1540000
1545000
1550000
1555000
1560000
8.97
0
-40

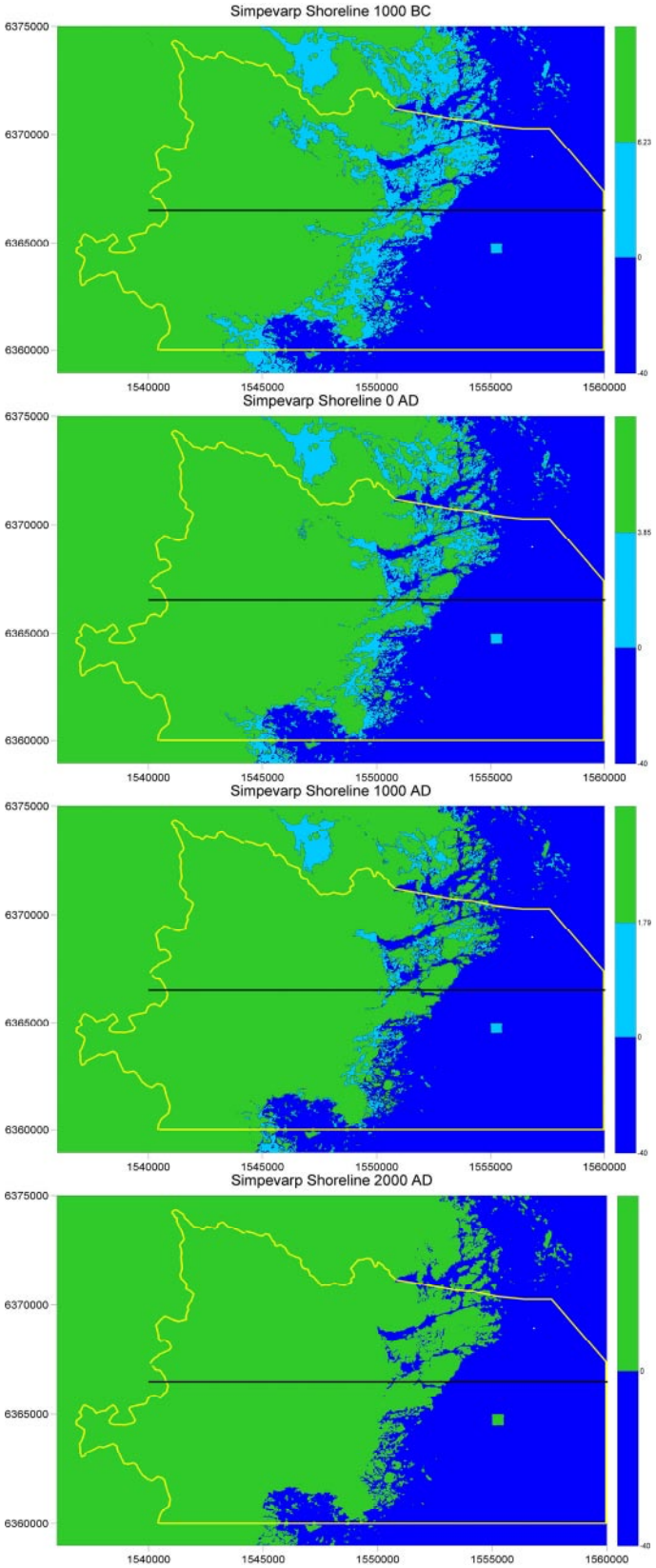
Simpevarp Shoreline 1000 BC
6375000
6370000
6365000
6360000
1540000
1545000
1550000
1555000
1560000
6.23
0
-40
Simpevarp Shoreline 0 AD
6375000
6370000
6365000
6360000
1540000
1545000
1550000
1555000
1560000
3.85
0
-40
Simpevarp Shoreline 1000 AD
6375000
6370000
6365000
6360000
1540000
1545000
1550000
1555000
1560000
1.79
0
-40
Simpevarp Shoreline 2000 AD
6375000
6370000
6365000
6360000
1540000
1545000
1550000
1555000
1560000
0
-40